2019

Investigation of shrinkage-compensating cement concrete from material and structural perspectives

Weizhuo Shi
Iowa State University

Investigation of shrinkage-compensating cement concrete from material and structural perspectives

by

Weizhuo Shi

A dissertation submitted to the graduate faculty

in partial fulfillment of the requirements for the degree of

DOCTOR OF PHILOSOPHY

Major: Civil Engineering (Structural Engineering)

Program of Study Committee:
Behrouz Shafei, Major Professor
Brent M. Phares
Jiehua Shen
Jennifer Shane
Ming-Chen Hsu

The student author, whose presentation of the scholarship herein was approved by the program of study committee, is solely responsible for the content of this dissertation. The Graduate College will ensure this dissertation is globally accessible and will not permit alterations after a degree is conferred.

Iowa State University

Ames, Iowa

2019

DEDICATION

This dissertation is dedicated to my sweet wife Chao for her unyielding love, support, and encouragement with this endeavor. To my beloved mother Tiemei, and my dearest brother Weinan, who have supported and inspired me throughout my studies.

TABLE OF CONTENTS

Page

LIST OF FIGURES

Page

LIST OF TABLES

Page

ACKNOWLEDGEMENTS

First and foremost, I would like to express my deepest gratitude to my advisor, Prof. Behrouz Shafei, for his technical guidance, valuable insight and encouragement throughout my doctoral study. Without his guidance and persistent help, this dissertation would not have been possible.

I would like to express my sincerest gratitude to Prof. Brent Phares, for the unwavering support he provided during this process. I would also like to thank Prof. Jiehua Shen, Prof. Jennifer Shane, and Prof. Ming-Chen Hsu, the members of my Ph.D. research committee, for their valuable perspective and commentary throughout my research study.

Also, I would like to express my thanks to Dr. Meysam Najimi for his knowledgeable inputs throughout this research. Special thanks to lab personnel Doug Wood, Owen Steffens, Bob Steffes, and Jeremy McIntyre for their assistance.

The Iowa Department of Transportation sponsored the research study. This support is gratefully acknowledged.

Finally, I also want to thank all the faculty, staff and my fellow students at the Civil, Construction, and Environmental Engineering Department at Iowa State University. The warmth that everyone has shown has made up for all the winter days in Ames.

ABSTRACT

Longitudinal joints used to connect adjacent box beams in bridges are known to experience cracks due to a variety of environmental and mechanical stressors, including diurnal temperature changes, hydration, drying shrinkage, restrained shrinkage, and traffic loads. Such cracks can open a direct path for water and deleterious agents to penetrate into the structural system, causing corrosion of embedded steel bars and structural degradation of bridge superstructure and substructure elements. The degradation adversely affects the integrity of the entire bridge, provokes safety and durability concerns, and eventually results in road closures and traffic disruptions due to maintenance and repair requirements.

Shrinkage-compensating cement, also known as Type K expansive agent, is a type of calcium sulfoaluminate cement with the ability of volume expansion during the early stages of hardening due to the volumetric formation of ettringite. In this way, shrinkage-compensating cement concrete (SCC-C) can significantly enhance the volume stability of concrete, increase the serviceability of the structure, and thus develop an optimized solution for cracking, especially in adjacent box beam bridges. In this study, a comprehensive experimental program was established to investigate the SCC-C from material and structural perspectives. The ultimate goal of this study is to develop recommendations for the proper use of SCC-C in longitudinal joints for adjacent box beam bridges, especially where the structural components are susceptible to both shrinkage and chloride attack.

To meet this goal, a comprehensive testing program was established to evaluate the concretes made with various dosages of Type K expansive agent (i.e., 0%, 7.5%, 15%, and 22.5% by weight of total cementitious materials) subjected to a number of mechanical,

transport, and durability assessment experiments, including compressive strength, drying shrinkage, rapid chloride penetration, rapid chloride migration, surface resistivity, absorption of water in hardened concrete, helium porosimetry, and Mercury intrusion porosimetry tests. The results indicated that the resistance of concrete to chloride ions was reduced with increasing the dosage of replacement of Type K cement. While the addition of class F fly ash led to partial mitigation of increased chloride permeability caused by the inclusion of Type K agent, the incorporation of silica fume or class C fly ash were identified as appropriate strategies for addressing the chloride permeability issue.

In addition, two full-scale box beams were designed, constructed and connected using a longitudinal joint made with Type K cement, to investigate the structural response under early-age thermal effects and cycles of structural loads. A set of three-dimensional finite-element simulations were also performed to extend the scope of investigations beyond the cases tested in the laboratory. Both experimental and numerical results indicate that the longitudinal Type K joint provides satisfactory performance in resisting joint cracks subjected to both early-age thermal effects and long-term service loads that the bridge experiences during its service life. Results from the finite element models were in a good agreement with the experimental measurements. Also, a parametric study was conducted to investigate the structural response subjected to the AASHTO-specified temperature profiles and the longitudinal joint design parameters, including different bond properties and the effect of joint reinforcement.

CHAPTER 1. INTRODUCTION

"There can be little doubt that in many ways the story of bridge building is the story of civilisation. By it we can readily measure an important part of a people's progress."

- Franklin D Roosevelt

1.1 Background

An adjacent precast concrete box beam bridge is considered a primary choice of design for short to medium-span bridges in the United States, especially on secondary roads. As can be seen in Figure 1.1, this type of bridge is generally constructed by placing box beams next to one another, grouting a shear key at their interface, applying transverse post-tensioning, then placing a thin overlay or a thick structural deck (Russell 2011). Such bridges have been adopted by multiple Departments of Transportation (DOT) because of their relatively shallow superstructure depth, their ease of construction, and their simple aesthetic attributes.

Although the structural performance of such bridges has proven to be successful, these and similar adjacent precast elements do suffer from a significant, i.e., developing reflective cracking of the deck surface and resulting leakage under the beams, providing a direct path for water and deleterious material to permeate into the structure, corrode the reinforcing and pre-stressing steel, and motivate large differential displacement between girders. This phenomenon could lead to reducing the capability of lateral connection for multiple beams and resulting in single elements being exposed to higher live loads than those for which they were designed. Such greater deflection tends to occur on single or a limited number of girders, possibly jeopardising bridges concerning both strength and serviceability performance, and ultimately possibly leading to a significant increase in maintenance costs and safety concerns. Various experimental and numerical studies have been conducted on shear keys to improve their

material performance by investigating geometrical configurations, and understanding loading transfer mechanisms, early age behavior, transverse tie effects, live loading response, etc. (Gulyas, et al., 1995; Miller 1999; Attanayake and Aktan 2008; Russell 2009; Attanayake, et al., 2010; Murphy, et al., 2010; Hanna, et al., 2011; Grace, et al., 2012; Giraldo-londoño 2014; Yuan and Graybeal 2014, 2016; Rikabi, et al., 2017).

Considering that one of the primary causes of cracking in adjacent box beam bridges is the shrinkage of materials placed in the longitudinal joints, the current study investigates the use of Type K shrinkage-compensating cement as a partial replacement of portland cement. Contrary to portland cement concrete, the shrinkage-compensating cement concrete benefits from the formation of a relatively large volume of ettringite, which counteracts shrinkage effects through early-age expansion (Ogawa 1982; Péra and Ambroise 2004). The bridge application of shrinkage-compensating cement concrete was first in bridge decks, for which the drying shrinkage cracks were found to be successfully mitigated (Gruner and Plain 1997). Folliard et al. (2003) evaluated the resistance of different concretes, such as fibre-reinforced concrete, shrinkage-compensating concrete, concrete with shrinkage-reducing admixture, and extensible concrete, to control the drying shrinkage. It was reported that the early-age expansion originated from Type K cement can provide a superior performance to overcome the shrinkage. Xi et al. (2003) conducted a study to understand the causes of early-age cracking in newly constructed bridge decks. It was found that 82% of the inspected bridge decks had various degrees of cracking and the high early age shrinkage of concrete was the main contributor to the problem.

Shrinkage-compensating cement (a.k.a., Type K expansive agent) is a calcium sulfoaluminate cement with the ability to provide volume expansion during the early age,

primarily due to the formation of ettringite. This can significantly enhance the volume stability of concrete, and thus, develop an optimized solution to increase the service life of structures. In recent years, there has been growing interest in using this type of cement (as partial replacement of portland cement) for bridge decks, parking structures, and post-tensioned structural elements (Ramseyer C, 2016; Russell, 2002; Sprinkel M, 2015). This was due to promising performance, in terms of shrinkage compensation and self-stressing characteristics, as well as an environmentally friendly manufacturing process (Han J, 2016; Ramseyer C, 2016; Péra J, 2004; Ogawa K, 1982; Rahman M, 2018; Gartner E, 2004). The main components of shrinkage-compensating cement are tetracalcium trialuminate sulfate ($4CaO{\cdot}3Al_2O_3{\cdot}SO_3$, abbreviated as C_4A_3S), anhydrite ($CaSO_4$), and lime (CaO). In the early stage of hydration, shrinkage-compensating cement (contrary to portland cement) produces large volumes of stable ettringite with the following reaction: $C_4A_4\bar{S} + 6CH + 8C\bar{S}H_2 + 71H \rightarrow 3C_6A\bar{S}_3H_{31}$, where $C_4A_4\bar{S}$ represents calcium sulfoaluminate; CH is calcium hydroxide; and $C\bar{S}H_2$ is gypsum (Péra J , 2004; Odler I, 2019; Bentur A, 1974). Ettringite ($C_6A\bar{S}_3H_{31}$) is known to be expansive with forming long needle-like crystals (Ogawa K, 1982).

1.2 Research Objectives

The primary objective of the project was to investigate an innovative longitudinal joint for adjacent box-beam bridges using SCC-C from material and structural perspectives. For this purpose, a systematic material- and structural-level studies have been performed. The outcome of this dissertation is expected to provide recommendations for the proper use of SCC-C in various structural applications, especially for longitudinal joints of adjacent box beam bridges that are susceptible to both shrinkage and chloride attack.

1.3 Research Summary

To achieve the research objectives, a comprehensive experimental program was developed. This program included small scale SCC-C samples subjected to a series of chloride transport testing, and a 31-ft. specimen made with two box beams and one longitudinal joint. The full-scale structural tests were performed to evaluate early-age thermal effects and cyclic structural loads. This research consists of experimental tests and numerical simulations performed as follows.

Although the wealth of information available on the strength, shrinkage, and hydration process of shrinkage-compensating cement concretes, very limited studies have been devoted to the investigation of their transport and corrosion properties. With the goal of obtaining an in-depth understanding of penetration of aggressive agents, particularly chloride ions, into shrinkage-compensating cement concretes, a comprehensive laboratory testing program was established to evaluate the concretes made with various dosages of Type K expansive agent (i.e., 0%, 7.5%, 15%, and 22.5% by weight of total cementitious materials) under a number of mechanical, transport, and dimensional stability experiments, including compressive strength, drying shrinkage, rapid chloride penetration, rapid chloride migration, surface electrical resistivity, air permeability, and absorption tests. The listed tests were then complemented with helium and mercury intrusion porosimetry analyses to further support the findings based on the pore structure of hardened mixtures. Corrosion testing of embedded steel reinforcements was also conducted to provide durability performance for such type of cement.

The study was then extended to investigate how the permeability of concretes made with this type of cement can be improved. For this purpose, similar tests were carried out after the addition of various supplementary cementitious materials (SCMs), such as fly ash class C, fly ash class F, and silica fume. The outcome of this study led to the identification of optimal

dosages of Type K expansive agents, as well as SCMs of choice that can be utilized for a variety of civil infrastructure applications, especially where there is a high risk of both shrinkage and chloride attack.

In addition, two full-scale box beams were built in the laboratory and connected with concrete made with a 15% replacement of portland cement with Type K shrinkage-compensating cement.

In the first test scenario, the primary focus of the investigation was on thermal effects, especially at the early age, due to a combination of diurnal temperature changes and the heat generated during cement hydration reactions. The test scenarios consisted of cycles of heating and cooling for seven days implemented immediately after the joint pour. The data collected from the experimental tests included temperature, longitudinal and transverse strain, and deflection at the joint and individual box beams. To extend the scope of investigations beyond the cases tested in the laboratory, a set of three-dimensional (3D) finite-element (FE) simulations were then established. The material model used for the longitudinal joint was developed in such a way that the effects of early-age expansion, the heat of hydration, and time-dependent mechanical properties were all taken into consideration. Upon validation of the FE model with the experimental test results, additional simulations were performed to obtain an in-depth understanding of how the joints made with Type K shrinkage-compensating cement concrete respond to extreme thermal loading scenarios, including that provided by AASHTO LRFD Bridge Design Specifications as well as two other additional temperature gradients, i.e., the highest temperature gradient recommended by AASHTO LRFD Bridge Design Specifications (TE-1) and 40 °C (104 °F), i.e., the highest temperature gradient reported from the field bridge weather monitoring data (TE-2) (White 2017)). The outcome of

this study provides an alternative solution to benefit from conventional, low-cost materials to ensure the safety and performance of box-beam bridges.

In the second scenario, the specimen was tested under structural cyclic loading aiming of investigating structural response. The data collected from the experimental tests consisted of longitudinal and transverse strain, and deflection in the joint and individual box beams due to the cyclic loading effects. A set of three-dimensional finite-element (FE) simulations was also developed with the goal of calibrating the structural performance of the Type K joint by comparing the results obtained from experimental testing, and reasonable agreement between numerical and experimental results was achieved, reflecting the accuracy of the FE modelling used to predict the behavior of such a structural system. Based upon the calibrated FE models, the further study was then extended to evaluate a series of influential parameters related to the arrangement of reinforcement in the joint as well as the interfacial contact properties. The outcome of this study is expected to identify the materials that not only improve the performance and durability of box beam bridge joints, but also facilitate the construction of bridges, especially where only limited resources are available.

1.4 Dissertation Layout

Following the introductory chapter, Chapters 2, 3, 4, and 5 are presented as journal articles. Chapter 2 provides the investigation of material properties, specifically for chloride penetration in concretes with shrinkage-compensating cement. Chapter 3 provides the investigation of the corrosion performance of embedded steel reinforcement for shrinkage-compensating cement concrete. Chapter 4 presents an experimental and numerical investigation of the structural behavior of reinforced longitudinal joints in bridges with adjacent box beams under thermal loads. Chapter 5 presents Laboratory and Numerical

Investigation of Reinforced Longitudinal Joints in Bridges with Adjacent Box Beams. This dissertation will be completed with laboratory and numerical investigation of reinforced longitudinal joints in bridges with adjacent box beams under cyclic loads. The last chapter will conclude the dissertation by providing a summary of the research results as well as recommendations for implementing longitudinal joint for adjacent box beam bridges using SCC-C.

1.5 References

Attanayake, U., and Aktan, H. (2008). "Issues with Reflective Deck Cracks in Side-by-Side Box Beam Bridge." 2008 CBC, 1, 1–18.

Attanayake, U., Ulku, E., and Aktan, H. M. (2010). "Rationally Designed Staged Posttension Abates Reflective Cracking on Side-by-Side Box- Beam Bridge Decks." Transportation Research Board 89th Annual Meeting, 1–15.

Bentur A, Ish-Shalom M. Properties of type K expensive cement of pure components II. Proposed mechanism of ettringite formation and expansion in unrestrained paste of pure expansive component. Cement and Concrete Research 1974; 4:709–21.

Giraldo-londoño, O. (2014). "Finite Element Modeling of the Load Transfer Mechanism in Adjacent Prestressed Concrete Box-Beams."

Grace, N. F., Jensen, E. A., and Bebawy, M. R. (2012). "Transverse post-tensioning arrangement for side-by-side box-beam bridges." PCI Journal, 48–63.

Gulyas, R. J., Wirthlin, G. J., and Champa, J. T. (1995). "Evaluation of keyway grout test methods for precast concrete bridges." PCI Journal, 40(1), 44–57.

Han J, Jia D, Yan P. Understanding the shrinkage compensating ability of type K expansive agent in concrete. Concrete and Building Materials 2016; 116:36–44.

Hanna, and Morcous. (2011). "Adjacent box girders without internal diaphragms or post-tensioned joints." PCI J, 51–64.

Kim, and Sang. (2010). Determining More Effective Approaches for Grouting Shear Keys of Adjacent Box Beams.

Miller, R. A. (1999). "Ful Scale Testing of Shear Keys for Adjacent Box Girder." PCI Journal.

Odler I, Colán-Subauste J. Investigations on cement expansion associated with ettringite formation. Cement and Concrete Research 1999; 29:731–5.

Rikabi, F. T. Al, Asce, S. M., Steinberg, E. P., and Asce, M. (2017). "Modeling the Shear Connection in Adjacent Box-Beam Bridges with Ultrahigh-Performance Concrete Joints I: Model Calibration and Validation." Journal of Bridge Engineering, 22(8), 1–14.

Ramseyer C. Behavior of Shrinkage Compensating Concrete in an Unrestrained and Restrained Environment. 1–20.

Russell H, Stadler R, Gelhardt H. Shrinkage-Compensating Concrete Made With an Expansive Component. Concrete International 2002; 24:107–11.

Russell. (2011). "Adjacent precast concrete bridges: State of the practice." PCI journal, 75–91.

Russell, H. G. (2009). SYNTHESIS 393 Adjacent Precast Concrete Box Beam Bridges: Connection Details.

Péra J, Ambroise J. New applications of calcium sulfoaluminate cement. Cement and Concrete Research 2004; 34:671–6.

Ogawa K. C4A3S Hydration, Ettringite Formation, and Its Expansion Mechanism: II. Microstructural Observation of Expansion 1982; 12.

Rahman M, Chen Y, Lindquist W, Ibrahim A, Hindi R. Mitigation of Shrinkage Cracking in Bridge Decks Using Type-K Cement Mohammad 2018:133–44.

Gartner E. Industrially interesting approaches to "low-CO2" cements. Cement and Concrete Research 2004; 34:1489–98.

Sprinkel M. Final Report Latex-Modified Concrete Overlay Containing Type K Cement 2015.

Yuan, and Graybeal. (2014). "Adjacent box beam connections." PCI National Bridge Conference, Precast/prestressed Concrete Insitute, Chicago, 1–28.

Yuan, J., and Graybeal, B. (2016). "Full-Scale Testing of Shear Key Details for Precast Concrete." Journal of Bridge Engineering.

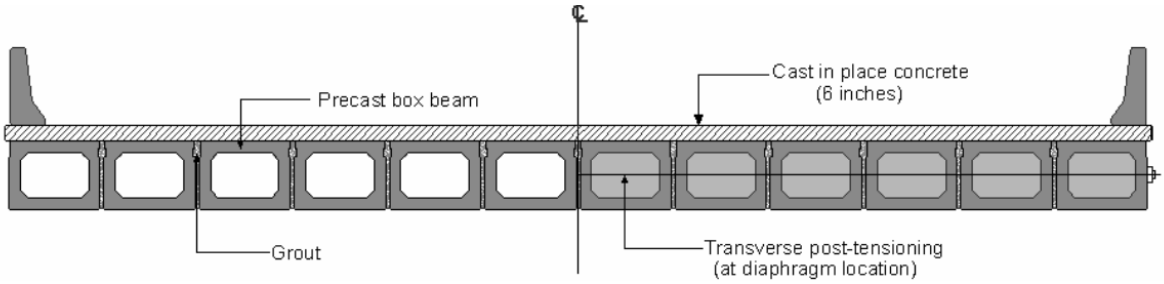

Figure 1.1 Typical configurations of side-by-side box-beam assemblages used in the US (Attanayake and Aktan 2008)

CHAPTER 2. INVESTIGATION ON CHLORIDE PENETRATION IN SHRINKAGE-COMPENSATING CEMENT CONCRETES

2.1 Abstract

Shrinkage-compensating cement (a.k.a., Type K expansive agent) is a calcium sulfoaluminate cement with the ability to provide volume expansion during the early age, primarily due to the formation of ettringite. This can significantly enhance the volume stability of concrete, and thus, develop an optimized solution to increase the service life of structures. Despite the past studies on the strength, shrinkage, and hydration of shrinkage-compensating cement concretes, there was no systematic investigation to understand the performance of this type of concrete under exposure to aggressive agents, particularly chloride ions. To address this gap, a comprehensive testing program was established in this study to evaluate the mechanical, transport, and dimensional stability properties of concretes made with various dosages of Type K expansive agent (i.e., from 0% to 22.5% by weight of total cementitious materials). This includes compressive strength, drying shrinkage, rapid chloride penetration, rapid chloride migration, surface electrical resistivity, and absorption tests. Both helium and mercury intrusion porosimetry analyses were also conducted to further support the experimental test results with the findings related to the distribution of pores. The results of this study confirmed the benefits of using Type K expansive agent (up to a certain dosage) in terms of increased compressive strength and reduced drying shrinkage. However, it was revealed that the permeability of concretes made with this type of cement is adversely affected. This issue was addressed by the identification of optimal dosages of supplementary cementitious materials, including fly ash and silica fume. Upon completing the necessary experiments on the improved mixtures, this study reported how low-shrinkage concretes with

low susceptibility to chloride penetration can be developed with the promise of application in a wide variety of civil infrastructures exposed to harsh environmental conditions.

Keyword: Shrinkage-Compensating Cement Concrete; Type K Expansive Agent; Chloride Penetration; Mechanical and Transport Properties; Supplementary Cementitious Materials.

2.2 Introduction

Cracks in concrete, particularly due to restrained shrinkage, have long been an issue of concern for those involved in the construction and maintenance of concrete structures. The formation and propagation of cracks in concrete often lead to strength and durability problems, as cracks permit the ingress of water and chloride ions towards embedded reinforcement. Among possible solutions, shrinkage-compensating cement (a.k.a., Type K expansive agent) has been reported to mitigate autogenous and drying shrinkage, leading to enhanced volumetric stability for concrete (ACI 2010; Chaunsali and Mondal 2016; Han et al. 2016; Klein et al. 1961; Mather 1970; Nair et al. 2016; Portland Cement Association 2002). In recent years, there has been growing interest in using this type of cement (as partial replacement of portland cement) for bridge decks, parking structures, and post-tensioned structural elements (Ramseyer n.d.; Russell et al. 2002; Sprinkel 2015). This was due to promising performance, in terms of shrinkage compensation and self-stressing characteristics, as well as an environment friendly manufacturing process (Gartner 2004; Han et al. 2016; Ogawa 1982; Péra and Ambroise 2004; Rahman et al. 2018; Ramseyer n.d.). The main components of shrinkage-compensating cement are tetracalcium trialuminate sulfate ($4CaO{\cdot}3Al_2O_3{\cdot}SO_3$, abbreviated as $C_4A_3\bar{S}$), anhydrite ($CaSO_4$), and lime (CaO). In the early stage of hydration, shrinkage-compensating cement (contrary to portland cement) produces large volumes of stable ettringite with the following

reaction: $C_4A_4\bar{S} + 6CH + 8C\bar{S}H_2 + 71H \rightarrow 3C_6A\bar{S}_3H_{31}$, where $C_4A_4\bar{S}$ represents calcium sulfoaluminate; CH is calcium hydroxide; and $C\bar{S}H_2$ is gypsum (Bentur and Ish-Shalom 1974; Odler and Colán-Subauste 1999; Péra and Ambroise 2004). Ettringite ($C_6A\bar{S}_3H_{31}$) is known to be expansive with forming long needle-like crystals (Ogawa 1982).

Table 2.1 provides a summary of past research investigations conducted on this type of cement. Among the past studies, Han et al. (2016) investigated both shrinkage and compressive strength of shrinkage-compensating cement concretes at 3, 7, and 28 days after casting and reported that the addition of Type K expansive agent could reduce the drying shrinkage with no adverse effects on mechanical properties. Pera and Ambroise (2004) also observed a promising development of compressive strength at the age of 1 to 60 days, while shrinkage was limited because of using calcium sulfoaluminate cement. Ramseyer et al. (2018) conducted a study on ground slabs to understand the shrinkage behavior of shrinkage-compensating cement concretes for in-situ applications. With an overall expansion of the slab, it was found that the expansion and shrinkage were both limited under the restrained condition. Rahman et al. (2018) investigated the effects of Type K cement on the shrinkage cracking of bridge decks. The study involved both laboratory and field investigations to understand the expansion and shrinkage behavior. Results from longitudinal and transverse strain measurements showed that the compressive stresses induced by early-age expansion can counteract the tensile stresses originated from the drying shrinkage, thus, help minimize early-age cracks.

Table 2.1 Previous research studies of using SCC-C.

Property	Experiments	Type of cementitious composite		Major findings
		Paste/mortar	**Concrete**	
Fresh Properties	Slump Flow	ACI (ACI 2010)	Battaglia (Battaglia 2012); Mather (Mather 1970); ACI (ACI 2010); Walkowich (Walkowich 2011); Moffat (Moffat 2005); Gress (Gress 2001); Sprinkel (Sprinkel 2005); D'Ambrosia (D'Ambrosia et al. 2013); Chaunsali (Chaunsali et al. 2013); Ramey (Ramey et al. 1997); Nair (Nair et al. 2016); Carballosa (Carballosa et al. 2015); Calvo (Calvo et al. 2017)	Workability loss
	Workability loss		Mather (Mather 1970); Han (Han et al. 2016); Calvo (Calvo et al. 2017)	
	Air content	ACI (ACI 2010)	Walkowich (Walkowich 2011); Sprinkel (Sprinkel 2005); Ramey (Ramey et al. 1997); D'Ambrosia (D'Ambrosia et al. 2013); Gress (Gress 2001); Moffat (Moffat 2005); Mather (Mather 1970); ACI (ACI 2010); Nair (Nair et al. 2016); Carballosa (Carballosa et al. 2015); Calvo (Calvo et al. 2017)	
	Setting time	Sarkar (Sarkar 1990), ACI (ACI 2010)	Ramey, 1997; D'Ambrosia (D'Ambrosia et al. 2013); ACI (ACI 2010)	
Hydration	Heat of hydration	Chaunsali (Chaunsali et al. 2013); Han (Han et al. 2016); Sarkar (Sarkar 1990);	Han (Han et al. 2016)	Higher heat generation
Mechanical Properties	Compressive strength	ACI (ACI 2010)	D'Ambrosia (D'Ambrosia et al. 2013); Walkowich (Walkowich 2011); Matter (Mather 1970); Chaunsali (Chaunsali et al. 2013); Ramey (Ramey et al. 1997); Sprinkel (Sprinkel 2005); Ramseyer (Ramseyer 2016); ACI (ACI 2010); Nair (Nair et al. 2016); Carballosa (Carballosa et al. 2015); Han (Han et al. 2016); Calvo (Calvo et al. 2017)	No negative effect on strength properties
	Tensile strengths	–	Walkowich (Walkowich 2011); Ramey (Ramey et al. 1997); Moffat (Moffat 2005); Nair (Nair et al. 2016)	
	Modulus of elasticity	–	Walkowich (Walkowich 2011); Ramey (Ramey et al. 1997); Moffat (Moffat 2005); D'Ambrosia (D'Ambrosia et al. 2013); Matter (Mather 1970); Nair (Nair et al. 2016); Han (Han et al. 2016)	
	Bond strength	–	Sprinkel (Sprinkel 2005); Matter (Mather 1970)	

Table 2.1 Continued

Property	Experiments	Type of cementitious composite		Major findings
		Paste/mortar	**Concrete**	
Transport Properties	Rapid chloride penetration	–	Battaglia (Battaglia 2012)	Lack of data, Conflicting observations
	Rapid chloride migration	–	–	
	Chloride diffusion	–	Battaglia (Battaglia 2012); D'Ambrosia (D'Ambrosia et al. 2013); Sprinkel (Sprinkel 2005)	
	Water permeability	–	Sprinkel (Sprinkel 2005); Moffat (Moffat 2005); Nair (Nair et al. 2016)	
	Absorption	–	–	
	Capillary absorption	–	–	
	Gas permeability	–	–	
	Electrical resistivity	–	–	
Durability Properties	Frost resistance	–	D'Ambrosia (D'Ambrosia et al. 2013); Sprinkel (Sprinkel 2005); Matter (Mather 1970); Nair (Nair et al. 2016)	Not studied properly
	Sulfate attack	–	–	
	Acid attack	–	–	
	Chloride-induced corrosion	–	–	
	Alkali-silica reactivity	–	–	
	Carbonation	–	–	
	Abrasion	–	–	

Table 2.1 Continued

Property	Experiments	Type of cementitious composite		Major findings
		Paste/mortar	**Concrete**	
Dimensional Stability	Drying shrinkage	Chaunsali (Chaunsali et al. 2013); Ramseyer (Ramseyer 2016)	Walkowich (Walkowich 2011); Chaunsali (Chaunsali et al. 2013); Ramseyer (Ramseyer 2016); Sprinkel (Sprinkel 2005); Ramey (Ramey et al. 1997); D'Ambrosia (D'Ambrosia et al. 2013); Gress (Gress 2001); ACI (ACI 2010); Ramseyer (Ramseyer 2016); Nair (Nair et al. 2016); Carballosa (Carballosa et al. 2015); Han (Han et al. 2016)	Reduced drying and restrained shrinkage. Not studied for plastic shrinkage
	Chemical and plastic shrinkage	–	–	
	Autogenous shrinkage	–	Han (Han et al. 2016)	
	Restrained shrinkage	Ramey (Ramey et al. 1997); ACI (ACI 2010)	Matter (Mather 1970); Battaglia (Battaglia 2012); Walkowich (Walkowich 2011); Chaunsali (Chaunsali et al. 2013); Valenene, (Valenene 2002); Ramey (Ramey et al. 1997); D'Ambrosia (D'Ambrosia et al. 2013); Gress (Gress 2001); ACI (ACI 2010); Ramseyer (Ramseyer 2016); Nair (Nair et al. 2016); Carballosa (Carballosa et al. 2015); Han (Han et al. 2016); Calvo (Calvo et al. 2017)	
	Creep	–	Moffat (Moffat 2005)	

Despite the fact that the wealth of information available on the strength, shrinkage, and hydration process of shrinkage-compensating cement concretes, very limited studies have been devoted to the investigation of their transport properties. It can be observed in this table that one of the critical aspects that have not been studied in depth is the transport properties of the concrete mixtures made with shrinkage-compensating cement. Battaglia (2012) studied the concrete permeability by performing the rapid chloride penetration test (RCPT) according to AASHTO T277-15 (AASHTO T277-07 2006). It was found that the mixtures made with Type K expansive agent had a chloride permeability close to twice of those made with Type I cement. D'Ambrosia (2013) and Nair (2016) also indicated that due to concerns regarding high permeability and risk of corrosion, the use of Type K cement was stopped in several states that had used it in the past. This issue was then explored in a separate study by Sprinkel (2015). With a focus on latex-modified concrete overlays, chloride permeability was evaluated and compared with Type I/II cement. The outcome of the latter study, however, was not consistent with Battaglia (2012), as the chloride permeability was reported to be in the range of very low to negligible for all the tested mixtures. In the absence of reliable findings in the literature, a holistic study on the transport properties of concretes made with Type K expansive agent was deemed essential.

It is demonstrated that a 15-17% replacement of cement content is sufficient to achieve shrinkage compensation to assists engineers in determining the most effective dosage for the project (Foster-Goodman and Vallens 2018). With the goal of obtaining an in-depth understanding of penetration of aggressive agents, particularly chloride ions, into shrinkage-compensating cement concretes, a comprehensive laboratory testing program was established to evaluate the concretes made with various dosages of Type K expansive agent (i.e., 0%,

7.5%, 15%, and 22.5% by weight of total cementitious materials) under a number of mechanical, transport, and dimensional stability experiments, including compressive strength, drying shrinkage, rapid chloride penetration, rapid chloride migration, surface electrical resistivity, and absorption tests. The listed tests were then complemented with helium and mercury intrusion porosimetry analyses to further support the findings based on the pore structure of hardened mixtures. The study was then extended to investigate how the permeability of concretes made with this type of cement can be improved. For this purpose, similar tests were carried out after the addition of various supplementary cementitious materials (SCMs), such as fly ash class C, fly ash class F, and silica fume. The outcome of this study led to the identification of optimal dosages of Type K expansive agents, as well as SCMs of choice that can be utilized for a variety of civil infrastructure applications, especially where there is a high risk of both shrinkage and chloride attack.

2.3 Experimental Program

Two series of experiments were performed in the current study. The first series was designed to investigate the permeability of shrinkage-compensating cement concrete mixtures with different dosages of Type K expansive agent. Upon understanding the adverse effects of replacing portland cement with shrinkage-compensating cement on transport properties, the second series of experiments were planned to evaluate how the incorporation of SCMs can reduce the penetration of water and chloride ions into concretes containing this type of cement.

2.3.1 Materials

This study used two types of cement, including Type I portland cement and shrinkage-compensating cement. For the second series of mixtures, three SCMs, including fly ash class C, fly ash class F, and silica fume were used. The chemical composition of these binders is

provided in Table 2.2. The aggregates used for the mixtures included fine aggregates (0 to 4.75 mm) and coarse aggregates (4.75 to 25 mm), in accordance with the gradation size requirements of ASTM C33 (2013). The physical properties of fine and coarse aggregates are reported in Table 2.3. A high-range water-reducing admixture (HRWR) was used only for the mixtures that contained silica fume to maintain the workability in a target range of 14 ± 4 cm.

2.3.2 Mixture Proportions

The mixture proportions of the concrete tested in the current study have been summarized in Table 4. In the first series of tests, Type I portland cement was replaced with four dosages of Type K expansive agent, including 0%, 7.5%, 15%, and 22.5%. To reflect no, low, medium, and high dosage of replacement, these mixtures have been labeled in Table 2.4 as Control, KL, KM, and KH, respectively. The second series of mixtures were developed on the basis of KM mixture and additionally included 15% fly ash class C, 15% fly ash class F, and 7.5% silica fume. They have been labeled in Table 4 as KM+FAF, KM+FAC, and KM+SF, respectively. The water-to-cementitious materials ratio (*w/c*) for all the mixtures designed for this investigation was selected as 0.5.

2.3.3 Mixing, Sampling, and Testing

Concrete specimens were mixed by a drum mixer with the capacity of 0.1 m^3 following the mixing procedures provided in ASTM C192 (2002). The slump of each concrete mixture was measured based on ASTM C143 (2015). The hydration heat release rate was evaluated with the isothermal heat conduction calorimetry. A number of cylindrical and prism-shaped specimens were cast for the measurement of hardened properties. The cylindrical specimens were 100 mm × 200 mm. After consolidating by a vibrating table, the specimens were covered and maintained at the room temperature for the first 24 hours. They were then removed from

their molds and stored in a standard moist room at a temperature of 23 ± 2 ℃ until the testing time.

Of the prepared cylindrical specimens of each mixture, four were used to measure the compressive strength according to ASTM C39 (2016). The rest of cylinders were used to assess the transport properties of concrete mixtures. The electrical resistivity of concrete was measured on 100 mm × 200 mm cylinders using a four-point Wenner array probe following FM 5-578 (FM 5-578 2004). For the measurement of the other transport properties, disc samples with a diameter of 100 mm and a thickness of 50 mm were cut from the cylinders. The disc samples (4 samples for each test) were then conditioned to prepare them for rapid chloride penetration, rapid chloride migration, water absorption, density and volume of permeable pore space, helium porosimetry, and mercury intrusion porosimetry tests. In addition, the length change in four beam-shaped specimens was measured from day 1 to 56 to assess the volumetric expansion/contraction of different mixtures according to ASTM C157 (2016). The shrinkage specimens were maintained in the curing room for 7 days before transferring them to the shrinkage room with a temperature of 23 ± 2 ºC and a relative humidity of 50 ± 4%. This test was completed to further quantify the extent of shrinkage compensation in the mixtures under consideration with and without SCMs.

RCPT is commonly used for a rapid characterization of the penetrability of chloride ions into the concrete. This test was conducted on all the mixtures according to ASTM C1202 (2012), which instructs to monitor the amount of electrical current passed through concrete disk samples. The current measured over time was then used to calculate the passed charge (in coulombs). Five categories of high, moderate, low, very low, and negligible were employed to determine the level of chloride ion penetrability. On the other hand, the rapid chloride

migration test, which was conducted according to NT BUILD 492 (1999), measured the depths of chloride penetration and reported the chloride migration coefficient. For the purpose of RCMT, a voltage of 30V was applied to the samples placed between sodium chloride and sodium hydroxide solutions for 24 hours. After testing each group of four concrete samples using the developed RCMT setup, all of them were split and sprayed with $AgNO_3$ solution (0.1 M), which acted as a colorimetric indicator. This provided a detailed assessment of penetrability of chloride ions into the concrete mixtures under consideration. The water absorption, as well as density and volume of permeable pore space, were also determined according to ASTM C642 (2008). For this purpose, the change in the mass of samples subjected to different moisture conditions, such as dry, immersed, and boiled, was recorded.

The helium porosimetry experiment was carried out on the same samples of water absorption test to quantify the total porosity. This test was performed by applying a known volume of helium gas to the samples until the equilibrium pressure was reached. Based on the principle of gas expansion, as described by Boyle's law, the resultant stabilized pressure was measured to predict the volume of voids in the samples. Furthermore, mercury intrusion porosimetry (MIP) was conducted to assess the distribution of pore sizes by injecting mercury into the samples with an increasing pressure. MIP is a powerful technique that provides detailed information regarding porosity, pore size distribution, and pore volume. With the MIP test, the pore structure of the concrete mixtures was investigated by injecting mercury into the samples with increasing the applied pressure. This measures the porosity of the mixtures by evaluating the pore-throat size that corresponds to each pressure change (Giesche 2006). This test determines the pore distribution in a wide range of pore diameters from 3 nm to 200 μm. In this research study, a Quantachrome PoreMaster 33 was used to measure the porosity as

well as the distribution of the pore sizes. Each sample (Control, KM, and KM+SF) was oven-dried for 12 hours at 100 °C and stored in a desiccator at room temperature for 24 hours before the test was performed. The range of temperature for conducting the MIP was between 24°C and 28°C. The following parameters were specified in the MIP test: a mercury contact angle of 140.00° (intrusion and extrusion), a mercury surface tension of 480.00 erg/cm^2, fine evacuation until 2 minutes (LP experiment), coarse evacuation until 3 minutes (LP experiment), and fill contact pressure of +1 to +3 psi (+7 to +21 kPa, LP experiment). The equivalent pore diameter can be calculated by the Washburn equation (Eq. 1) for non-wetting liquid penetration:

$$D = \frac{-4\gamma\cos\theta}{P} \quad (1)$$

where P is the applied pressure (in Pa); D is the pore diameter (in μm); γ is the surface tension of the mercury; and θ is the contact angle between the mercury and the mixture. In this study, a Quantachrome PoreMaster 33 was used for measuring mercury intrusion.

2.4 Assessment of Fresh, Strength, and Dimensional Stability Properties

2.4.1 Heat of Hydration

The process of heat generation as a result of hydration reactions at an early age can be commonly classified into five stages of initial, induction (dormant), accelerated, decelerated, and slow reaction periods (Winnefeld and Lothenbach 2010). These five reaction periods for the cement pastes containing different dosages of Type K expansive agent have been determined from the isothermal heat conduction calorimetry. According to Figure 2.1, when the dosage of Type K expansive agent was increased, the peak of the initial reaction period was increased as well. This can be attributed to the reaction of the main component of Type K

expansive agent, i.e., $C_4A_3\bar{S}$, with CH and $C\bar{S}H_2$, which results in the formation of ettringite (Grusczscinski et al. 1993). During the induction period, the rate of heat generation was higher in all the Type K expansive agent-contained pastes than the control paste. It was found that this trend is reversed within the accelerated reaction period, in which a time difference of up to 2 hours is recorded between the peak of KH mixture and the control mixture. This can be because the main components of Type K cement reacted within the first 8 hours, and thus, the process of ettringite formation dissipated significant thermal energy (Kaufmann et al. 2016).

2.4.2 Workability

The slump measurements have been reported in Table 2.5. Although the slump of all the mixtures was in an adequate range to allow proper compaction, there was an overall reduction of flow with the addition of Type K expansive agent. As it can be seen in this table, the slump was decreased from 16.5 cm to 10.2 cm with increasing the dosage of Type K expansive agent from 0% to 22.5%. A similar slump loss was also reported by Nair (Sprinkel 2015), which can be related to the physicochemical processes, through which ettringite is formed during early hydration reactions in the cement paste (Mehta 1973). The SCMs that were used in the second series of mixtures, however, had different effects on the workability of shrinkage-compensating cement concretes. While the flow was improved by using fly ash class F, fly ash class C had negligible effects on the slump. On the other hand, the addition of silica fume considerably reduced the flow, which was compensated by the inclusion of HRWR. It should be mentioned that no water reducer was used in the tested mixtures, except for those containing silica fume.

2.4.3 Compressive Strength

The compressive strength test results for all the concrete mixtures at the age of 28 days have been included in Table 2.5. An increasing 28-day compressive strength was observed up to the 15% dosage of Type K expansive agent, after which a sudden drop occurred. The average compressive strength of concrete mixtures with 7.5% and 15% Type K expansive agent was 13.9% and 13.1% higher than that of concrete made only with portland cement (i.e., control mixture), respectively. It is important to note that the concrete strength significantly decreased when the 22.5% dosage of Type K expansive agent was used. This was due to excessive expansion that had destructive structural effects and weakened the bond between the coarse aggregates and the mortar. This is reflected in the zoomed-in picture of KH mixtures taken at the age of 28 days (Figure 2.2).

The compressive strengths of KM mixtures made with and without SCMs can be compared in Table 2.5. A slight decrease in compressive strength was observed when 15% of portland cement was replaced by fly ash class F, while there was no apparent difference between the compressive strength of KM and KM-FAC. This finding can be related to the late pozzolanic reactivity of fly ash class F, which in fact, reduced the compressive strength at an early age. However, the compressive strength was found to be the highest with the inclusion of silica fume. This can be attributed to the extreme fineness of silica fume and its very high amorphous silicon dioxide content (Rashad et al. 2014).

2.4.4 Length Change Measurements

The shrinkage-compensating behavior of Type K expansive agent originates from the formation of expansive ettringite, assuming that a proper wet curing condition is present. In general, most of early-age cracking is introduced by tensile stresses caused by the restrained

drying shrinkage of concrete. Type K expansive agent, however, introduces compressive stresses by increasing volume at the early age, which can compensate tensile stresses, leading to reduce (or eliminate) the effects of drying shrinkage. To evaluate and quantify how Type K expansive agent influences length change, four beam specimens for each mixture were cast and cured in the moist room for seven days. The length change was then measured and compared according to ASTM C157. Figure 2.3(a) presents the length change measurement for different dosages of Type K expansive agent from the first day after demolding for 56 days. This includes one measurement every day in the first seven days and one measurement every seven days after the first week. As indicated in this figure, the control mixture that had no Type K expansive agent did not experience any expansion in the first seven days in the curing room. This mixture experienced a drying shrinkage of more than 0.04% after eight weeks. However, the mixtures that contained Type K expansive agent experienced significant expansion within the first seven days in the curing room. The overall length change of KL and KM mixtures was an expansion of 0.020% and 0.060% after seven days and -0.023% and 0.001% after 56 days, respectively. This confirms that with an early expansion, the KM mixture is capable of fully compensating the destructive tensile stresses due to drying shrinkage. In the case of mixtures containing 22.5% Type K expansive agent, a considerably high residual expansion (of more than 0.22%) was observed after 56 days. This level of expansion is expected to contribute to the weakening of the bond between the coarse aggregates and the mortar, adversely affecting the compressive strength, as reported in Table 2.5.

Furthermore, the length change measurement for the mixtures with and without SCMs is presented in Figure 2.3(b). It can be seen that all the mixtures with SCMs experienced expansion in the first seven days in the curing room. The expansion was 0.040%, 0.065%, and

0.030% for KM-SF, KM-FAF, and KM-FAC, respectively. This indicates that the use of SCMs had a negligible influence on the expansion of shrinkage-compensating cement mixtures. The results also indicated that the overall length change remains minimal after 56 days (i.e., in the range of 0.025%).

2.5 Investigation of Chloride Penetration

2.5.1 Rapid Chloride Penetration

Figure 2.4 shows the RCPT results, in terms of total charge passed through the mixtures with different dosages of Type K expansive agent with and without SCMs. Considering that Type K expansive agent is much less alkaline than regular portland cement (as can be confirmed in (Kurtis 1999) and as can be seen in Table 2.2 when comparing 0.1% K_2O of shrinkage compensating cement with 0.1% Na_2O and 0.65% K_2O of Portland cement as the primary alkaline ions affecting passing charges through RCPT), a drop in the passing charge was originally expected due to the reduced alkalinity of the pore solution (Ghafoori et al. 2017). However, it can be seen in Figure 4(a) that when the dosage of Type K expansive agent was increased, the charge passed through the disc specimens increased from 3000 coulombs for the control mixture to 3200 and 3800 coulombs for KL and KM mixtures, respectively. This can be explained with the negative effect of Type K expansive agent on the microstructure of mixtures (as further elaborated in Sections 5.1 and 5.2), from which it showed higher porosity than portland cement concrete and outweighed the alkalinity effect. In the case of KH mixture, the passed charge was considerably high, resulting in an electrolyte overflow. Thus, no charge was reported for the KH mixture. This highlights the importance of dosage of Type K expansive agent in governing the chloride ion penetration.

Based on the results shown in Figure 2.4(b), with the addition of SCMs to the mixtures, the charge passed through the disc specimens decreased. This initiated from 3800 coulombs for the KM mixture to 2471, 1572, and 891 coulombs for KM-FAF, KM-FAC, and KM-SF, respectively. The observed reduction is an indication of improved resistance to chloride ion penetration after the inclusion of SCMs. More specifically, SCMs usually consume $Ca(OH)_2$ and reduce the amount of hydroxyl ions in the pore solution. Hence, the SCMs with a high pozzolanic activity can significantly decrease OH^- and reduce RCPT results. As there are some debates on how RCPT results should be interpreted, rapid chloride migration test has also been performed in the current study (see Section 4.3).

2.5.2 Concrete Electrical Resistivity

Similar to RCPT, the electrical resistivity test has been widely used as an indicator of concrete resistance to chloride ion penetration. In this test, the ionic mobility is evaluated within the pore solution of concrete mixtures. Figure 2.5 presents the results for the concrete's electrical resistivity of the mixtures with and without Type K expansive agent and those with and without SCMs. As shown in Figure 2.5(a), the average electrical resistivity measured for the mixtures that contained Type K expansive agent was lower than that of the control mixture. The reduction in resistivity was negligible when only 7.5% of portland cement was replaced with Type K expansive agent. The resistivity, however, further dropped as the dosage of Type K expansive agent increased to 15% and 22.5%. This observation was consistent with the RCPT results presented in Figure 2.4.

Figure 2.5(b) shows that the electrical resistivity increased when the SCMs were included. Class F fly ash was able to fully compensate the reduction in resistivity due to the use of Type K expansive agent. Use of fly ash class F and C was considerably helpful, as they

increased the resistivity by 26% and 82%, respectively. The measured electrical resistivity increased to 35 kohms.cm for the KM-SF mixture, indicating that the inclusion of silica fume can significantly improve the electrical resistivity of concrete when shrinkage-compensating cement is included. This observation can be due to the fact that silica fume significantly reduces the porosity of concrete compared to the other pozzolanic materials. The reduction of conductivity as a result of the consumption of available calcium hydroxide is also another significant contributor to increased resistivity after the addition of SCMs.

2.5.3 Rapid Chloride Migration

Considering that rapid chloride migration test (RCMT) is devised as a reliable accelerated test to measure the chloride permeability of concrete, the current study utilized the RCMT to complement the findings from RCPT and electrical resistivity tests. Figure 6 presents the measurements of chloride penetration depth for each series. Despite the fact that the chloride penetration fronts get unavoidably distorted due to the presence of coarse aggregates, the overall chloride penetration depth can be estimated based on the depth, through which the specimen turns white, as an indicator of AgCl precipitation. For accuracy, the depth of penetration was measured at 7 locations for each specimen. Given the measured distance and other experimental setup details, i.e., concentrations of anolyte and catholyte, the non-steady-state chloride migration coefficient was calculated according to Eq. 2 (NT BUILD 492 1999).

$$D_{\mathrm{nssm}} = \frac{0.0239(273+T)L}{(U-2)t}\left(x_{\mathrm{d}} - 0.0238\sqrt{\frac{(273+T)Lx_{\mathrm{d}}}{(U-2)}}\right) \qquad (2)$$

where D_{nssm} is the non-steady-state migration coefficient ($\times 10^{-12}$ m^2/s); U is the absolute value of the applied voltage (V); T is the average value of the initial and final temperatures in the anolyte solution (℃); L is the thickness of the specimen (mm); x_{d} is the average value of the penetration depths (mm); and t is the test duration (hour).

Figure 2.7 shows the measured chloride ion penetration depths and their associated chloride migration coefficients for both series of mixtures. As shown in Figure 2.7(a), the depth of chloride ion penetration was ranging from 24.2 mm to 42.0 mm, reflecting a 75% increase as the dosage of Type K expansive agent was increased from 0% to 15%. It should be noted that this figure does not include the measurements for the KH mixture, as chloride ions were found to penetrate all the way through the entire thickness of the specimens. The trend observed in Figure 2.7(a) is in a good agreement with those obtained from the previous tests. Accordingly, the calculated chloride migration coefficient was increased from 11.47×10^{-12} m^2/s to 20.73×10^{-12} m^2/s as the dosage of Type K expansive agent was increased from 0% to 15%.

According to Figure 2.7(b), the measured depth of chloride ion penetration has a noticeable decrease as the SCMs were added to the mixtures. More specifically, the incorporation of fly ash class C and silica fume in the mixture led to superior performance by reducing the chloride penetration depth by more than 30% and 53% of that measured for the KM mixture, respectively. Likewise, the calculated chloride migration coefficient was dropped by 55% and 65% with the use of fly ash class C and silica fume, respectively. A comprehensive review of results collected from the three tests performed to investigate the transport properties of mixtures containing Type K expansive agent confirms the choice of SCMs identified in the current study as a potential solution to improve the chloride permeability of concretes made with shrinkage-compensating cements.

2.6 Water Absorption and Porosimetry Analysis

2.6.1 Water Absorption and Helium Porosimetry

The water absorption test has been commonly used to estimate the absorption and total porosity of concrete. Table 2.6 presents the water absorption test results for the concrete specimens containing different dosages of Type K expansive agent with and without SCMs. This excludes the KH mixture, which was found to have a noticeable weak interface between the coarse aggregates and the mortar matrix (as shown in Figure 2.2). According to Table 6, while the absorption and pore volume of the KL mixture was slightly higher than those of the control mixture, the pore volume of the concrete mixture with 15% Type K expansive agent was close to 50% higher than that of the control mixture, which had no Type K expansive agent. This result was supportive of the findings from the other experiments, which indicated that water absorption increases with an increase of the dosage of Type K expansive agent.

Use of SCMs considerably reduced the absorption and pore volume of the mixtures with Type K expansive agent. The pore volume of the mixtures with fly ash class C and F were 15.5% and 16.4%, respectively, which were 16% and 21% lower than that of the KM mixture, respectively. The reduction of water absorption and volume of permeable pore space in concrete after the addition of SCMs can be attributed to not only the refinement of the pore structure as a result of pozzolanic reactions, but also the filler effect of small particles. Figure 8 provides a comparison between the results obtained from the water absorption and helium porosimetry tests. Helium porosimetry was performed because helium is considered a monomolecular gas with an atomic diameter smaller than water, which allows it to penetrate into smaller pores in concrete (Krus et al. 1997). It can be observed that the volume of pores measured in the latter test is consistent with that obtained from the water absorption test, in which the use of Type K expansive agent increased the pore volume, and the addition of SCMs

decreased the pore volume of the tested mixtures. It should be noted that the volume of pores measured with the helium porosimetry was consistently lower than that determined from the water absorption test. As elaborated in Hearn and Bamforth (Bamforth 1987; Hearn et al. 2006), this can be due to the moisture content of the concrete mixture that reduces the volume of pores in the helium porosimetry test, although the samples are expected to be dried for several days before the test. Another possible reason is that the applied pressure is relatively low (approximately 0.15 MPa), which may not be sufficient for the intrusion of the helium gas into all the pores (Journal et al. 2010).

2.6.2 Mercury Intrusion Porosimetry

A review of Figure 2.4 and Figure 2.7, as well as Table 2.6, shows that the results from rapid chloride penetration and rapid chloride migration tests on the mixtures containing SCMs were lower than those obtained for the control mixture. Although the total porosity is one of the main properties of the concrete's microstructure, the pore structure and size distribution in the concrete matrix plays a critical role in the transport properties of concrete. This is due to the fact that a fraction of the pore space, as well as other pores in the form of dead-ends, are not accessible, and thus, cannot contribute to the transport of water and aggressive agents (Garboczi 1990). To further investigate this aspect, the MIP test was carried out on the control, KM, and KM-SF mixtures.

Figure 2.9 shows the pore size distributions of the concrete samples taken from the control, KM, and KM-SF mixtures. The results demonstrate the pore size distribution of each sample and the area under each curve indicates the total porosity. It can be noted that the presence of Type K expansive agents increased the porosity of the tested samples (from 0.68 to 0.77 cm^3/gram), which can be translated to an expedited transport of water and aggressive

agents. On the other hand, the addition of silica fume decreased the porosity (from 0.77 to 0.66 cm^3/gram), which was consistent with the other reported findings.

Since the rate of ion transport is governed by interconnected pore space, the pore size distribution of the hardened mixtures can be employed to evaluate the transport properties. With the goal of obtaining a detailed insight into the porosity of the tested mixtures, the measured mercury intrusion values were divided into four pore diameter categories: (i) gel pores (interlayer CSH, below 0.01 μm), (ii) capillary micropores (mesopores, 0.01 to 0.05 μm), (iii) capillary macropores (large mesopores, 0.05 to 10 μm), and (iv) entrained/entrapped air voids (above 10 μm). Among them, capillary pores are known to have the most significant impact on the permeability of concrete. As shown in Figure 10, the volume of mercury intrusion into the pore sizes of 0.01 to 10 μm (i.e., both capillary micropores and macropores) is 0.72 cm^3/gram for the KM mixture, in comparison with 0.67 and 0.61 cm^3/gram for the Control and KM-SF mixtures, respectively. A similar trend can also be seen for entrained/entrapped air voids (pore sizes of above 10 μm). The MIP results were found to be in a good agreement with the other test results, confirming the effectiveness of the identified mixture alternative in delivering both shrinkage compensation and chloride resistance characteristics.

These porosimetry features, observed in water absorption, helium and mercury intrusion porosimetry, are due to the expansive phenomena resulted from Type K expansive agents. According to the study conducted by Le Saoût (Le Saoût et al. 2013), in which the backscattered electron image (SEM-BSE) was performed on the polished surfaces of concrete hydrated for 28 days, it was found that significantly more hollow shell hydration grains (a.k.a., Hadley grains) were present in Type K cement concrete than portland cement concrete. The

observation of more Hadley grains can indicate more pores developed between the cement core and the layer of reaction product formed around the cement grain surface (Scrivener 2004). This may be due to more aluminate phase, and the amount of sulfate phase presented in more of ettringite in Type K cement concretes than portland cement concretes, by which the distance was separated between the solid particles and thus the porosity of the hydrated system increases (Glasser and Zhang 2001; Janotka et al. 2007; Kjellsen and Lagerblad 2007; Kurdowski W. 1980; Odler 2000; Telesca et al. 2014). The unique hydration properties and expansive behavior of the Type K shrinkage-compensating cement allow its total mesopore volume to increase substantially with aging, which leads to a reduced phenomenon in chloride penetration.

2.7 Conclusions

This study performed a systematic investigation of the transport properties of concrete mixtures containing shrinkage-compensating cement. For this purpose, a range of chloride penetration tests paired with fresh, strength, dimensional stability tests were performed on the mixtures with different dosages of Type K expansive agent. After comparing the results with those obtained for the mixtures that had no Type K expansive agent, the second series of tests were carried out to evaluate how SCMs can improve the resistance of shrinkage-compensating cement concretes against chloride penetration. From the investigations performed in this study, the following key conclusions were made:

1. The slump showed a noticeable drop in the mixtures that contained Type K expansive agent. The added SCMs, however, had different effects on the observed flow. While fly ash class F was able to fully mitigate the workability loss, fly ash class C had minimal effects on the flow. Silica fume, on the other hand, reduced

the flow, mainly because of fineness of silica fume in comparison with the other SCMs.

2. The expansive behavior of the shrinkage-compensating cement concrete was quantified for different dosages of Type K expansive agent. It was found that the peak expansion can be achieved after seven days (i.e., end of the curing period). For the mixtures tested in the current study, it was determined that the overall length change could remain in the expansion range even after 56 days. This confirms how an optimal dosage of Type K expansive agent can address the early-age shrinkage issues.
3. For 7.5% and 15% dosages of Type K expansive agent, an increase in the compressive strength was recorded in comparison with the control mixture that had no Type K expansive agent. While a high dosage of Type K expansive agent (e.g., 22.5%) resulted in significant expansion, this came with the drawback of the weakened bond between the coarse aggregates and the mortar, which adversely affected the 28-day compressive strength.
4. The resistance of concrete to the penetration of chloride ions reduced with increasing the dosage of replacement of portland cement with Type K expansive agent. While the addition of fly ash class F led to partial mitigation of increased chloride permeability, the incorporation of fly ash class C and silica fume were found to be superior solutions to address the vulnerability of shrinkage-compensating cement concretes to chloride attack.
5. Based on the results from water absorption and helium porosimetry tests, the pore volume of the concrete mixtures that contained 15% Type K expansive agent was

more than 50% higher than that of the control mixture. This was, however, reduced with the inclusion of SCMs, supporting the effectiveness of the identified mixture designs.

6. Upon the finding mechanisms of the recent research studies related to the porosimetry properties, it can be found that the more aluminate phase and the amount of sulfate phase presented in more of ettringite cause the increasing porosity, resulting in a reduced resistance in chloride penetration.
7. Partial replacement of portland cement with Type K expansive agent was found to lead to the development of shrinkage free, low permeability concrete mixtures if SCMs are included. This was confirmed in the concrete mixture that contained 15% Type K expansive agent and 7.5% silica fume after a holistic investigation of compressive strength, drying shrinkage, chloride penetration, and absorption characteristics of a wide range of mixtures.

2.8 Acknowledgements

The technical assistance of Dr. Fraciszek Hasiuk with performing the porosimetery tests is gratefully acknowledged.

2.9 References

Klein A, Karby T, Polivka M. Properties of an Expansive Cement for Chemical Prestressing. J Am Concrete Inst 1961; 58:59–82.

Mather B. Expansive Cements 1970.

Portland Cement Association. Types and Causes of Concrete Deterioration. PCA R&D Spec N 2617 2002:1–16.

ACI. Guide for the Use of Shrinkage-Compensating Concrete. 2010.

Chaunsali P, Mondal P. Cement and Concrete Research Physico-chemical interaction between mineral admixtures and OPC – calcium sulfoaluminate (CSA) cements and its influence on early-age expansion. Cement and Concrete Research 2016; 80:10–20.

Han J, Jia D, Yan P. Understanding the shrinkage compensating ability of type K expansive agent in concrete. Concrete and Building Materials 2016; 116:36–44.

Nair H, Ozyildirim C, Sprinkel MM. Evaluation of Bridge Deck with Shrinkage-Compensating Concrete. 2016.

Ramseyer C. Behavior of Shrinkage Compensating Concrete in an Unrestrained and Restrained Environment. 1–20.

Russell H, Stadler R, Gelhardt H. Shrinkage-Compensating Concrete Made With an Expansive Component. Concrete International 2002; 24:107–11.

Sprinkel M. Final Report Latex-Modified Concrete Overlay Containing Type K Cement 2015.

Péra J, Ambroise J. New applications of calcium sulfoaluminate cement. Cement and Concrete Research 2004; 34:671–6.

Ogawa K. C4A3S Hydration, Ettringite Formation, and Its Expansion Mechanism: II. Microstructural Observation of Expansion 1982; 12.

Rahman M, Chen Y, Lindquist W, Ibrahim A, Hindi R. Mitigation of Shrinkage Cracking in Bridge Decks Using Type-K Cement Mohammad 2018:133–44.

Gartner E. Industrially interesting approaches to “low-CO2” cements. Cement and Concrete Research 2004; 34:1489–98.

Odler I, Colán-Subauste J. Investigations on cement expansion associated with ettringite formation. Cement and Concrete Research 1999; 29:731–5.

Bentur A, Ish-Shalom M. Properties of type K expensive cement of pure components II. Proposed mechanism of ettringite formation and expansion in unrestrained paste of pure expansive component. Cement and Concrete Research 1974; 4:709–21.

Battaglia I. Experimental Use of Type K Cement Concrete in Wisconsin Highway Bridge Decks 2012.

AASHTO T277-15. Standard Method of Test for Electrical Indication of Concrete’s Ability to Resist Chloride Ion Penetration. Washington D.C: AASHTO; 2015.

D’Ambrosia MD. Report for the Illinois State Toll Highway. CTL Group Project No. 057122 2013; 1030.

Walkowich T. Field Monitoring of Shrinkage Cracking Potential in a High-Performance Concrete Field Monitoring of Shrinkage Cracking Potential in a High- Performance Concrete Bridge Deck. 2011.

Moffat. Shrinkage-Compensating Concrete: An Investigative Study. Structures Congress 2005:1–11.

Gress D. Determination of Shrinkage Characteristics of Concretes with Type K cement, Mineral and Chemical Additives. 2001.

Sprinkel MM. Latex-Modified Concrete Overlay Containing TYPE K Cement. FHWA/VTRC 05-R26. 2005.

D'Ambrosia MD, Slater J, Dam T Van. High-Performance Concrete for Bridge Decks Final Report. CTL Group Project No. 057122. vol. 1030. 2013.

Chaunsali P, Li S, Mondal P, Foutch D, Richardson D, Tung Y, et al. Bridge Decks: Mitigation of Cracking and Increased Durability 2013.

Ramey GE, Pittman DW, Webster G, Carden A. Use of Shrinkage Compensating Cement in Bridge Decks. 1997.

Carballosa P, Calvo JLG, Revuelta D, Sánchez JJ, Gutiérrez JP. Influence of cement and expansive additive types in the performance of self-stressing and self-compacting concretes for structural elements. Concrete and Building Materials 2015; 93:223–9.

Calvo JLG, Revuelta D, Carballosa P, Gutiérrez JP. Comparison between the performance of expansive SCC and expansive conventional concretes in different expansion and curing conditions. Concrete and Building Materials 2017; 136:277–85.

Sarkar S. Strength Enhancement in Type K Expansive Cement Using Additives. Journal of Materials in Civil Engineering 1990; 2:1–14.

Ramseyer C. Shrinkage Compensating Concrete – Past, Present, and Future, SP-307SP-307. 2016.

Foster-Goodman S, Vallens K. Shrinkage-Compensating Concrete Designs. Structrual Des 2018:40–3.

ASTM C33. Standard Specification for Concrete Aggregates. American Society Test Material 2013:1–11.

ASTM C192. Standard Practice for Making and Curing Concrete Test Specimens in the Laboratory. Management 2002; 04:1–8.

ASTM C143. Standard Test Method for Slump of Hydraulic-Cement Concrete. ASTM C143 2015:1–4.

ASTM C39. Standard Test Method for Compressive Strength of Cylindrical Concrete Specimens. American Society Test Material 2016:1–7.

FM 5-578. Florida Test Method for Concrete Resistivity as an Electrical Indicator of its Permeability 2004:4–7.

ASTM C157. StandardTest Method for Length Change of Hardened Hydraulic-Cement Mortar and. Annual B ASTM Stand 2016; 08:1–7.

ASTM C1202. Standard Test Method for Electrical Indication of Concrete's Ability to Resist Chloride Ion Penetration. American Society Test Material 2012:1–8.

NT BUILD 492. Concrete, Mortar and Cement-Based Repair Materials: Chloride Migration Coefficient from Non-Steady-State Migration Experiments. Measurement 1999:1–8.

ASTM C642. Standard Test Method for Density, Absorption, and Voids in Hardened Concrete. United States American Society Test Material 2008:11–3.

Giesche H. Mercury porosimetry: A general (practical) overview. Part Part Syst Charact 2006;23:9–19.

Winnefeld F, Lothenbach B. Hydration of calcium sulfoaluminate cements - Experimental findings and thermodynamic modelling. Cem Concr Res 2010;40:1239–47.

Grusczscinski E, Brown PW, Bothe J V. The formation of ettringite at elevated temperature. Cem Concr Res 1993;23:981–7. doi:10.1016/0008-8846(93)90052-B.

Kaufmann J, Lothenbach B, Winnefeld F. Stability of ettringite in CSA cement at elevated temperatures 2016;28.

Mehta PK. Studies on slump loss in expansive cement concretes. Klein Symp Expans Cem Concr SP - 38 1973:57–68.

Rashad AM, Seleem HEDH, Shaheen AF. Effect of Silica Fume and Slag on Compressive Strength and Abrasion Resistance of HVFA Concrete. Int J Concr Struct Mater 2014;8:69–81.

Kurtis KE. Analysis of Durability of Advanced Cementitious Materials for Rigid Pavement Construction in California 1999.

Ghafoori N, Spitek R, Najimi M. Transport properties of limestone-containing self-consolidating concrete. ACI Mater J 2017;114:527–36.

Krus M, Hansen KK, Kunzel HM. Porosity and liquid absorption of cement paste 1997;30:394–8.

Hearn N, Hooton RD, Nokken MR. Pore structure, permeability, and penetration resistance characteristics of concrete. ASTM Spec Tech Publ 2006:238–52.

Bamforth PB. The relationship between permeability coefficients for concrete obtained using liquid and gas. Mag Concr Res 1987;39:3–11.

Journal IC, Karnataka T, Bombay T. A comparative study for determining pore volume of concrete A comparative study for determining pore volume of concrete 2010;4.

Garboczi EJ. Permeability, Diffusivity, and Microstructural Parameters: a Critical Review. Cem Concr Res 1990;20:591–601.

Le Saoût G, Lothenbach B, Hori A, Higuchi T, Winnefeld F. Hydration of Portland cement with additions of calcium sulfoaluminates. Cem Concr Res 2013;43:81–94.

Scrivener KL. Backscattered electron imaging of cementitious microstructures : understanding and quantification 2004;26:935–45.

Kjellsen KO, Lagerblad B. Microstructure of tricalcium silicate and Portland cement systems at middle periods of hydration-development of Hadley grains. Cem Concr Res 2007;37:13–20.

Janotka I, Krajči L, Mojumdar SC. Performance of sulphoaluminate-belite cement with high C4A3S̄ content. Ceram - Silikaty 2007;51:74–81.

Telesca A, Marroccoli M, Pace ML, Tomasulo M, Valenti GL, Monteiro PJM. A hydration study of various calcium sulfoaluminate cements. Cem Concr Compos 2014;53:224–32.

Odler I. Special Inorganic Cements. 2000.

Glasser FP, Zhang L. High-performance cement matrices based on calcium sulfoaluminate-belite compositions. Cem Concr Res 2001;31:1881–6.

Kurdowski W. Expansive cements. Proc 7th Int Congr Chem Cem 1980;I:V-2/1–10.

Table 2.2 Chemical composition of binders (w/t%).

Type of Binder	CaO	SiO_2	SO_3	Fe_2O_3	Al_2O_3	MgO	K_2O	Na_2O	TiO_2	Ye'elimite	Gypsum
Porland Cement	62.94	20.10	3.18	3.09	4.44	2.88	0.61	0.10	0.24	–	19.4
Shrinkage-Compensating Cement	65.40	1.80	25.10	1.20	4.80	1.40	0.10	–	–	1.4	14.7
Fly Ash C	15.78	50.87	0.61	5.27	20.17	3.19	1.09	0.69	1.29	–	–
Fly Ash F	21.54	42.46	1.20	5.51	19.46	4.67	0.68	1.42	1.48	–	–
Silica Fume	0.30	94.30	–	0.10	0.09	0.43	0.83	0.27	–	–	–

Table 2.3 Aggregate properties.

Aggregate Type	Bulk Specific Gravity	SSD Specific Gravity	Absorption (%)	Dry Rodded Unit Weight (kg/m^3)	Fineness Modulus
Fine aggregates	2.77	2.79	0.90	-	3.0
Coarse aggregates	2.76	2.77	0.40	1653	-

Table 2.4 Mixture proportions.

Mix. ID	PC	KC	SF	FA-F	FA-C	Water	Fine Agg.	Coarse Agg.	Type K Dosage	w/c
	kg/m^3								(%)	(%)
Control	404.5	0.0	0.0	0.0	0.0	202.0	565.5	1090.0	0.0	0.5
KL	374.0	30.0	0.0	0.0	0.0	202.0	565.5	1090.0	7.5	0.5
KM	344.0	61.0	0.0	0.0	0.0	202.0	565.5	1090.0	15.0	0.5
KH	313.5	91.0	0.0	0.0	0.0	202.0	565.5	1090.0	22.5	0.5
KM+FAF	283.0	61.0	0.0	61.0	0.0	202.0	565.5	1090.0	15.0	0.5
KM+FAC	283.0	61.0	0.0	0.0	61.0	202.0	565.5	1090.0	15.0	0.5
KM+SF	315.5	61.0	28.5	0.0	0.0	202.0	565.5	1090.0	15.0	0.5

Table 2.5 Test results for slump flow and 28-day compressive strength.

	Mixture ID					
Properties	**Control**	**KL**	**KM**	**KM-FAF**	**KM-FAC**	**KM+SF**
Absorption after immersion, %	5.53	5.73	7.04	6.98	6.25	6.41
Absorption after immersion and boiling, %	5.61	5.72	7.66	7.42	6.37	6.94
Volume of permeable void, %	12.93	13.17	19.32	16.36	14.44	15.51

Table 2.6 Absorption test results for the mixtures considered in the current study.

Properties	Mix. ID					
	Control	**KL**	**KM**	**KM-FAF**	**KM-FAC**	**KM-SF**
Absorption after immersion (%)	5.53	5.73	7.04	6.98	6.25	6.41
Absorption after immersion and boiling (%)	5.61	5.72	7.66	7.42	6.37	6.94
Volume of permeable void (%)	12.93	13.17	19.32	16.36	14.44	15.51

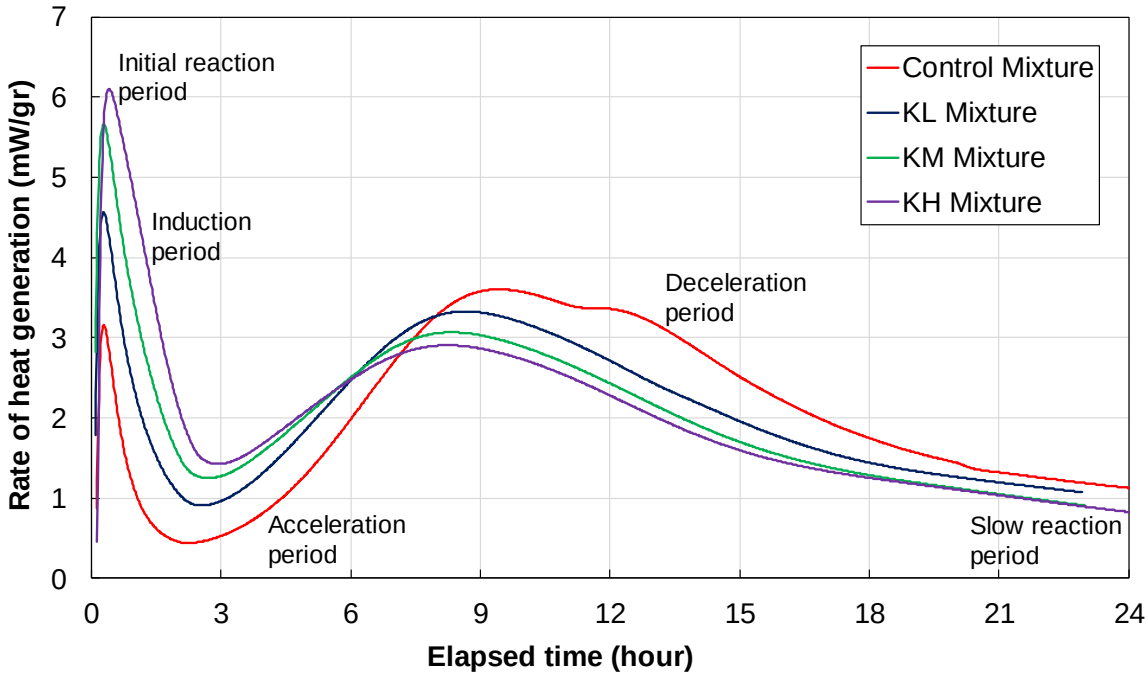

Figure 2.1. Effects of Type K expansive agent on the rate of heat generation.

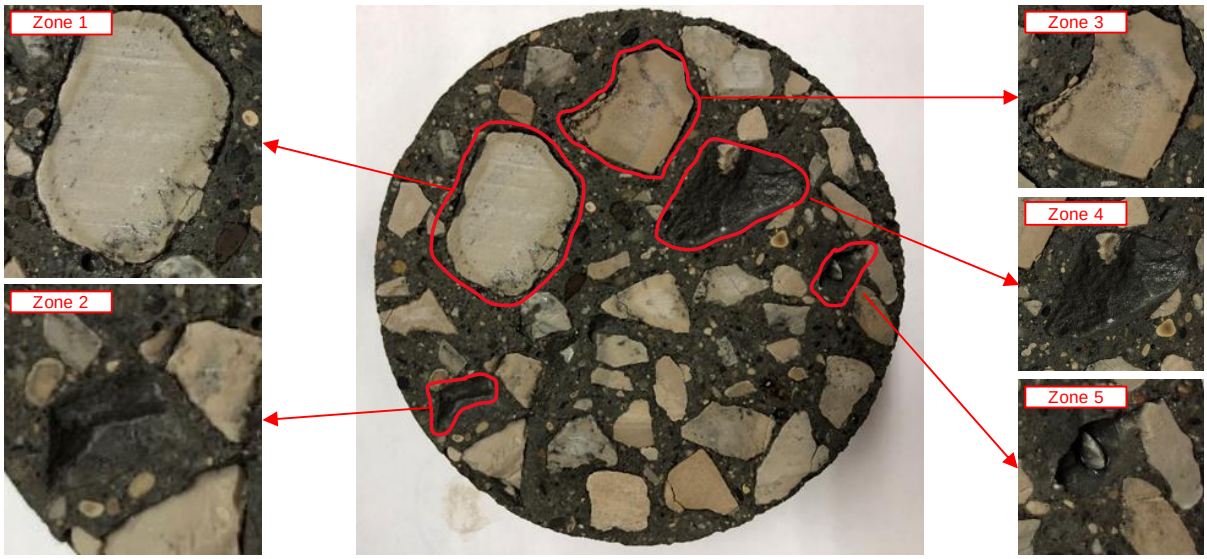

Figure 2.2. Zoomed-in view of one of the specimens made with KH mixture: Zone 1, weak interface; Zone 2, loose aggregate; Zone 3, weak interface; Zones 4 and 5, loose aggregates.

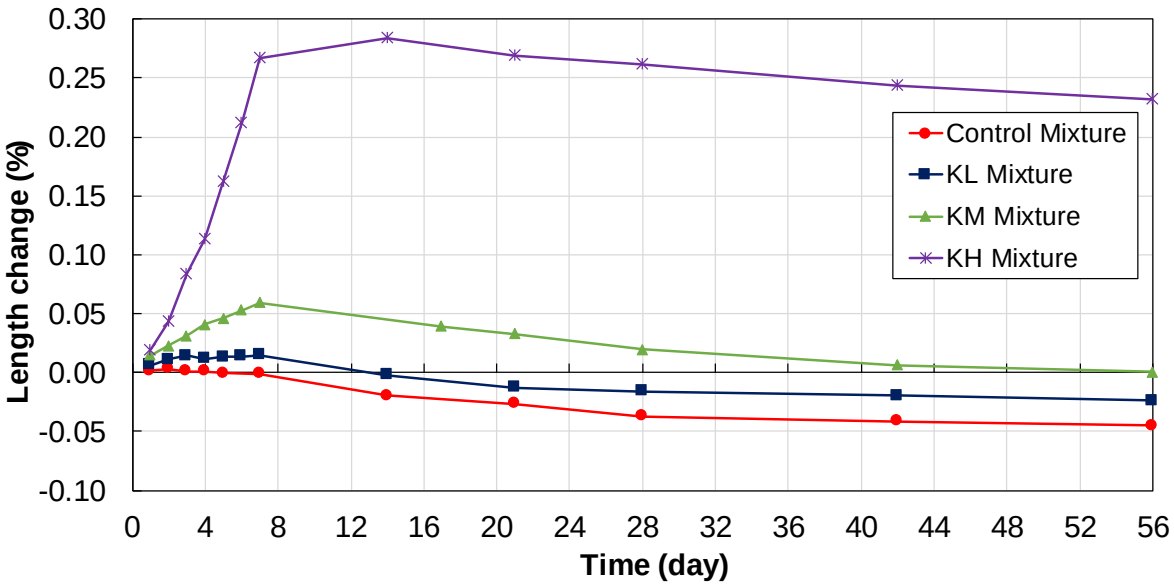

(a)

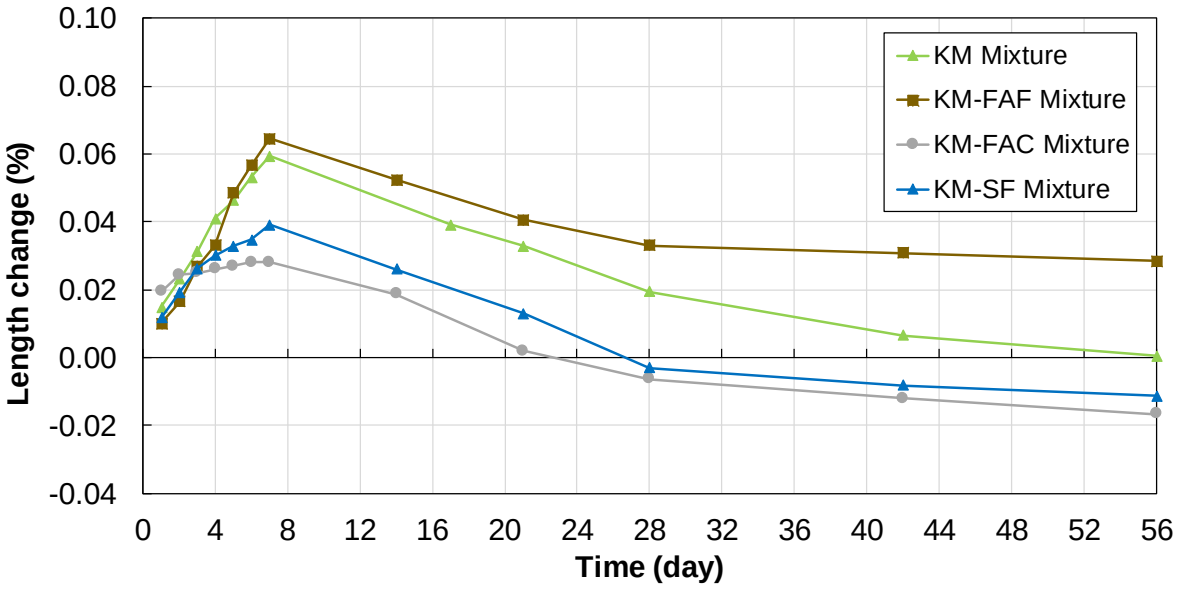

(b)

Figure 2.3. Length change measurements over time for the mixtures: (a) with and without Type K expansive agent and (b) with and without SCMs.

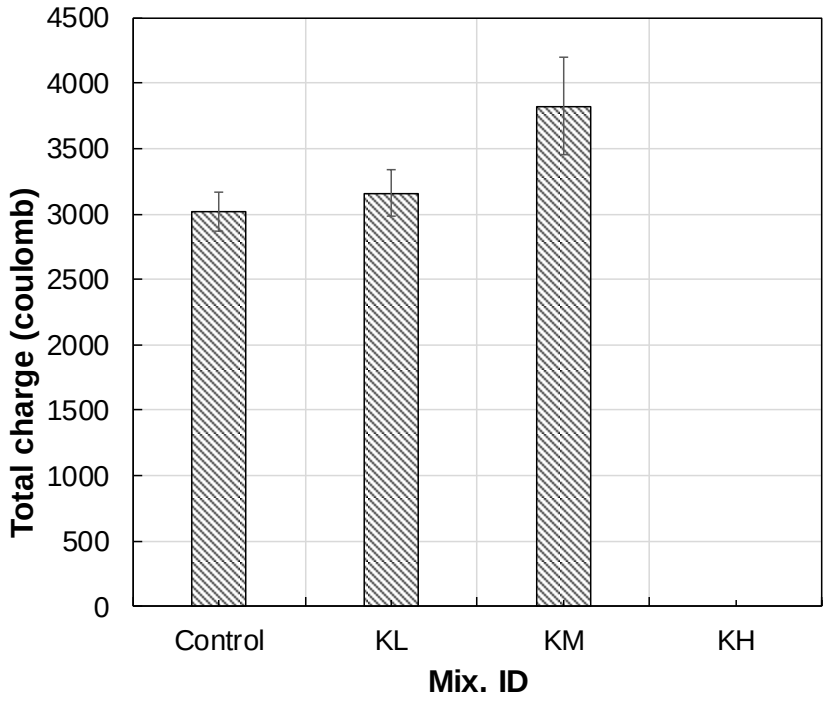

(a)

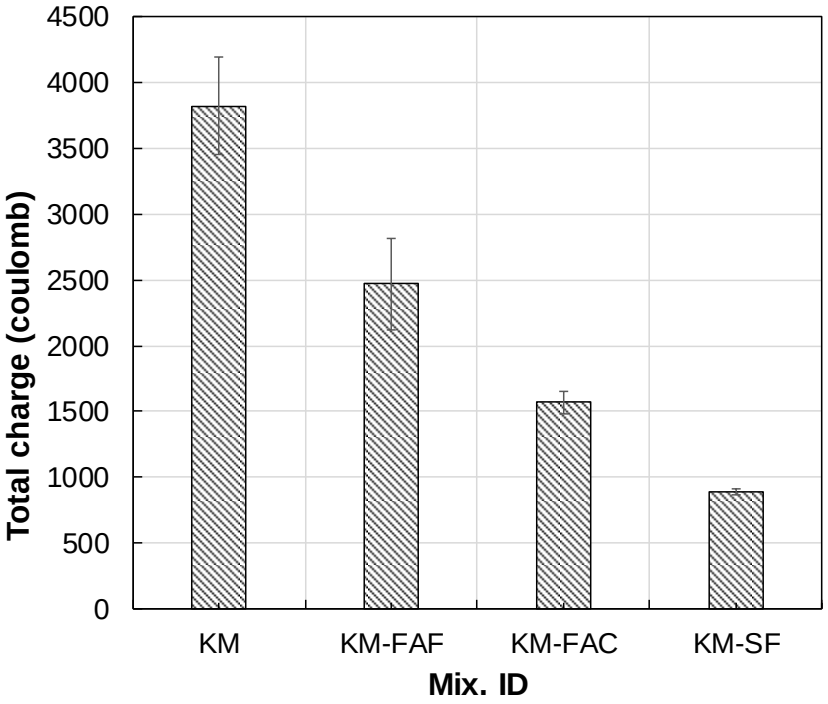

(b)

Figure 2.4. Total charge passed through disk specimens for the mixtures: (a) with and without Type K expansive agent and (b) with and without SCMs.

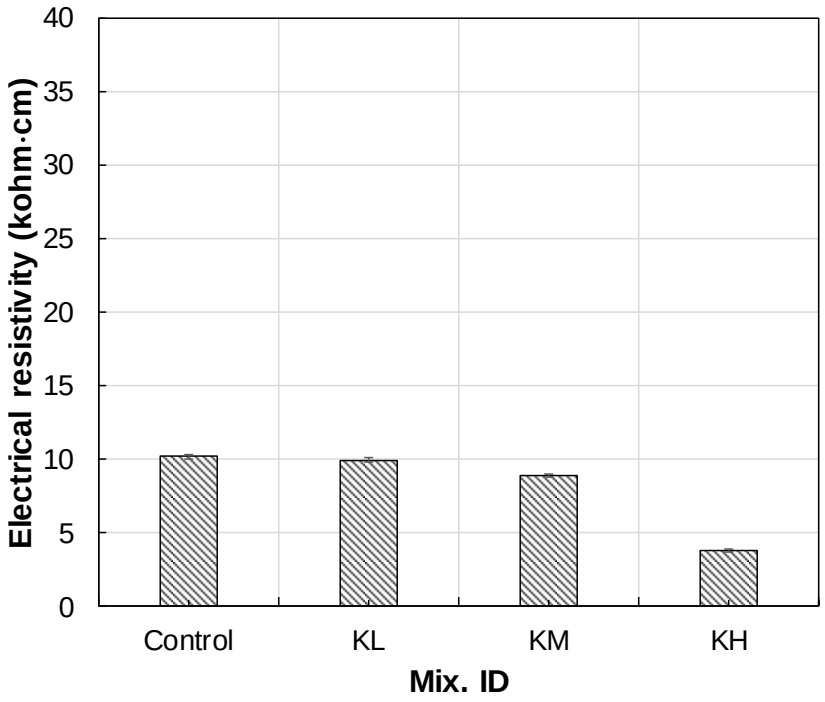

(a)

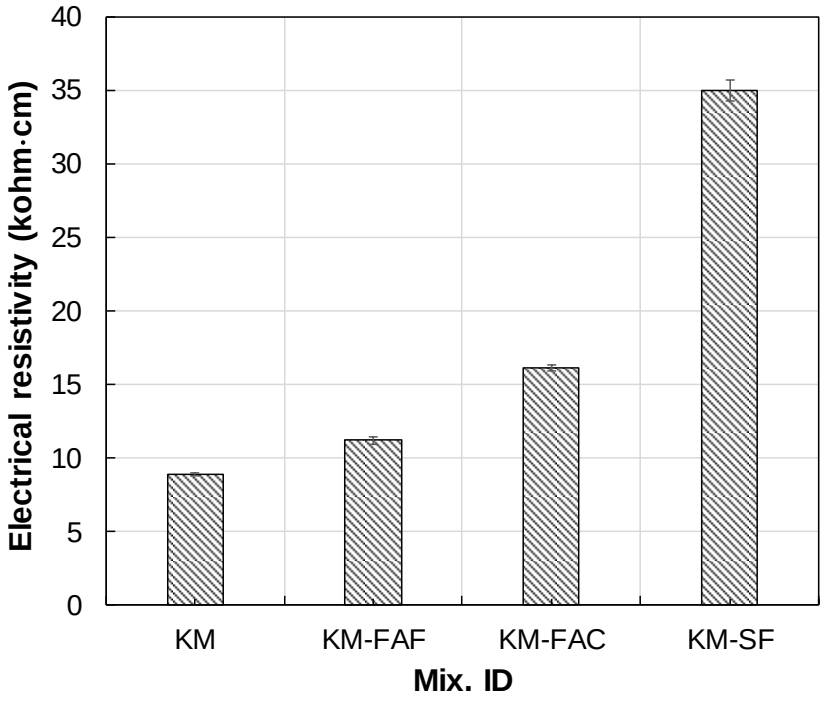

(b)

Figure 2.5. Measurements for electrical resistivity: (a) with and without Type K expansive agent and (b) with and without SCMs.

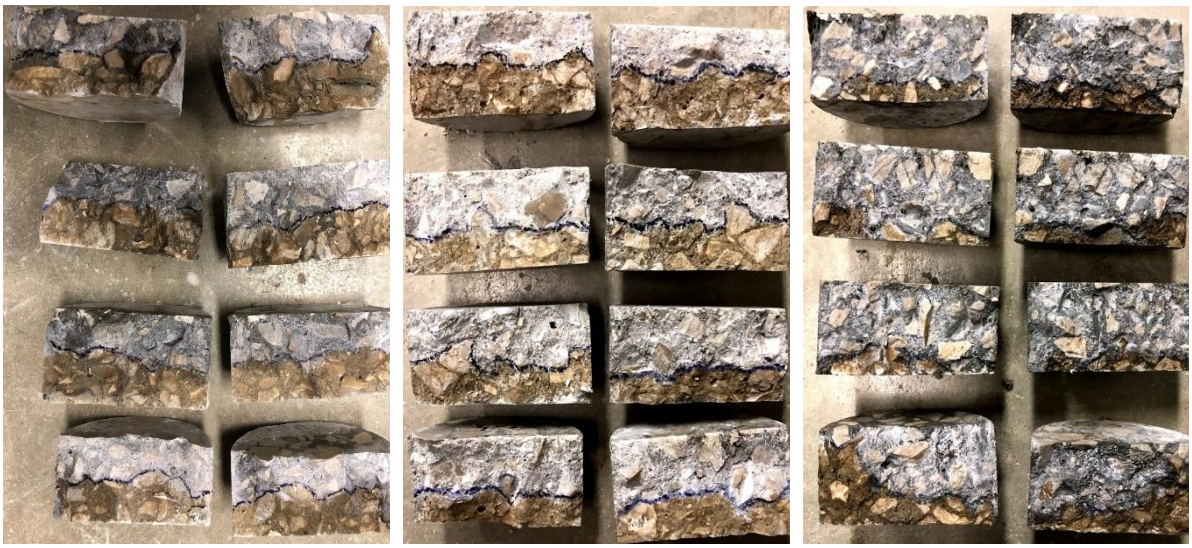

Control Mixture KL Mixture KM Mixture

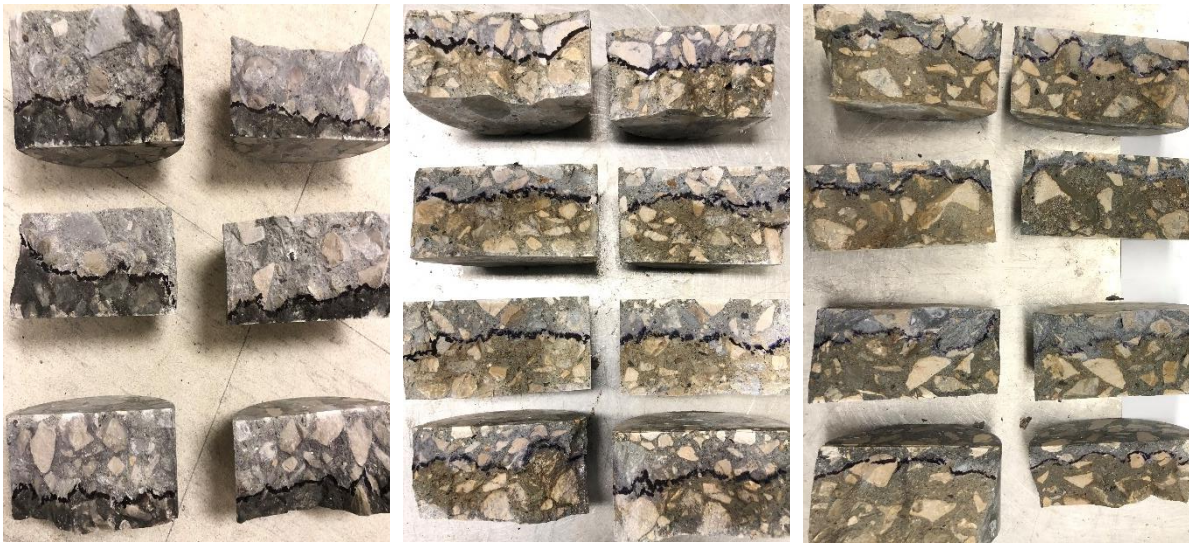

KM-FAF Mixture KM-FAC Mixture KM-SF Mixture

Figure 2.6. Chloride ion penetration depth measured for the mixtures investigated in the current study.

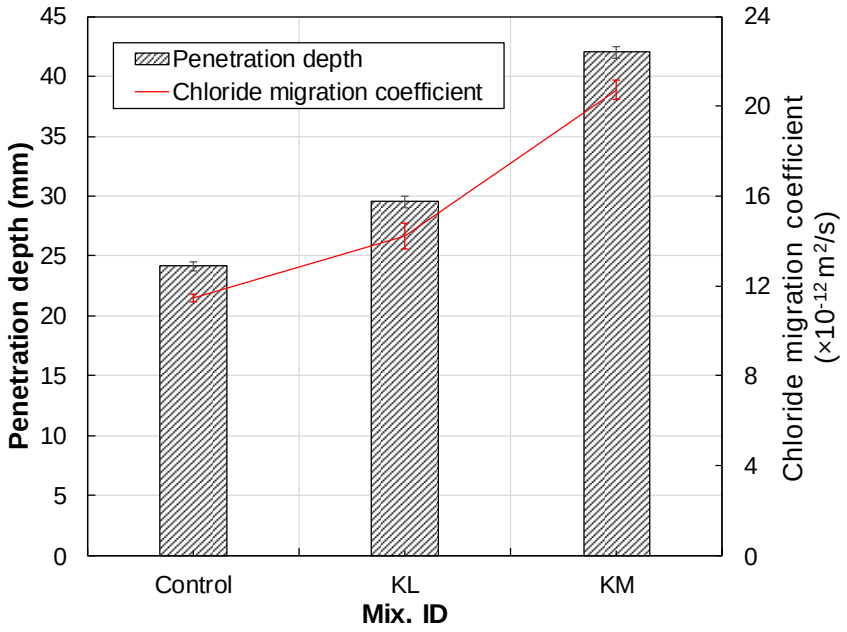

(a)

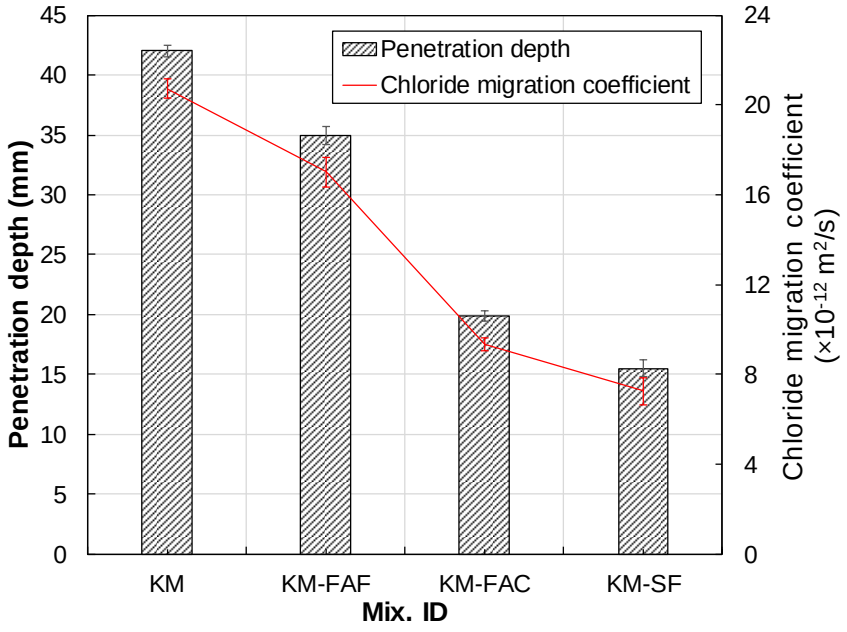

(b)

Figure 2.7. Results of rapid chloride migration tests: (a) with and without Type K expansive agent and (b) with and without SCMs.

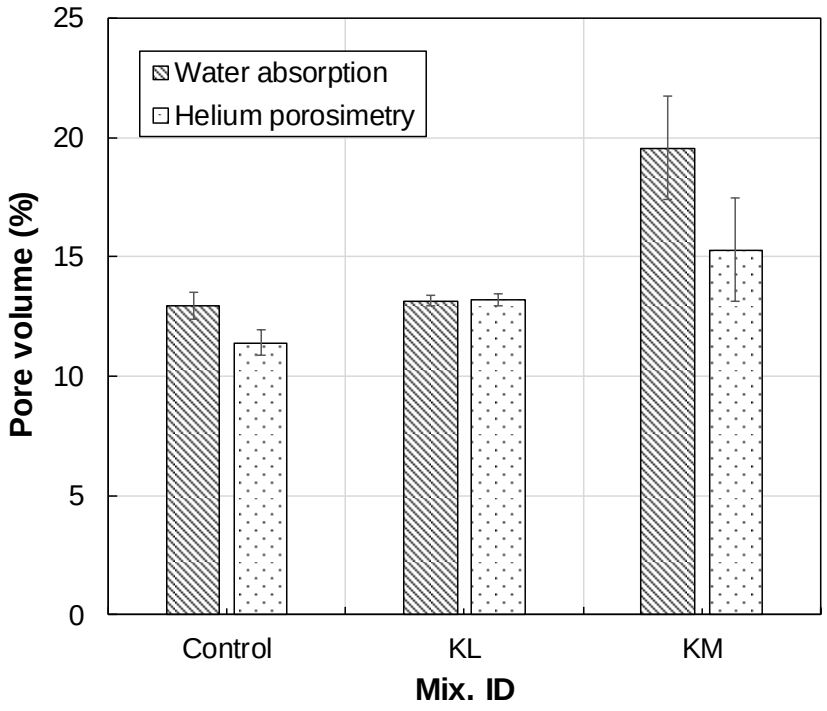

(a)

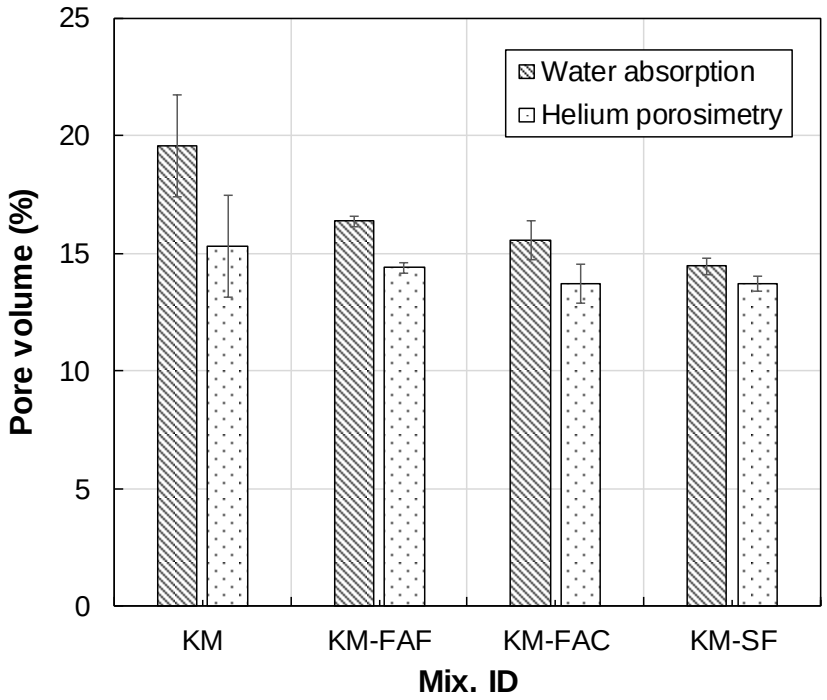

(b)

Figure 2.8. Results of water absorption and helium porosimetry results: (a) with and without Type K expansive agent and (b) with and without SCMs.

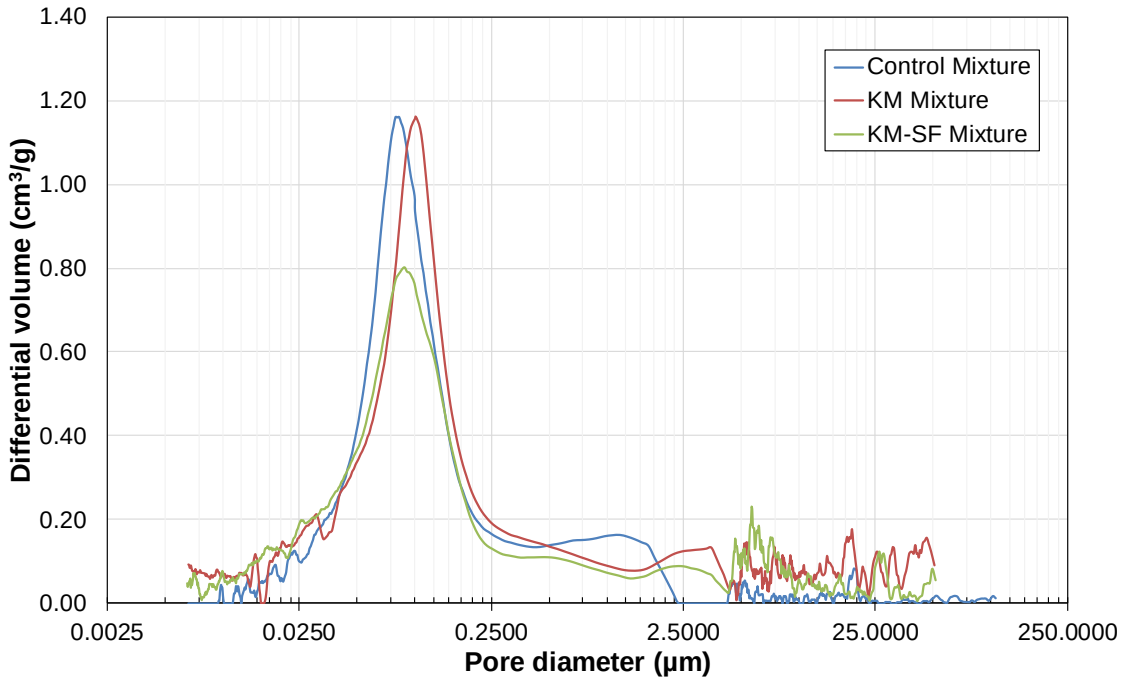

Figure 2.9. MIP test results: (a) differential porosity incremental intrusion volume of mercury versus pore diameter of specimen and (b) total intrusion volume of mercury.

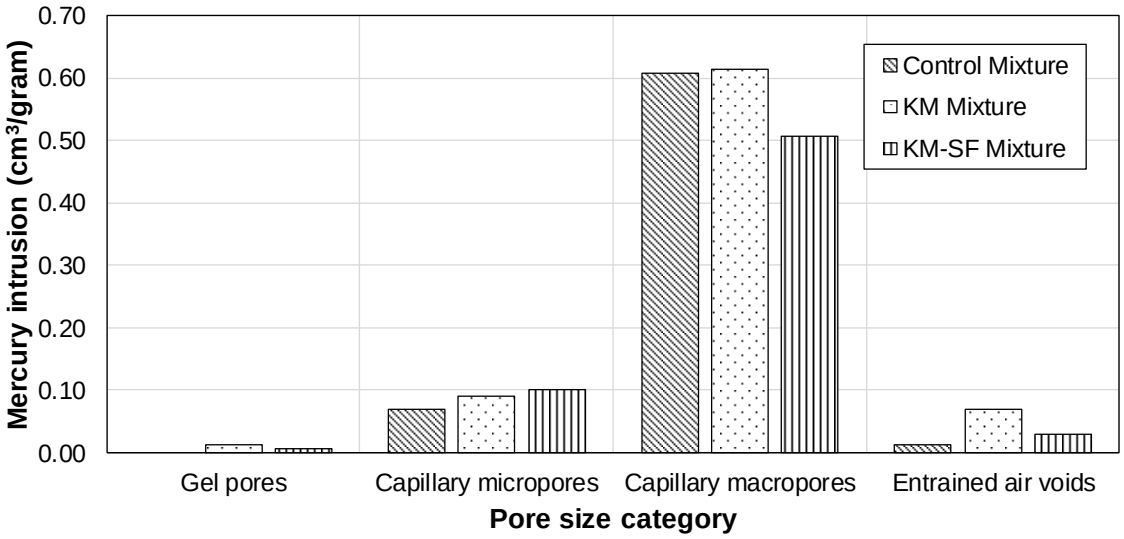

Figure 2.10. Intrusion volume of mercury at different pore size range for concrete samples.

CHAPTER 3. REINFORCEMENT CORROSION AND TRANSPORT PROPERTIES OF CHLORIDE IONS, WATER, AND OXYGEN IN SHRINKAGE-COMPENSATING CEMENT CONCRETES

3.1 Abstract

One of the primary concerns for those involved in the construction industry and maintenance of concrete structures is the time-dependent volume reductions/shrinkage resulted from the moisture loss. This will create tensile stresses in the concrete, which can eventually cause the cracking and debonding of between steel reinforcement and concrete. Among possible solutions, shrinkage-compensating cement (a.k.a., Type K expansive agent) has been reported to mitigate autogenous and drying shrinkage, leading to enhanced volumetric stability for concrete. However, the results of accelerated transport property experiments have shown that this improvement may come with the expense of increased permeability of concrete. This raised a serious question about long term durability of Type K cement contained concrete, particularly whether the unfavorable transport property potentially lead to premature deterioration resulted from corrosion of steel or not? To understand the performance of steel reinforcement embedded with this type of concrete under aggressive environmental conditions, more traditional tests rather than the commonly used accelerated test methods are necessary. In this study, therefore, a comprehensive experimental program, including the long-term monitoring corrosion rate of steel embedded in concrete, chloride diffusion, as well as air permeability and capillary absorption (sorptivity), were implemented to evaluate the ability of resisting penetration of corrosive agents (air, water and chloride) and chloride induced corrosion for shrinkage-compensating cement concrete with various dosages. The results revealed that the corrosion rate, chloride diffusion, capillary absorption, and gas permeability were adversely affected by the use of Type K expansive agent, which is in agreement with the

previous discussion. In particular, the corrosion rate of concrete made with optimum manufactory dosage of Type K expansion agent (15.0%) was considerably high, and the half-cell potential results for this concrete were in high corrosion potential zone. The satisfactory performance of such durability parameters was addressed by the identification of optimal dosages of supplementary cementitious materials, i.e., fly ash (Class C and F) and silica fume. The outcome of this study is proposed to provide recommendations in utilizing Type K cement in the highway bridge and building infrastructure applications, especially where the structural components are susceptible to both shrinkage and chloride-induced corrosion.

Keyword: Shrinkage-Compensating Cement; Type K Expansive Agent; Chloride Diffusion; Corrosion Rate; Air Permeability; Capillary Absorption; Supplementary Cementitious Materials.

3.2 Introduction

Concrete structures are often vulnerable to the time-dependent volume instability and cracking resulted from the combination of shrinkages, i.e., drying shrinkage, autogenous shrinkage, and plastic shrinkage. These cracks, particularly in bridge decks or joints, are often the source of penetration of aggressive agents, such as chloride ions, which significantly affect the long-term performance of structures. Shrinkage-compensating cement (a.k.a., Type K expansive agent) has been reported to effectively mitigate autogenous and drying shrinkage, leading to eliminate the shrinkage cracking (ACI 2010; Chaunsali and Mondal 2016; Han et al. 2016; Klein et al. 1961; Mather 1970; Nair et al. 2016; Portland Cement Association 2002). The main components of shrinkage-compensating cement are tetracalcium trialuminate sulfate ($4CaO{\cdot}3Al_2O_3{\cdot}SO_3$, abbreviated as $C_4A_3\bar{S}$), anhydrite ($CaSO_4$), and lime (CaO). The needle crystals formed in the early stage, ettringite ($C_3A\bar{S}_3H_{31}$), can explain the expansive in such

type of cement according to the following reaction, which is, in turn, able to minimize or eliminate the early-age shrinkage cracking (Ogawa 1982):

$$C_4A_3\bar{S} + 6CH + 8C\bar{S}H_2 + 71H \rightarrow 3C_6A\bar{S}_3H_{31}$$

where CH represents the calcium hydroxide, H is the water, and $C\bar{S}H_2$ is the gypsum.

Based on a review of the existing literature, there are a few studies performed to understand the essential characteristics, such as mechanical properties, time-dependent shrinkage, and hydration process, of the concretes made with shrinkage-compensating cement. Among them, Mather (Mather 1970) reported that the addition of a proper dosage of Type K expansive agent reduces the drying shrinkage without affecting the mechanical properties in any significant way. The cited study, however, indicated that the workability of the concrete mixtures that include this type of cement could drop faster than that of the mixtures made only with portland cement. Similar observations were provided by Han et al. (2016) as well. In the experimental study conducted by Péra and Ambroise (2004), a promising development of strength over time, including an appropriate early strength, was obtained in the mixtures that contained shrinkage-compensating cement. The volume stability of shrinkage-compensating cement concretes was investigated by Ramseyer et al. (Ramseyer 2016) for in-situ applications. With testing a wall segment and two slabs, the restrained behavior of shrinkage-compensating cement concretes was evaluated under unrestrained, partially restrained, and fully restrained conditions. In a separate study conducted by Rahman et al. (Rahman et al. 2018) on the shrinkage-induced cracking of bridge decks, it was determined that the compressive stresses generated due to the early-age expansion of shrinkage-compensating cement could counteract the tensile stresses that originate from drying shrinkage. This was found to address the issue

of early-age cracks. Despite the contribution of past investigations, very limited studies were found in the literature regarding the long-term durability of shrinkage-compensating cement concretes. This was the primary motivation of the current study to (i) explore the corrosion and transport properties of this type of concrete and (ii) develop appropriate solutions to enhance it against corrosion and chloride penetration.

Prior to performing corrosion tests, the transport properties of shrinkage-compensating cement concretes were assessed by the authors of this manuscript through accelerated tests on the mixtures that had various dosages of Type K expansive agent. The outcome indicated that the permeability of the mixtures is adversely affected by the use of this type of cement. Specifically, the resistance of the developed mixtures to the penetration of chloride ions was measured through rapid chloride penetration test (RCPT), rapid chloride migration test (RMT), and surface resistivity test. The recorded results confirmed that the resistance of the mixtures to chloride ion penetration drops with increasing the replacement dosage of portland cement with Type K expansive agent. In addition, based on the results of water absorption tests, the pore volume of the concrete mixtures that contained Type K expansive agent was found considerably higher than that of the control mixture made without Type K expansive agent. Such observations were consistent with a few other studies: Battaglia (2012) investigated the permeability of shrinkage-compensating cement concrete mixtures by performing RCPT and indicated that the mixtures made with Type K expansive agent had a chloride permeability close to twice of those made with Type I cement. In two separate studies, D'Ambrosia and Slater (2013) and Nair et al. (2016) also highlighted the concerns related to high permeability and risk of corrosion associated with the use of Type K expansive agent. The reported observations, however, were primarily from the accelerated tests that are known to have several

limitations. Thus, there were still fundamental questions on how the use of Type K expansive agent influence the penetration of aggressive agents and corrosion of embedded steel bars over time.

To address the identified research gaps, the long-term performance of concrete mixtures made with various dosages of Type K expansive agent (i.e., 0, 7.5, and 15% by weight of total cementitious materials) was investigated in the current study. This was with a focus on monitoring the progress of corrosion of embedded steel bars for a period of more than one year. As the chloride-induced corrosion of steel reinforcement is directly dependent on the penetration and availability of chloride ions, water, and oxygen in the concrete matrix, a set of air permeability, chloride diffusion, and capillary absorption (sorptivity) tests were also performed to provide a detailed insight on the transport properties of the tested mixtures. In the second stage of the testing program, similar experiments were carried out on the mixtures that were improved with the addition of supplementary cementitious materials (SCMs), such as fly ash Class C, fly ash Class F, and silica fume. The choice of adding SCMs was made due to their outstanding pozzolanic reaction, in which calcium hydroxide ($Ca(OH)_2$) is consumed to produce additional C-S-H reaction products. This fills up the pores, and consequently, results in the reduced permeability of the binder (Najimi and Ghafoori 2019; Schneider et al. 2011). The mercury intrusion porosimetry analyses were, then, conducted to further support the findings based on the pore structure of the hardened mixtures. The outcome of this study is expected to provide improved mixture designs with shrinkage-compensating cement, especially for the RC structures vulnerable to both early-age shrinkage and chloride-induced corrosion.

3.3 Experimental Testing Program

To investigate the penetration of destructive agents (chloride, water and oxygen) into the concrete, and the corrosion for embedded reinforcing steel, two series of experiments were considered in the current study. In the first series, the authors investigated the performance of shrinkage-compensating cement concrete mixtures with different dosages of Type K expansive agent. Upon understanding the adverse effects of replacing portland cement with shrinkage-compensating cement on the corrosion of reinforcement and transport properties of concrete, the second series of experiments were planned with primary focus on the impact of the SCMs incorporation in improving performance of Type K cement concrete exposed to the abovementioned aggressive agents.

3.3.1 Materials

The cement used in this study included Type I portland cement and shrinkage-compensating cement. For the second series of mixtures, three SCMs, including fly ash Class C, fly ash Class F, and silica fume, were used. Table 3.1 summarizes the chemical composition of the cements and SCMs. The aggregates were comprised of fine aggregates (0 to 4.75 mm) and coarse aggregates (4.75 to 25 mm), in accordance with the gradation size requirements of ASTM C33 (ASTM C33 2013). Table 3.2 presents the physical properties of the fine and coarse aggregates. With the goal of maintaining the workability within a range of 14 ± 4 cm, a high-range water-reducing (HRWR) admixture was used only for the mixtures that contained silica fume.

3.3.2 Mixture Proportions

Table 3.3 presents the mixture proportions of the concretes tested in the current study. Four dosages of Type K expansive agent, i.e., 0, 7.5, 15, and 22.5%, were selected to replace

Type I portland cement in the first series of tests. To reflect no, low, medium, and high dosage of replacement, these mixtures have been labeled in Table 3.3 as Control, KL, KM, and KH, respectively. It should be noted that the high dosage mixture provided a very low concrete strength (in the range of 4.5 MPa), due to excessive expansion (of more than 0.22% after 56 days). Thus, the second series of mixtures were developed on the basis of the KM mixture with the addition of a source of SCM, i.e., 15% fly ash Class C, 15% fly ash Class F, and 7.5% silica fume. As reflected in Table 3.3, these three mixtures have been labeled as KM+FAF, KM+FAC, and KM+SF, respectively. The water-to-cementitious materials ratio (w/c) for all the mixtures designed for this investigation was selected as 0.5.

3.2.3 Mixing, Sampling, and Testing

Concrete specimens were mixed by a drum mixer with a capacity of 0.1 m^3 following the mixing procedure provided in ASTM C192 (ASTM C192 2002). The mechanical properties, such as strength and dimensional stability, were measured on 10×20 cm cylindrical and 10×10×56 cm prismatic samples prepared and tested based on ASTM C39 (ASTM C39 2018) and ASTM C157 (ASTM C157 2017). A set of cylindrical samples were also cast for the measurement of the permeability of destructive agents, such as chloride ions, water, and oxygen. After consolidating by a vibrating table, the samples were covered and maintained at the room temperature for the first 24 hours. They were then removed from their molds and stored in a standard moist room at a temperature of 23 ± 2 ºC until the testing time.

For evaluating the long-term corrosion of steel bars, four samples were cast for each mixture with two layers of No. 13 bars (with the diameter of 12 mm), including one bar at the top layer and two bars side-by-side at the bottom layer, according to ASTM G109 (ASTM 2013). In this test, a 10-ohm resistor was connected between the top and bottom layers of steel

reinforcement. To eliminate any leaking issue, a pool of 15.2×7.6×7.6 cm salt solution was created at the top of each sample, as shown in Figure 3.1. After 28 days of curing, the samples were removed from the moist room and placed in the laboratory under room temperature with a 50% relative humidity. Except for the bottom surface of the inside pool, all the sides of each sample were coated with water-proof epoxy. The samples were then exposed to a solution of 30 g/L NaCl (3%) in alternating cycles of 2-week wetting and 2-week drying. Throughout the test, the current, voltage, and half-cell potential were monitored on a regular basis to assess the progress of corrosion. This test continued for more than one year, including 28 weeks of wetting and 28 weeks of drying.

The air permeability was measured to investigate the ability of the developed concrete mixtures to resist the passage of air. The test was established following the University of Cape Town Method (Alexander 2005). For this purpose, 50 mm disc samples were cut from the cylindrical concrete specimens (Figure 3.2). The disc samples were then sealed with rubber collars and placed on the top of the permeability device. After the air was pumped into the cell with a 170 kPa pressure, the pressure decay was monitored for 24 hours. The Darcy coefficient of permeability was then determined to evaluate the air permeability of the shrinkage-compensating concrete mixtures. Capillary absorption (sorptivity) test was also conducted in accordance with ASTM C1585 (ASTM C1585 2004). In this test, after 18 days of preconditioning, which included placing the samples in a 50 ℃ and 80% relative humidity environment for 3 days and in a 23 ℃ and 50% relative humidity environment for 15 days, the bottom surface of each disc specimen was exposed to water. The mass increase resulting from the absorption of water as a function of time was recorded for eight days.

Chloride diffusion test was performed according to ASTM C1556 (ASTM Committee C09.66 2011). This was to determine the resistance of the concrete specimens that contained different dosages of Type K cement and SCMs against chloride diffusion. A set of 75 mm disc samples sealed on all the sides except the top surface immersed in 16.5% NaCl solution (165 g NaCl in 1 L solution) for 45 days. The powder samples were then obtained by grinding off eight layers from each sample in accordance with ASTM C1556 (ASTM Committee C09.66 2011). The powders were mixed/stirred with nitric acid and water for the chloride concentration analysis. In addition, detailed information regarding porosity, pore size distribution, and pore volume was obtained via mercury intrusion porosimetry (MIP) (Diamond 2000). For this purpose, mercury was injected into the Control, KM, and KM+SF samples with an increasing pressure. Each sample was oven-dried for 12 hours at 100 °C and stored in a desiccator at room temperature for 24 hours before the test was performed. This provided an in-depth insight to further explain and support the experimental test results.

3.4 Shrinkage-Compensating Behavior and Compressive Strength

Prior to the main testing program planned for the current study, the shrinkage-compensating behavior and compressive strength of the designed mixtures were investigated to ensure that they meet the expected performance requirements. The shrinkage-compensating behavior was evaluated for different dosages of Type K expansive agent, as shown in Table 3.4. The length change measurement was performed from the 1st day after demolding up to the 56th day, during which the samples were in the curing room for the first seven days. The obtained results indicate that the control mixture experienced a drying shrinkage of 0.045% after eight weeks, while the mixtures that contained Type K expansive agent were in expansion after seven days (i.e., end of the curing period). The overall length change of the KL and KM

mixtures was an expansion of 0.020% and 0.060% after seven days and -0.023% and 0.001% after 56 days, respectively. This showed that the KM mixture delivers an early age expansion to a level that destructive tensile stresses due to drying shrinkage are entirely eliminated. A similar early age expansion was observed in the mixtures that contained 15% Type K expansive agent with SCMs, indicating that the selected SCMs had no adverse effect on the shrinkage-compensating behavior of the second series of the mixtures. For the KH mixture, however, a significantly high expansion was observed. This led to the weakening of the bond between the coarse aggregates and their adjacent mortar.

In addition, compressive strength was evaluated to understand the effects of Type K expansive agent on the mechanical properties of the developed mixtures. Table 3.4 summarizes average compressive strength results. It was found that the compressive strength increases with the use of 7.5% and 15% dosages of Type K expansive agent. However, a further increase of dosage to 22.5% reduces the concrete strength to a level that almost no compressive force can be resisted. This was consistent with the loss of internal bond observed in the KH mixture specimens. When the SCMs were included in the concrete mixtures made with 15% Type K expansive agent, the compressive strength was not influenced in any significant way and the results remained in the range of 44.9 MPa to 57.6 MPa.

3.5 Long-Term Corrosion of Embedded Reinforcement

Four samples were cast for each mixture and subjected to salt ponding for a period of one year (Figure 3.3). Every two weeks, at the time of switching between the cycles of wetting and drying, the half-cell potential was measured between the top layer steel reinforcement and a silver/silver-chloride (Ag/AgCl) reference electrode filled with potassium chloride (KCl) solution. A multimeter with the resolution of 0.1 µA and 0.1 mV was also utilized to measure

the current and voltage between the top and bottom layers of steel reinforcement. Figure 4 presents the half-cell potential measurements converted to copper/copper sulphate (Cu/CuSO4) electrode (CSEs) (Park 2009). To determine the risk of steel corrosion, an intermediate level risk was associated with a corrosion potential between -350 mV and -200 mV, while a high-level risk was associated with a corrosion potential more negative than -350 mV, following ASTM C876 (ASTM C876 2016; Clear 1976; Stratfull 1973). According to Figure 3.4, the half-cell potential was found to remain relatively constant and as low as -200 mV for the mixtures containing no and 7.5% Type K expansive agent. However, the reference potential for steel reinforcement embedded in the KM mixture started to rise at the 196th day (i.e., after 28 weeks) and reached close to -350 mV at the end of the 336th day (i.e., 48 weeks), indicating a high risk of corrosion in the top layer of steel reinforcement. On the other hand, when the SCMs were incorporated in the KM mixture, the steel embedded in the mixtures showed a low risk of corrosion. This highlighted how the adverse effects of Type K expansive agent can be mitigated with high pozzolanic activities introduced by the SCMs.

The macrocell corrosion current between the top and bottom steel reinforcement was measured to assess the progress of corrosion in each of the specimens. Figure 3.5 presents the corrosion current density measurements for the top and bottom steel reinforcements during the one-year time window. The corrosion severity of steel is ranked low when the corrosion rate is measured between 0.1 and 0.5 µA/cm2, and intermediate when the corrosion rate is between 0.5 and 1.0 µA/cm2 (Broomfield 2007). As shown in Figure 3.5, the corrosion current density for the KM mixture reached 0.5 µA/cm^2 at the end of the 220th day (i.e., 32 weeks), indicating a high risk of steel corrosion. However, no significant difference was observed between the corrosion current density of the Control and KL mixtures with the current density fluctuating

from 0.05 to 0.15 μA/cm^2. For the mixtures that included the SCMs, the current density was found to remain close to zero, indicating a significant improvement in the corrosion resistance of the concrete mixtures made with the addition of SCMs to shrinkage-compensating cement.

In addition to the measured currents, the corrosion rate was calculated based on the Faraday's law in terms of metal loss (Darwin et al. 2002):

$$r = \frac{ia}{nFD} \quad (2)$$

where r represents the corrosion rate (μm/year); i is the corrosion current density (amp/cm^2 or coulombs/cm^2·sec); a is the atomic weight, 55.84 g for iron; n is the number of electrons exchanged, 2 for Fe^{2+}; F is the Faraday's constant, which is 96,500 coulombs/mole; and D is the density of the metal, 7.87 g/cm^3 for steel. From the regular measurements of the corrosion current density, the corrosion rate at the end of the first year is calculated. The outcome of this calculation indicates that the corrosion rate increased from 0.43 μm/year for the control mixture to 3.11 μm/year after the incorporation of a 15% dosage of shrinkage-compensating cement. On the other hand, the corrosion rate of the samples improved with fly ash or silica fume dropped again to the negligible value of 0.33 μm/year.

After the salt exposure test, the concrete samples were broken, and the embedded steel bars were examined for the signs of corrosion. As shown in Figure 3.6, no corrosion was observed in the control mixture that contained no Type K expansive agent. The corrosion issue, however, emerged in the KM mixture with apparent signs of local corrosion. This issue was resolved in the KM+SF mixture, which delivered both shrinkage-compensating behavior and corrosion resistance. As reflected in the three reported measurements along with direct visual observations, the corrosion resistance of the shrinkage-compensating concrete mixtures is

significantly improved by adding fly ash or silica fume. This is mainly because they reduce the porosity of the concrete matrix by blocking the pores. Thus, they minimize the penetration of water and chloride ions towards the embedded steel bars. This important aspect has been investigated in detail through a set of tests designed to evaluate the transport properties of the developed mixtures.

3.6 Investigation of Transport Properties

3.6.1 Air Permeability

Air permeability is one of the parameters that directly affect the durability of concrete and the corrosion of steel reinforcement embedded in it (Neves et al. 2015; Sanjuán and Muñoz-Martialay 1995). The air permeability of the developed concrete mixtures was evaluated by monitoring the loss of air pressure with time. Figure 3.7 shows how the air pressure loss (P_t/P_0, where P_0 and P_t represent the initial pressure and the pressure at time t, respectively) changes over time. It is evident that the air pressure dropped significantly as the dosage of Type K expansive agent increased from 0 to 15%. To further quantify the effect of dosage, the Darcy coefficient of permeability, k, was calculated using the following equation:

$$k = \frac{\omega V g d z}{R A \emptyset} \tag{3}$$

where ω is the air's molecular mass (28.97 g/mol); V is the volume of the air under pressure (m^3); g is the acceleration due to the gravity (9.81 m/s^2); d is the thickness of the disk sample; z is the slope of the relationship between $\ln(P_0/P_t)$ and time; R is the universal air constant (8.313 J/K.mol); A is the cross-sectional area of the sample; and $\emptyset$ is the room temperature (K).

With the input of z extracted from the test results, Table 3.5 summarizes the Darcy coefficient of permeability for all the tested samples. Specifically, the k value in the KL and KM mixtures experienced an increase of 7.1% and 63.7% when the Type K cement dosage was increased from none to 7.5% and from 7.5% to 15%, respectively. This indicates how the inclusion of shrinkage-compensating cement in the mixtures increases the air permeability of the concrete matrix. The addition of SCMs was also found helpful, as they were able to reduce the Darcy coefficient of permeability to 9.81 ($\times 10^{-8}$ m/s), which was even less than that of the control mixture, i.e., 9.97 ($\times 10^{-8}$ m/s).

Moreover, the air permeability index (API) was calculated based on the measured Darcy coefficient of permeability using Equation 4.

$$\text{API} = -\log_{10}(k) \tag{4}$$

As summarized in Table 3.5, a higher API indicates a lower permeability of the concrete matrix. The obtained results highlight that the addition of SCMs led to the mitigation of the air permeability issue. This can be attributed to not only the refinement of the concrete's pore structures as a result of pozzolanic reactions, but also the filler effect of the SCM particles (Ann et al. 2008).

3.6.2 Capillary Absorption and Pore Characteristics

The capillary absorption test examines the transportation of water through the capillary pores of concrete (after hydration) and reports the concrete's effective porosity. The sorptivity coefficient of the developed concrete mixtures was determined in this study by monitoring the rate of water absorption for eight days, according to the following equation:

$$I = S_i\sqrt{t} \tag{5}$$

where I is the cumulative amount of water absorption per unit cross-sectional area of the specimen (g/mm^2); S_i is the sorptivity coefficient (g/mm^2/sec$^{1/2}$); and t is the time in seconds. Figure 3.8 shows the results obtained during the first stage (i.e., the first six hours) and second stage (i.e., up to eight days) of the capillary absorption test. In the first stage, the control samples showed a 46% and 58% lower absorption of water compared to the KL and KM mixtures, respectively. On the other hand, the addition of SCMs significantly reduced the amount of absorbed water. More specifically, the KM+FAF, KM+FAC, and KM+SF mixtures demonstrated an average reduction of 60%, 34%, and 18% compared to the KM mixture, respectively. A similar trend can be observed in the second stage, during which the KL and KM mixtures absorbed the highest amount of water, while the mixtures with the SCMs, particularly silica fume and Class F fly ash, mitigated the high water absorption issue.

Table 3.6 documents the sorptivity coefficient, which is defined as the slope of the line fitted to the sorptivity data measured for each of the concrete mixtures. According to this table, the sorptivity coefficient is consistently higher at the first stage due to the relatively large concentration gradient resulted from the unsaturated pore structure condition in the concrete matrix. This coefficient then drops in the second stage, mainly because the pore structure has reached a saturated state (Mohamad and Evans 2018). It can also be found that the initial rate of water absorption significantly increased from 0.8 ($\times 10^{-3}\,\mathrm{mm}/\sqrt{\mathrm{s}}$) to 1.9 ($\times 10^{-3}\,\mathrm{mm}/\sqrt{\mathrm{s}}$) after the portland cement was replaced by Type K expansive agent in the concrete specimens. However, when the SCMs were included in the mixtures, the rate of water absorption reduced to a rate close to the control mixture.

The capillary pores, ranging from 0.01 μm to 10 μm, distributed in the concrete matrix, are known to govern the sorption process at the first stage of water sorptivity (Gong et al.

2014). During the second stage of water sorptivity, however, the gel pores dictate the rate of water flow (Martys and Ferraris 2007). To properly investigate the effect of pore size distribution on the capillary absorption of the developed concrete mixtures, the MIP test was conducted on the control, KM, and KM+SF mixtures (Figure 3.9). In comparison of the control and KM mixtures, it can be seen that the capillary micropores (i.e., 0.01 to 0.05 μm) and macropores (i.e., 0.05 to 10 μm) were both increased with the use of Type K expansive agent, which is in agreement with the increased capillary absorption coefficient shown in Figure 3.8. This figure also proves that the use of silica fume reduced the capillary pores of the KM+SF mixture, which, in turn, decreased the capillary absorption coefficient.

3.6.3 Chloride Diffusion

There are a few accelerated electrochemical test procedures for evaluating chloride penetration into the concrete. Among them, the chloride diffusion test was conducted in the current study to estimate the chloride diffusion coefficient over the testing period in accordance with ASTM C1556 (ASTM Committee C09.66 2011). Figure 3.10 presents the chloride ion content of the concrete samples measured in eight layers, beginning from the surface to the depth of 22.5 mm. The apparent chloride diffusion coefficient for each mixture was obtained by fitting Equation 6 to the measured chloride ion contents using the least square method.

$$C(x,t) = C_s - (C_s - C_i)\text{erf}\left(\frac{x}{2\sqrt{D_a t}}\right) \quad (6)$$

where $C(x,t)$ is the chloride concentration measured at the depth of x (mm) at the exposure time of t; C_s is the chloride concentration at the interface between the exposure liquid and test specimen; C_i is the initial chloride concentration in the concrete specimen prior to ponding in the salt solution; D_a is the apparent chloride diffusion coefficient obtained from the regression analysis; and erf is the error function. Based on the R^2 values reported in Table 3.7,

it is noted that the lines obtained from the regression analyses fit the recorded chloride profiles well. The overall trend indicated that the chloride ion content in the depth of concrete samples increases with the increase of the dosage of Type K expansive agent. With the addition of SCMs to the concrete specimens that contained 15% Type K expansive agent, the chloride ion content was significantly reduced, especially below the depth of 4 mm. This is in a good agreement with the results reported for the other transport properties and further highlights the positive effect of SCMs to minimize chloride diffusion into shrinkage-compensating cement concretes.

The apparent chloride diffusion coefficients obtained by fitting Equation 6 to the measured chloride ion contents are summarized in Table 3.7, along with their associated R^2 values. It is evident that the apparent chloride diffusion coefficient was doubled by the addition of a 15% dosage of Type K expansive agent. On the other hand, when fly ash Class F, fly ash Class C, and silica fume were included in the mixtures, the apparent chloride diffusion coefficient dropped by 25.0%, 67.8%, and 63.7% in comparison with the KM mixture, respectively. The observations and measurements made during the tests on transport properties properly support the choice of SCMs identified in the current study. This provides a potential solution to mitigate the chloride ion ingress and corrosion of steel reinforcement in the concretes made with shrinkage-compensating cements.

3.7 Conclusions

This study investigated the reinforcement corrosion and ion transport in the concrete mixtures made with Type K expansive agent and SCMs. For this purpose, a holistic set of long-term corrosion tests paired with air permeability, capillary absorption, MIP, and chloride diffusion tests were performed. The observations and measurements from the corrosion tests

showed strong correlations with the transport properties obtained for the developed mixtures. The increased corrosion rate through the addition of Type K expansive agent was accompanied by an increase in air permeability, capillary absorption, and chloride diffusion. When a higher dosage of Type K expansive agent was used, a higher permeability of destructive agents (i.e., chloride ions, water, and oxygen), and thus, higher corrosion rate were observed. This was supported by the findings from the MIP tests, in which the porosity of concrete samples was found to increase from 0.68 cm^3/g to 0.77 cm^3/g when 15% of portland cement was replaced with Type K expansive agent. This further quantified how the shrinkage-compensating properties of Type K expansive agent come with the expanse of increased permeability and risk of reinforcement corrosion over time.

To address this issue, three SCMs, i.e., fly ash Class C, fly ash Class F, and silica fume, were investigated as possible additions to the concrete mixtures made with Type K expansive agent. For this investigation, the same series of tests were performed to evaluate how these SCMs can improve the transport properties and corrosion resistance of the developed mixtures. Upon completing the long-term corrosion as well as the transport properties tests, it was revealed that the addition of the selected SCMs successfully minimized the risk of corrosion in the steel bars embedded in shrinkage-compensating cement concrete mixtures. This conclusion was made based on the negligible corrosion rate accompanied by the minimum air permeability and chloride diffusion coefficient in the mixtures that contained the SCMs. Such mixtures also mitigated the negative effect of Type K expansive agent on capillary absorption. Through the MIP test results, this was attributed to the refinements made in the pore structure of the SCM-contained mixtures obtained as a result of pozzolanic reactions.

3.8 References

A. Klein, T. Karby, M. Polivka, Properties of an Expansive Cement for Chemical Prestressing, Proceeding of International Concrete Abstracts Portal. 58 (1961) 59–82.

B. Mather, Expansive Cements, U.S. Army Enginner Waterways Experiment Station, Vicksburg, Mississippi. (1970).

Portland Cement Association, Types and Causes of Concrete Deterioration, R&D Serial No. 2617. Portland Cement Association. (2002) 1–16.

ACI Committee 223, Guide for the Use of Shrinkage-Compensating Concrete, Report ACI 223R-10. American Concrete Institute. 2010.

P. Chaunsali, P. Mondal, Physico-Chemical Interaction between Mineral Admixtures and OPC–Calcium Sulfoaluminate (CSA) Cements and Its Influence on Early-Age Expansion, Cement and Concrete Research. 80 (2016) 10–20.

J. Han, D. Jia, P. Yan, Understanding the Shrinkage Compensating Ability of Type K Expansive Agent in Concrete, Construction and Building Material. 116 (2016) 36–44.

H. Nair, C. Ozyildirim, M.M. Sprinkel, Evaluation of Bridge Deck with Shrinkage-Compensating Concrete, Report VTRC 16-R15. Virginia Transportation Research Council. 2016.

K. Ogawa, C4A3S Hydration, Ettringite Formation, and Its Expansion Mechanism: II. Microstructural Observation of Expansion, Cement and Concrete Research. 12 (1982).

W. Shi, M. Najimi, B. Shafei, Investigation of Chloride Penetration in Shrinkage-Compensating Cement Concretes, Under Review. (2019).

I. Battaglia, Experimental Use of Type K Cement Concrete in Wisconsin Highway Bridge Decks, Report No. FEP-04-12. Wisconsin Department of Transportation. (2012).

AASHTO T277-07, Standard Test Methods for Preparing Precision and Bias Statements for Test Methods for Construction Materials. Standard Specifications for Transportation Materials and Methods of Sampling and Testing, Part 2B: AASHTO, Washington D.C, 2006.

M.D. D'Ambrosia, J. Slater, High-Performance Concrete for Bridge Decks Final Report, CTL Group Project No. 057122. (2013).

ASTM G109-07(2013), Standard Test Method for Determining Effects of Chemical Admixtures on Corrosion of Embedded Steel Reinforcement in Concrete Exposed to Chloride Environments, ASTM International, West Conshohocken, PA, 2013.

ASTM C876-15, Standard Test Method for Corrosion Potentials of Uncoated Reinforcing Steel in Concrete, ASTM International, West Conshohocken, PA, 2015.

ASTM C33 / C33M-18, Standard Specification for Concrete Aggregates, ASTM International, West Conshohocken, PA, 2018.

ASTM C192 / C192M-18, Standard Practice for Making and Curing Concrete Test Specimens in the Laboratory, ASTM International, West Conshohocken, PA, 2018.

ASTM C39 / C39M-18, Standard Test Method for Compressive Strength of Cylindrical Concrete Specimens, ASTM International, West Conshohocken, PA, 2018.

ASTM C157 / C157M-17, Standard Test Method for Length Change of Hardened Hydraulic-Cement Mortar and Concrete, ASTM International, West Conshohocken, PA, 2017.

M.J. Alexander, Durability indexes and their use in concrete engineering, Univ. Cape T. (2005) 9–22. doi:10.1617/2912143586.002.

ASTM C1585-13, Standard Test Method for Measurement of Rate of Absorption of Water by Hydraulic-Cement Concretes, ASTM International, West Conshohocken, PA, 2013.

ASTM C1556-11a(2016), Standard Test Method for Determining the Apparent Chloride Diffusion Coefficient of Cementitious Mixtures by Bulk Diffusion, ASTM International, West Conshohocken, PA, 2016.

M.A. Sanjuán, R. Muñoz-Martialay, Influence of the age on air permeability of concrete, Journal of Materials Science. 30 (1995) 5657–5662.

R. Neves, B.S. Da Fonseca, F. Branco, J. De Brito, A. Castela, M.F. Montemor, Assessing Concrete Carbonation Resistance through Air Permeability Measurements, Construction and Building Materials. 82 (2015) 304–309.

K.Y. Ann, H.Y. Moon, Y.B. Kim, J. Ryou, Durability of Recycled Aggregate Concrete Using Pozzolanic Materials, Waste Management. 28 (2008) 993–999.

B. MN, F. Mohamad, R. Evans, R. MM, Assessment of Sorptivity Coefficient in Concrete Cubes. Discovery, 2018, 54(274), 377-386.

J. Wu, H. Li, Z. Wang, J. Liu, Transport Model of Chloride Ions in Concrete Under Loads and Drying-Wetting Cycles, Constructional Building Materials. 112 (2016) 733–738.

ASTM C1202-19, Standard Test Method for Electrical Indication of Concrete's Ability to Resist Chloride Ion Penetration, ASTM International, West Conshohocken, PA, 2019.

NT BUILD 492, Concrete, Mortar and Cement-Based Repair Materials: Chloride Migration Coefficient from Non-Steady State Migration Experiments, Nordtest, Espoo, Finland, (1999).

ASTM C1556-11a (2016), Standard Test Method for Determining the Apparent Chloride Diffusion Coefficient of Cementitious Mixtures by Bulk Diffusion, ASTM International, West Conshohocken, PA, 2016.

R.M. Park, A Guide to Understanding Reference Electrode Readings, Materials Performance. (2009) 32–36.

ASTM C876-15, Standard Test Method for Corrosion Potentials of Uncoated Reinforcing Steel in Concrete, ASTM International, West Conshohocken, PA, 2015.

J.P. Broomfield, Corrosion of Steel in Concrete: Understanding, investigation and repair, 2nd Edition, 2007.

D. Darwin, J. Browning, T. Van Nguyen, J. C.E. Locke, Mechanical and Corrosion Properties of a High-Strength, High Chromium Reinforcing Steel for Concrete," SM Report No. 66, University of Kansas Center for Research, Inc., Lawrence, Kansas, March (2002) 142.

Table 3.1. Chemical composition of binders (% weight).

Type of Binder	**CaO**	**SiO_2**	**SO_3**	**Fe_2O_3**	**Al_2O_3**	**MgO**	**K_2O**	**Na_2O**	**TiO_2**
Porland Cement	62.94	20.10	3.18	3.09	4.44	2.88	0.61	0.10	0.24
Shrinkage-Compensating Cement	65.40	1.80	25.10	1.20	4.80	1.40	0.10	–	–
Fly Ash F	15.78	50.87	0.61	5.27	20.17	3.19	1.09	0.69	1.29
Fly Ash C	21.54	42.46	1.20	5.51	19.46	4.67	0.68	1.42	1.48
Silica Fume	0.30	94.30	–	0.10	0.09	0.43	0.83	0.27	–

Table 3.2. Physical properties of fine and coarse aggregates.

Aggregate Type	**Bulk Specific Gravity**	**SSD Specific Gravity**	**Absorption (%)**	**Dry Rodded Unit Weight (kg/m^3)**	**Fineness Modulus**
Fine aggregates	2.77	2.79	0.90	–	3.0
Coarse aggregates	2.76	2.77	0.40	1653	–

Table 3.3. Mixture proportions developed for the current study.

Mix. ID	PC	KC	SF	FA-F	FA-C	Water	Fine Agg.	Coarse Agg.	Type K Dosage	w/c
	kg/m^3								(%)	(%)
Control	404.3	0.0	0.0	0.0	0.0	202.0	565.4	1089.9	0.0	0.5
KL	374.0	30.3	0.0	0.0	0.0	202.0	565.4	1089.9	7.5	0.5
KM	343.7	60.6	0.0	0.0	0.0	202.0	565.4	1089.9	15.0	0.5
KH	313.3	91.0	0.0	0.0	0.0	202.0	565.4	1089.9	22.5	0.5
KM+FAF	283.0	60.6	0.0	60.6	0.0	202.0	565.4	1089.9	15.0	0.5
KM+FAC	283.0	60.6	0.0	0.0	60.6	202.0	565.4	1089.9	15.0	0.5
KM+SF	315.4	60.6	28.3	0.0	0.0	202.0	565.4	1089.9	15.0	0.5

Table 3.4. Summary of previous conducted results of compressive strength and length change measurement.

Mix. ID	Length change measurement (%)			Compressive strength
	7th day	28th day	56th day	(MPa)
Control	-0.001	-0.037	-0.045	47.88
KL	0.015	-0.016	-0.024	55.04
KM	0.059	0.020	0.001	54.77
KH	0.267	0.262	0.232	4.55
KM+FAF	0.065	0.033	0.029	44.88
KM+FAC	0.028	-0.006	-0.017	53.90
KM+SF	0.039	-0.003	-0.011	57.58

Table 3.5. Darcy coefficient of permeability of tested specimens.

Mix ID	Darcy coefficient of permeability, k ($\times 10^{-8}$ m/s)
Control	9.97
KL	10.68
KM	17.48
KM+FAF	13.71
KM+FAC	10.18
KM+SF	9.81

Table 3.6. Coefficient of capillary absorption of concrete specimens containing different dosages of Type K agents and SCMs.

Mix ID	Control	KL	KM	KM+FAF	KM+FAC	KM+SF
Initial rate ($mm/\sqrt{s}$)	0.8×10^{-3}	1.9×10^{-3}	1.9×10^{-3}	1.0×10^{-3}	1.7×10^{-3}	1.4×10^{-3}
Secondary rate ($mm/\sqrt{s}$)	0.7×10^{-3}	1.2×10^{-3}	1.3×10^{-3}	1.0×10^{-3}	1.0×10^{-3}	0.7×10^{-3}

Table 3.7. Apparent chloride diffusion coefficient in the mixtures under consideration.

Mix. ID	Apparent Chloride Diffusion Coefficient ($\times 10^{-11}$ m^2/s)	R^2
Control	1.71	0.86
KL	1.93	0.97
KM	3.48	0.95
KM+FAF	2.61	0.97
KM+FAC	1.12	0.92
KM+SF	1.26	0.97

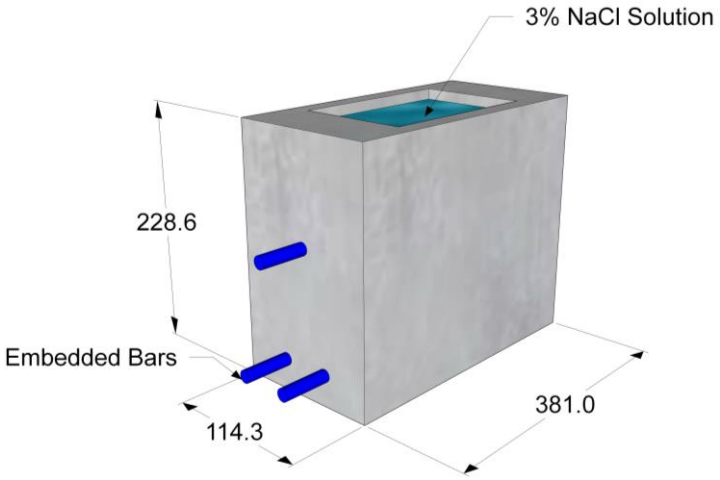

(a)

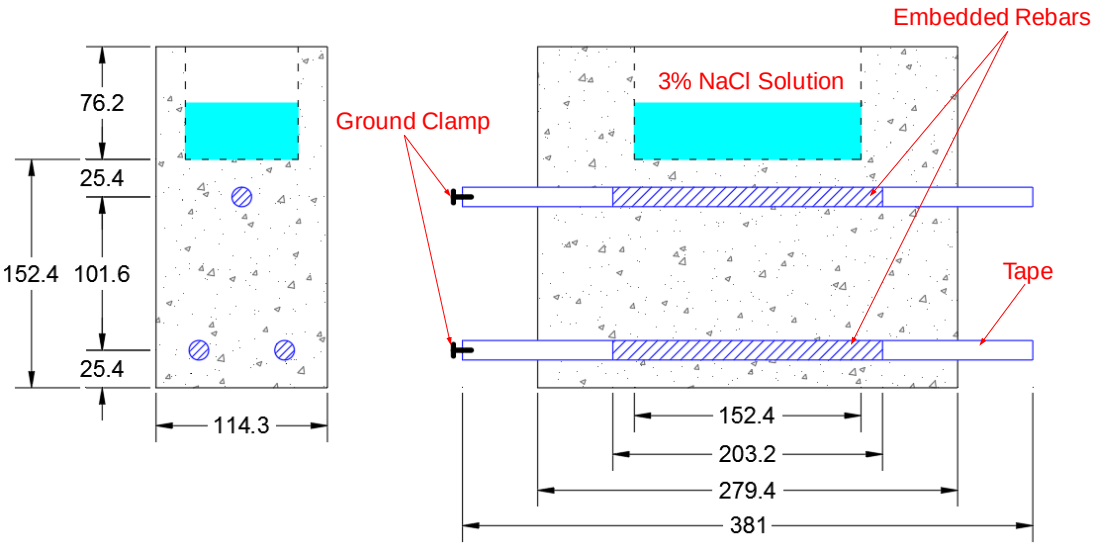

(b)

Figure 3.1. *Setup developed for the rebar corrosion tests: (a) 3D view, and (b) two side views. All the dimensions are in mm.*

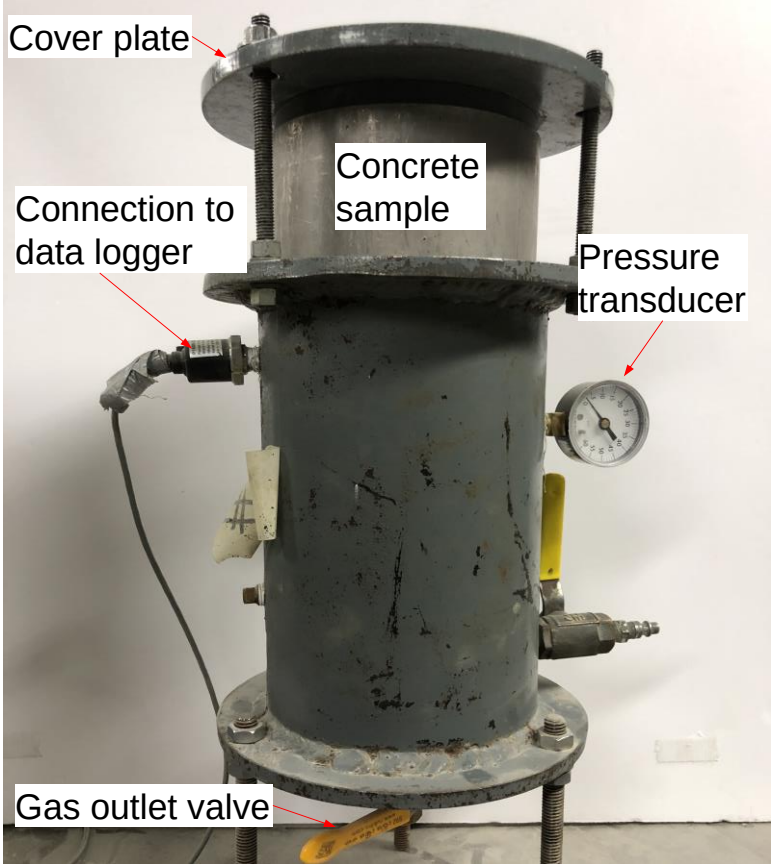

Figure 3.2. *Test set-up of air permeability apparatus.*

Figure 3.3. *Long-term corrosion test setup.*

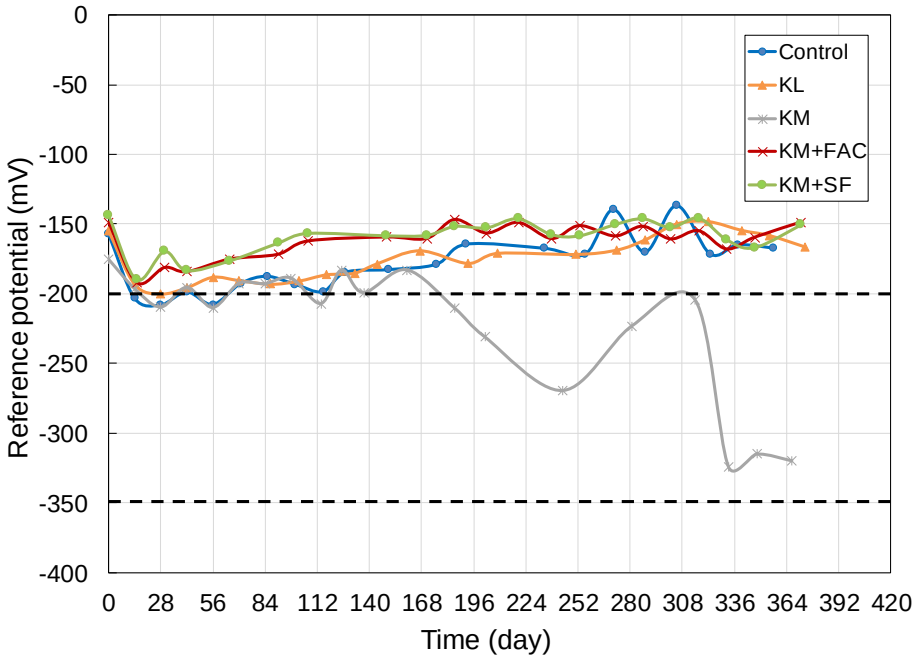

Figure 3.4. *Half-cell potential measurements relative to copper/copper sulfate (Cu/CuSO4) electrode for the top reinforcement.*

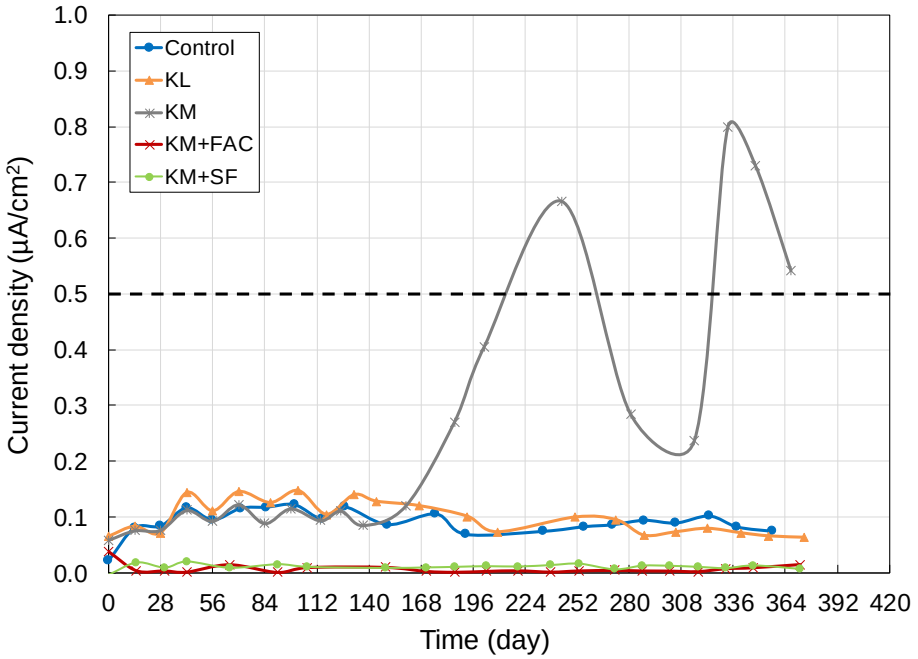

Figure 3.5. *Corrosion current density measurements for the top and bottom reinforcements.*

(a)

(b)

(C)

Figure 3.6. *Examination of the steel bars after one year in the corrosion setup: (a) Control, (b) KM, and (c) KM+SF mixtures.*

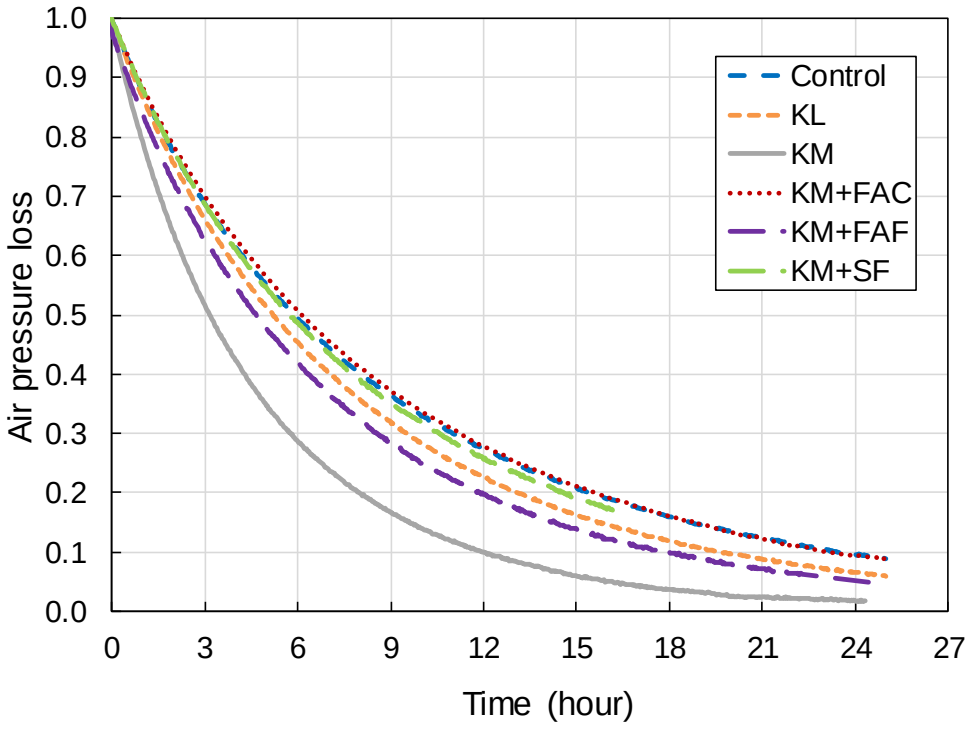

Figure 3.7. *Air permeability test results for the developed mixtures.*

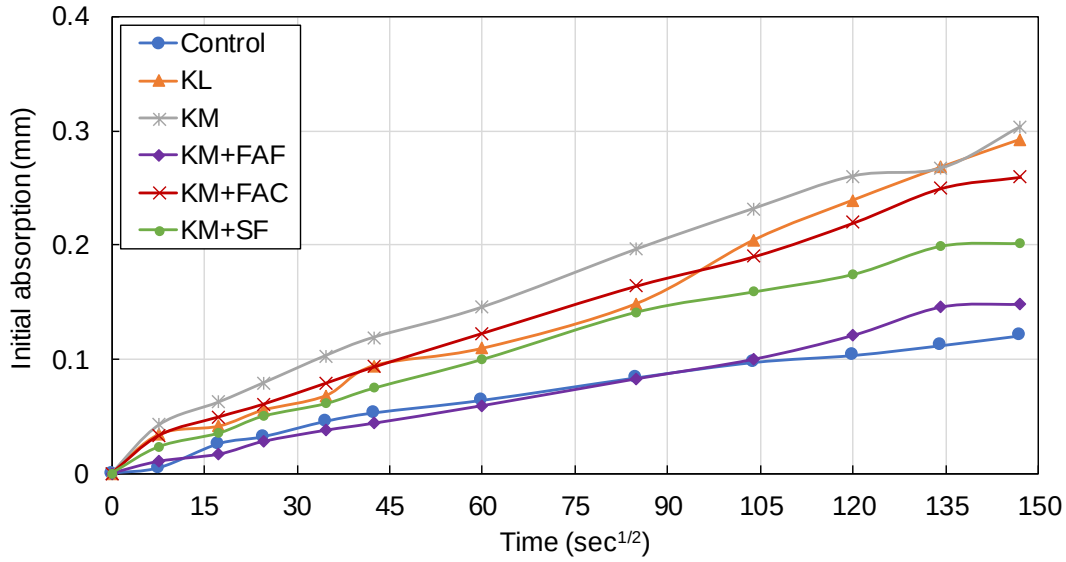

(a)

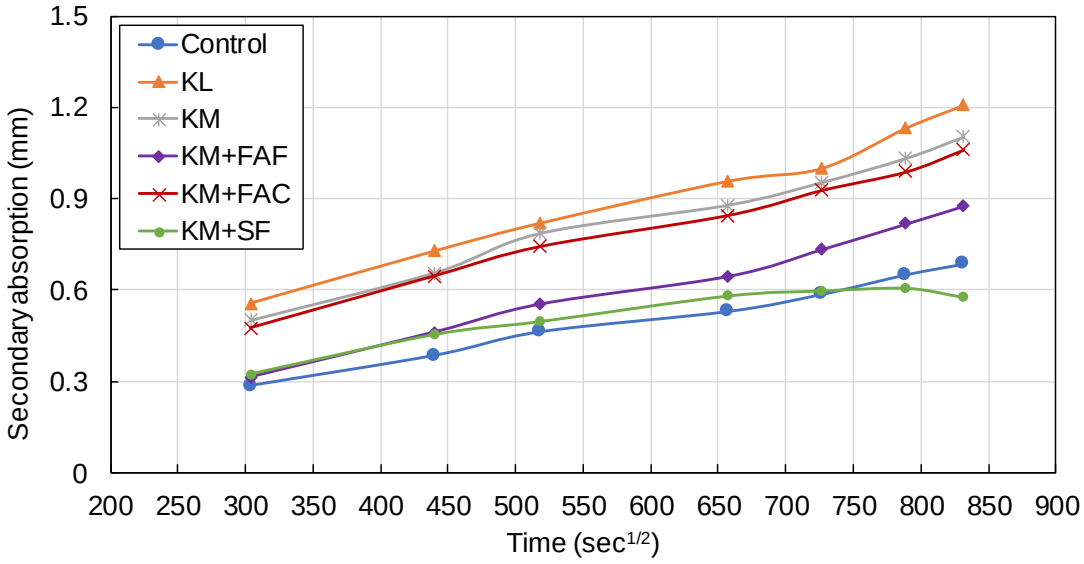

(b)

Figure 3.8. *Rate of water absorption in the tested concrete mixtures: (a) during the first six hours, and (b) up to eight days.*

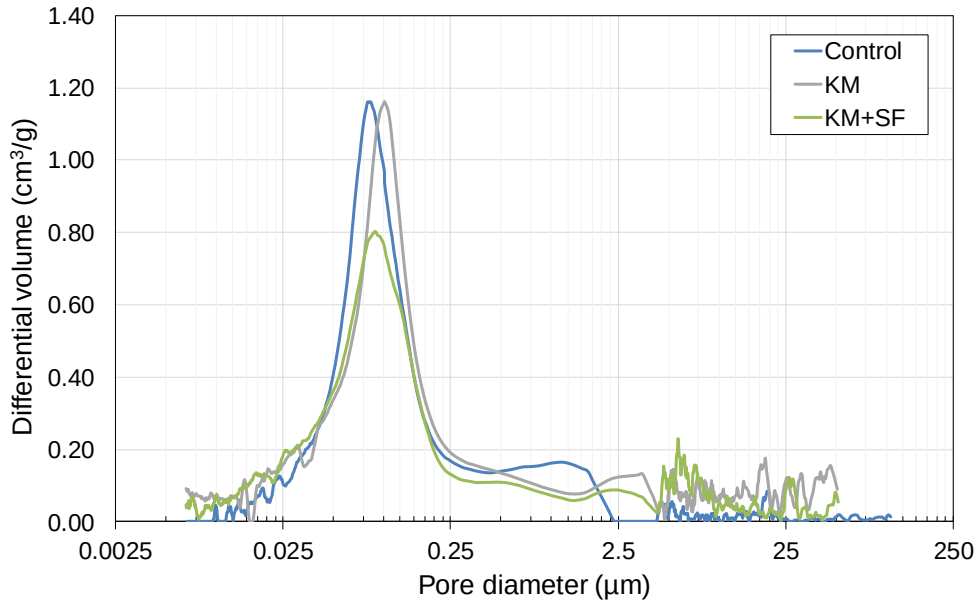

(a)

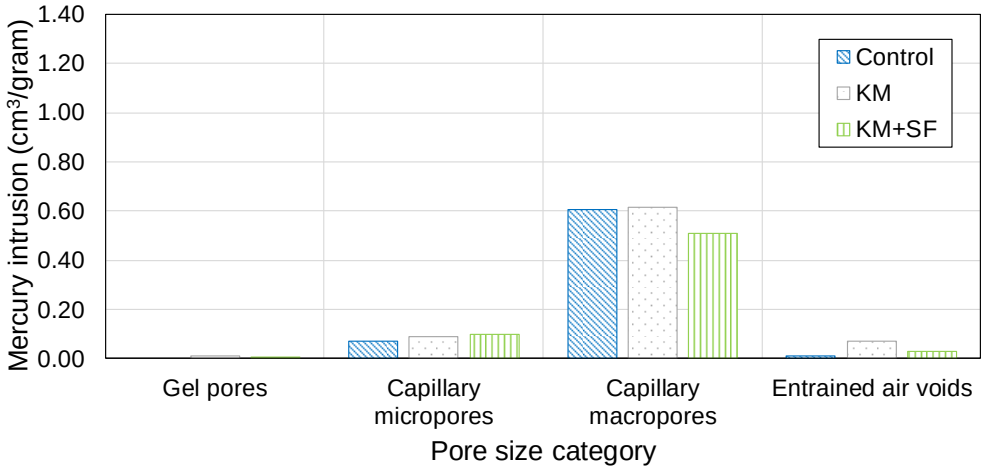

(b)

Figure 3.9. *Results of MIP tests: (a) total intrusion volume of mercury, and (b) intrusion volume of mercury in different pore size categories.*

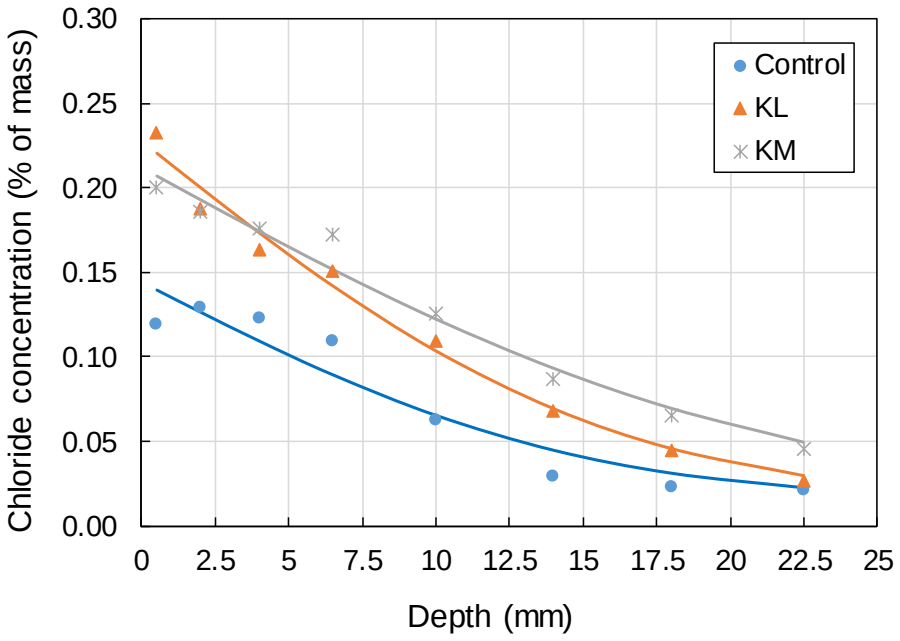

(a)

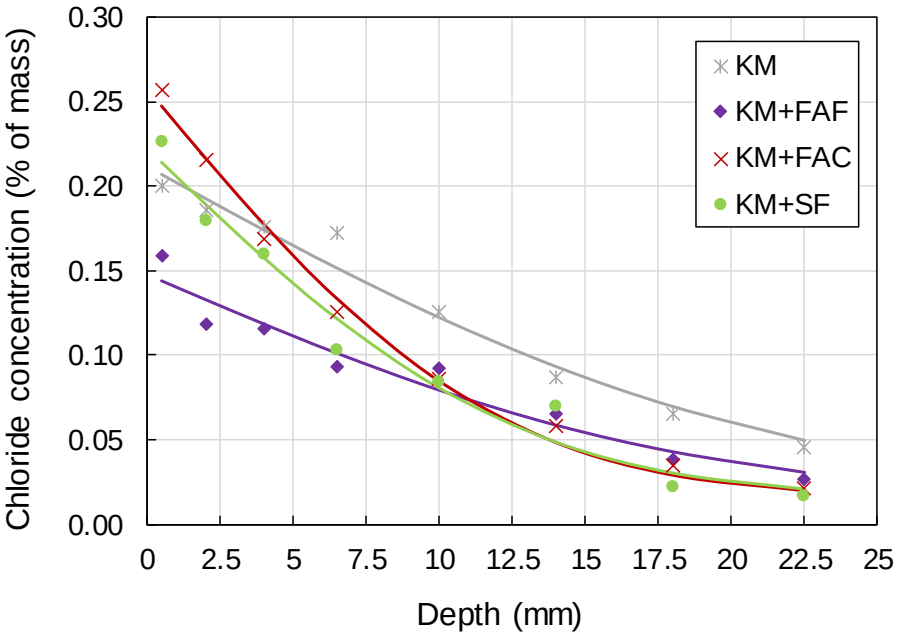

(b)

Figure 3.10. *Chloride concentration recorded at different depths below the exposed surface for the mixtures: (a) with and without Type K expansive agent, and (b) with and without SCMs.*

CHAPTER 4. EXPERIMENTAL AND NUMERICAL INVESTIGATION OF STRUCTURAL BEHAVIOR OF REINFORCED LONGITUDINAL JOINTS IN BRIDGES WITH ADJACENT BOX BEAMS UNDER THERMAL LOADS

4.1 Abstract

Longitudinal joints used to connect adjacent box beams in bridges are known to experience early-age cracks due to a variety of environmental and mechanical stressors, including diurnal temperature changes, hydration, drying shrinkage, restrained shrinkage, etc. Such cracks can open a direct path for water and deleterious agents to penetrate into the structural system, causing corrosion of embedded steel bars and structural degradation of bridge superstructure and substructure elements. To mitigate this problem, one innovative solution developed in this study was using Type K shrinkage-compensating cement, which can greatly enhance the volume stability of concrete, increase the serviceability of structures, and thus develop an optimized solution for issues regarding the early-age deterioration for longitudinal joints in bridges. In this study, a test setup consisting of two full-scale box beams connected with concrete made with Type K shrinkage compensating cement is investigated to understand the structural response of bridge superstructure under various temperature profiles at top and bottom. Data consisting of temperature, longitudinal and transverse strain, and beam deflection are collected during the thermal tests at the joint and each box beam. A set of three-dimensional finite-element simulations are also performed to extend the scope of investigations beyond the cases tested in the laboratory. The obtained results from both test and FE analysis showed that under the daily temperature difference, heat of hydration, joint concrete expansion, the stress in the joint is lower than the yield strength of the material, and the transverse stress is also lower than the bond strength of the interface. The outcome of this study provides an

important step forward in introducing materials for minimizing damage to bridge elements under various sources of thermal loads.

***Keywords*:** Box-beam bridges; Joints; Type-K shrinkage compensating cement; Finite Element Analysis; Thermal Loads.

4.2 Introduction

Precast box-beam bridges have been widely used by transportation agencies for short- and medium-span bridges, especially those serving secondary roads. This type of bridge superstructure has been adopted primarily because of relatively low depth-to-span length ratio, simple design, ease of construction, and reasonable maintenance needs. In principle, such a bridge superstructure is constructed by placing precast concrete box beams next to each other, connecting them by casting shear keys, applying transverse post-tensioning forces on a need basis, and then placing either a thin overlay or a thick structural deck (Russell 2009). Despite the overall success of this structural system, longitudinal cracks are commonly observed at the interface of the box beams and the shear key (Arthur A.Huckelbridge and El-Esnawi 1997; Russell 2009; Miller 1999; Steinberg, et al., 2011; Lei. et al., 2015). Because of longitudinal cracks, a direct path for the penetration of water and deleterious agents into the bridge superstructure and substructure is formed. This causes corrosion of embedded steel reinforcement, degradation of structural elements, and excessive differential deflections between adjacent beams, especially if the longitudinal joints cannot meet the expected performance requirements. This adversely affects the strength and serviceability of the bridge and may require extensive maintenance and repair activities.

During their service life, box-beam bridges experience a number of environmental and mechanical stressors, primarily originated from temperature and shrinkage effects, as well as

live loads (Huckelbridge Jr. et al. 1995). Among these stressors, many bridges are exposed to significant daily and/or seasonal temperature changes. The adverse consequences due to such temperature changes are, however, magnified when the joints also experience exothermic cement hydration processes, particularly in early age. In Miller (1999), a full-scale, four-beam assembly comprised of three joint configurations was studied to understand the thermal effects. It was observed that, although the epoxy used for longitudinal joints can provide a high bond strength, longitudinal cracks are still initiated and propagated if the ambient temperature range exceeds a certain limit, mainly because the coefficient of thermal expansion of the epoxy was two to three times higher than that of concrete. This led to differential displacements that opened some joints and closed the others. Attanayake and Aktan (2008) monitored a box beam bridge during and after construction with the objective of understanding the shear key behavior. Longitudinal deck cracks were observed a few days after construction before the bridge was opened to traffic. The cracks, which remained open even after applying transverse post-tensioning forces, eventually propagated through the deck thickness. In a follow-up study, Attanayake et al. (2010) investigated the effectiveness of post-tensioning applied through discrete diaphragms. It was reported that transverse tensile stresses of up to 100 psi can be generated at the top of shear keys, posing a significant potential for exceeding the bond strength at the interface. While a two-stage post-tensioning application reduced the transverse stresses along the bottom and top surfaces of the deck exposed to temperature effects, a similar benefit was not obtained for the shear keys due to the lack of uniform compression under the transverse post-tensioning forces. Thus, it was recommended that an optimized design of connection details is imperative in both longitudinal and transverse directions. In a separate study, Steinberg (2011) also observed several longitudinal cracks in the joints of box-beam bridges.

One of them occurred within only three days after the shear key was filled. In another instance, cracks were found in the mid-depth shear key within just one week after grouting with the temperature effect identified as the root cause. Grace et al. (2012) investigated the structural performance of shear keys under a combination of temperature gradients and traffic loads using both half-scale laboratory tests and numerical simulations. The study reported that the traffic load did not directly result in initiating longitudinal cracks, contrary to the temperature gradient, which was found to be the main stressor causing cracks in the longitudinal joints.

The Federal Highway Administration (FHWA) has explored the use of ultra-high performance concrete (UHPC) for adjacent box beam bridges to enhance their strength and serviceability (Yuan and Graybeal 2014, 2016; Semendary, et al., 2017; Rikabi, et al., 2017a, b). Yuan and Graybeal (2014, 2016) conducted a study to evaluate UHPC as an alternative material for shear keys and found that longitudinal cracks did not initiate under ten thermal loading cycles. In the referenced study, two types of joint materials, i.e., conventional grout and UHPC, were examined, one in a partial-depth and the other in a full-depth joint. To compare the thermal behavior, a 50 °F (28 °C) temperature difference was applied to the top and bottom of box beams by pumping steam. A deflection of 0.42 in. (11 mm) was reported at the mid-span after ten thermal loading cycles with no cracks or debonding at the joints. Hussein et al. (2017) and Sargand et al. (2017) performed a series of numerical simulations and confirmed the load transfer mechanisms for shear keys made with UHPC in adjacent box-beam bridges. The main issue reported for the use of UHPC in shear key connections is the high price and level of expertise needed for proper mixing, casting, and curing. It is, therefore, essential to identify and implement alternative joint materials that not only meet structural

performance requirements, but also offer economic advantages given the number of bridges built with box beams.

Considering that one of the primary causes of cracking in adjacent box beam bridges is the shrinkage of materials placed in the longitudinal joints, the current study investigates the use of Type K shrinkage-compensating cement as a partial replacement of portland cement. The main components of this type of cement are tetracalcium trialuminate sulfate ($4CaO{\cdot}3Al_2O_3{\cdot}SO3$, abbreviated as $C_4A_3\bar{S}$), anhydrite ($CaSO_4$), and lime (CaO). Contrary to portland cement concrete, the shrinkage-compensating cement concrete benefits from the formation of a relatively large volume of ettringite, which counteracts shrinkage effects through early-age expansion (Ogawa 1982; Péra and Ambroise 2004). The bridge application of shrinkage-compensating cement concrete was first in bridge decks, for which the drying shrinkage cracks were found to be successfully mitigated (Gruner and Plain 1997). Folliard et al. (2003) evaluated the resistance of different concretes, such as fiber-reinforced concrete, shrinkage-compensating concrete, concrete with shrinkage-reducing admixture, and extensible concrete, to restrained drying shrinkage. It was reported that the early-age expansion originated from Type K cement can provide a superior performance to overcome the shrinkage. Xi et al. (2003) conducted a study to understand causes of early-age cracking in newly constructed bridge decks. It was found that 82% of the inspected bridge decks had various degrees of cracking and the high early age shrinkage of concrete was the main contributor to the problem.

The Wisconsin Department of Transportation constructed five bridge decks using Type K cement and no shrinkage-induced cracks were observed during the monitoring period (Battaglia 2012). Han et al. (2016) investigated both of shrinkage and compressive strength of shrinkage-compensating cement concrete mixtures at 3, 7, and 28 days after casting. It was

found that the use of this type of cement reduced the drying shrinkage and enhanced the performance under restrained drying shrinkage. This was achieved with no adverse effects on the compressive strength compared to ordinary portland cement concrete. Nair et al. (2016) investigated a set of bridge decks to evaluate the effectiveness of shrinkage-compensating cement concrete in field applications. Fewer transverse cracks were observed on the bridge deck made with Type K cement than that made with portland cement. However, several longitudinal cracks were noted because of the differential deflection of the beams. Rahman et al. (2018) conducted a study to investigate the use of Type K cement for reducing the shrinkage-induced cracks. This was found successful because of initial expansion that induced compressive stresses to counteract tensile stresses due to restrained shrinkage. Despite the promising observations made when using shrinkage-compensating cement in bridge decks, there was no study available in the literature on the performance of longitudinal bridge joints made with this type of cement. The main motivation of the current study was to fill this research gap by exploring the use of shrinkage-compensating cement concrete in these longitudinal bridge joints.

In this study, two full-scale box beams were built in the laboratory and connected with concrete made with a 15% replacement of portland cement with Type K shrinkage-compensating cement. The primary focus of the investigation was on thermal effects, especially at early age, due to a combination of diurnal temperature changes and the heat generated during cement hydration reactions. The test scenarios consisted of cycles of heating and cooling for seven days implemented immediately after joint pour. The data collected from the experimental tests included temperature, longitudinal and transverse strain, and deflection at the joint and individual box beams. To extend the scope of investigations beyond the cases

tested in the laboratory, a set of three-dimensional (3D) finite-element (FE) simulations were then performed. The material model used for the longitudinal joint was developed in such a way that the effects of early-age expansion, heat of hydration, and time-dependent mechanical properties were all taken into consideration. Upon validation of the FE model with the experimental test results, additional simulations were performed to obtain an in-depth understanding of how the joints made with Type K shrinkage-compensating cement concrete respond to extreme thermal loading scenarios, including that provided by AASHTO LRFD Bridge Design Specifications.

4.3 Experimental Testing Program

To evaluate the performance of longitudinal joints between box beams under early-age temperature and shrinkage effects, two full-scale box beams were designed, fabricated, and connected by casting a full-depth joint of Type K shrinkage-compensating cement concrete. The two reinforced concrete box beams were identical in cross section with a width of 48 in. (121.9 cm) and total height of 27 in. (68.6 cm) (Figure 4.1), following the current Iowa Department of Transportation's 30 ft. Box Beam Standard. The total length of each beam was 31.2 ft. (9.5 m). Seven #9 steel rebars were used for longitudinal reinforcement. Shear stirrups were #5 steel rebars at the bottom and #4 steel rebars at the top with a spacing of 8 in. (20 cm) close to the supports and 10 in. (25.4 cm) elsewhere. The concrete clear cover was 1.25 in. (3.2 cm) measured from the beam surface to the outer surface of shear stirrups. The box beams were simply supported on neoprene bearing pads, replicating the actual field condition.

The mixture proportions of the box beams and the longitudinal joint have been summarized in Table 4.1. As can be seen in the table, for the concrete mix design used for the joint, 15% of portland cement was replaced with Type K shrinkage-compensating cement,

following the instructions provided by the cement manufacturer (CTS, 2019). To investigate the time dependent interfacial behavior on the shrinkage compensating concrete-normal concrete, the normal stress test was performed using cylinder splitting tensile test performed by Liu (2018) following ASTM C496 under two interface treatments, including surface roughened and no surface roughened but reinforced by #4 rebar. The interface normal bond strength was calculated by dividing the maximum load along the contact plane by the bond area at the interface. Figure 4.2 summarizes the bond strength test results. As can be seen in the plot, the normal bond strength tends to be constant after the first three days. It is significant to highlight that even though the surface is untreated, the specimens with reinforced steel obtained a more promising normal bond strength than the ones without reinforcement steel, which may be due to the dowel action.

A new joint reinforcement detail was designed for this project to improve anchoring between the box beams and the joint. This consisted of a bent steel bar extended from each side of the precast box beams into the joint. Each bent bar was connected to the box beam using a splice system (Dayton 2016), which included a dowel bar with a screw thread embedded into the box beam. The bent bars were further tied with a stirrup to form a closed loop, as shown in Figure 4.1. In addition, four #4 longitudinal steel rebars were embedded in the joint to increase the flexural stiffness. The test setup included duct spaces for 1.5 in. (3.8 cm) diameter transverse posttensioning rods. For this purpose, a total of ten 2.0 in. (5.0 cm) diameter PVC pipes crossing through the beams in the transverse direction were attached to the rebar cage. Considering that one of the objectives of this joint design was to eliminate the transverse posttensioning of box-beam bridges, the prestressing forces were not applied to the rods during the test. In addition, the surfaces of box beams that were in direct contact with joint

materials were roughened by using a form retarder to increase the interface shear resistance and bond strength.

To measure the response of this structural system to early-age temperature and shrinkage effects, four types of sensors, including vibrating-wire strain gauges (VWSGs), electrical-resistance strain gauges (ERSGs), displacement transducers (DTs), and thermocouples (TCs), were employed. The instrumentation plan is shown in Figure 4.3. A total of 36 VWSGs were installed on the top and bottom surfaces of the box beams to obtain the longitudinal and transverse strains at critical locations, such as the ends, quarter-spans, and mid-span of the beams. Six ERSGs were placed on the top and bottom steel rebars of the joint to obtain strain distributions at three sections, i.e., quarter-spans and mid-span. In addition, four DTs were placed at the mid-span underneath the beams to record the vertical deflections. Twelve TCs were embedded in the joint and at the interface between the joint and the beam at the ends and mid-span. The TCs were placed at the top, middle, and bottom of each joint to measure the temperature profile at various depths.

To investigate the joint's performance under temperature variations, a temperature profile was applied in a total of seven heating and cooling cycles, replicating the temperature that a box-beam bridge can experience in reality during the first week after construction. For insulation purposes, a blue-foam box was built on the top surface of the test setup, as shown in Figure 4.4. A total of twenty heating lamps, two heaters, and six fans were distributed on the beam surface to achieve the target temperature profile. A number of preliminary thermal tests were conducted to verify the most optimal locations of the heaters, lamps, and fans. Through regular measurement of temperature inside the insulated box, it was ensured that the expected heating and cooling cycles are created.

4.4 Test Procedure and Results

Temperatures, strains, and deflections were recorded at various locations of the test setup in 2-minute intervals during the seven-day thermal loading test. Figure 4.5 shows the temperature profiles measured with the VWSGs attached on the top and bottom surface of the test setup, as well as the TCs embedded at various depths in the joint. As it can be seen in this figure, the temperature at the bottom surface remains almost constant, representing the ambient temperature in the laboratory. The temperature at the top surface, however, experiences cycles of (approximately) 17 °C (30 °F) variation. During the seven-day testing period, the record high and low temperatures inside the insulated box were recorded to be 41.1 °C (106 °F) and 21.1 °C (75 °F), respectively. No significant variation was observed in the temperatures recorded at different locations on the top surface. It should be noted that the temperature profile recorded at the top surface was found to be influenced by multiple openings and closings of the insulation box at the beginning of the test to setup the heaters, lamps, and fans included for controlling the temperature. Thus, in the absence of reliable temperature recordings for the first few hours, the measured data have been reported for the time period after the test setup was completed and the insulation box was not opened anymore. While the data obtained from the TCs show a similar trend during heating and cooling cycles, a residual temperature was observed near the end portions of the heating and cooling process. This can be attributed to the fact that the surface temperature changes faster than the inside temperature because of the time required for the transfer of heat into the specimen.

To avoid a sharp increase or decrease in temperature, a series of steps were taken, including:

In the heating process, 10 lamps were turned on at the very beginning; another 10 were turned on after 2 hours; and 2 heaters were remained in use after another 2 hours.

In the cooling process, 2 heaters were first turned off; 4 lamps were then turned off every hour until all of them were off; and finally, half of the top foam plates were alternatively removed to cool down the system.

Further to the vertical temperature variation, the change of temperature in the transverse direction from the center of the joint to the interface with the box beam was monitored. This can be seen in Figure 4.6, which illustrates the average temperature difference at five different depths from the top to the bottom surface of the test specimen. With a temperature difference less than 1.1 °C (2 °F), a good thermal consistency can be observed between the joint material and surrounding concrete. Figure 4.7 presents the average transverse strain at the top and bottom surface subjected to the thermal loading cycles, as measured with the VWSGs. Transverse strain is a key measurement, which can reflect the initiation of any longitudinal cracks between the joint and the box beam.

According to the instrumentation layout provided in Figure 4.3, S3-2T(B) and S3-3T(B) were transversely attached near the joint, while S3-1T(B) and S3-4T(B) were transversely placed at the middle of the box beam on both top and bottom surfaces. While all the transverse strain data exhibit a consistent trend with respect to temperature changes, it can be observed in Figure 4.7(b) that the transverse strain becomes negative near the interface, due to cantilever effects. A review of strain ranges indicates that the transverse strain always remains below the cracking strain. It is significant to note that the cracking strain herein was defined as tensile stress of Type K concrete divided by its modulus of elasticity, both of which were determined from the theoretical equation of ACI (2014) based on the compressive strength. Based on a holistic visual inspection performed at regular intervals, the test specimen is found to maintain its structural integrity with no observable cracks. As also can be observed

in Figure 4.7, the temperatures are different when the zero strain takes places for top and bottom fiber, which may be because of the aforementioned residual temperature near each end portion of the heating and cooling process.

4.5 Numerical Simulations

Box-beam bridges are continuously exposed to daily and seasonal temperature variations. Such variations are transferred to the bridge superstructure with a time delay, primarily because of the low thermal conductivity of concrete. As a result, the temperature inside a bridge superstructure can be drastically different from the temperature that the superstructure is exposed to. Such a depth-dependent temperature distribution leads to additional stresses that can induce cracks in adjacent box beams, especially at their joints. To investigate this critical aspect in the longitudinal bridge joints made with shrinkage-compensating cement concrete, a set of heat transfer analyses were conducted on the FE models that replicate the test specimen. In general, temperature, T, at a given location, (x, y, z), of a structure at the time, t, can be determined based on the Fourier's law. The 3D heat transfer equation can be expressed as:

$$k\left(\frac{\partial^2 T}{\partial x^2}+\frac{\partial^2 T}{\partial y^2}+\frac{\partial^2 T}{\partial z^2}\right)+q_v = C\rho\frac{\partial T}{\partial t} \quad (1)$$

where k represents the thermal conductivity in W/(m K); C accounts for the specific heat capacity in J/(kg °K); ρ is the density of concrete in kg/m^3; and q_v represents the rate of heat generation per unit volume in W/m^3.

To include the effect of early-age internal heat generation after casting the joint, the associated heat of hydration was applied as a function of time. The information related to the heat of hydration of shrinkage-compensating cement concrete was obtained from the semi-adiabatic calorimetry tests performed by Sandberg and Liberman (2007).

In the present study, FE simulations were performed using the ABAQUS software package (Simulia 2014) to determine the temperature profiles in the joint and adjacent box beams under various thermal loading scenarios. Such scenarios capture the effect of temperature fluctuations beyond those tested in the laboratory, including the temperature profiles indicated in the AASHTO LRFD Bridge Design Specifications (2016). Following the heat transfer analyses, coupled thermal-stress analyses were performed with the objective of evaluating the structural response of the entire joint setup. For the thermal-stress analyses, temperature data were applied at each time step as a nodal predefined field from the output data of the heat transfer analysis completed in the previous time step.

Figure 4.8 shows the 3D FE model generated based on the test specimen's geometry and structural details. Upon completing a mesh sensitivity analysis, a fine mesh size was used in and near the joint region, while a coarse mesh was applied to the rest of the model to ensure computational efficiency. Table 4.2 provides a summary of concrete material properties used for the current study. The concrete damage plasticity model was employed to take into consideration the concrete's response beyond the elastic range (Simulia 2014). This model also allows stiffness recovery during cyclic loads. Time-dependent material properties were included for the joint to capture early-age changes in the compressive strength, elastic modulus, stress-strain relationship, and shrinkage of Type K shrinkage-compensating cement concrete. According to ACI 209.2R-08 (2008), the following equation can be used for predicting the

time-dependent compressive strength of Type K shrinkage-compensating cement concrete based on the 28-day compressive strength, f_{cm28}.

$$f_c(t) = f_{cm28}(\frac{t}{a + bt}) \quad (2)$$

where f_c is the compressive strength; t is the concrete age in days; and a and b are the constants, assumed equal to 4.0 and 0.85, respectively. The corresponding modulus of elasticity and stress-strain relationship were then updated as a function of time-dependent compressive strength. For time-dependent shrinkage effects, four beam specimens (i.e., 76 mm × 76 mm × 300 mm) were cast with the same batch material used for the joint and cured in the moist room for seven days, during which the length changes were measured following ASTM C157 (2016). This includes one measurement every day in the first 28 days. The test results indicated that the Type K concrete mixture experienced the expansion of approximately total 80 microstrain in the first seven days, while the conventional concrete usually experienced drying shrinkage with approximately 60 microstrain. The shrinkage effect was then implemented into the joint's model by converting the measured shrinkage to an equivalent temperature change that can cause a similar length change.

As for boundary conditions, one end of the model was fixed against translation in all the three orthogonal directions, while the other end was fixed against vertical and transverse translation, but free to move in the longitudinal direction. No rotational constraints were imposed. Such boundary conditions reflected the supports used for the experimental tests. The interface between the joint and each box beam was modeled with a surface-to-surface contact, which captured both friction and shear failure. The friction coefficient between similar concretes was assumed as 1.0 following the recommendation made in the PCI Bridge Design Manual (PCI 2015). Bischaff (2004) investigated the shear bond strength between the old

concrete and patching materials. It was found that the patch material containing Type K shrinkage compensating cement had the highest shear bond strength, with a value of 7.2 MPa. Considering that sliding/debonding can occur when the shear stress exceeds a critical threshold, a threshold of 5.5 MPa was assumed in the current modeling.

4.6 Simulation Results and Discussions

To validate the developed FE models, temperature profiles similar to those applied to the test specimen were first employed. Figure 4.9 compares the temperature distributions predicted by the heat transfer analysis at different depths with the data measured during the thermal loading test. It can be seen that the temperature profiles obtained from the FE simulations are consistent with those measured during the experimental test. The largest temperature difference is in the range of 1 to 2 °C, which occurs at the mid-depth of the joint within the first day of curing. This can be attributed to the complex early-age reactions that are often influenced by the ambient temperature and curing environment. To further validate the model, mid-span deflections are extracted from the thermal-stress analysis. According to Figure 4.10, the deflections predicted for the FE model are very close to those recorded during the experiment. The result indicated that the deflections predicted from FE simulations were in a good agreement with those measured from the test. A slight delay, however, occurs between the peak temperature and the displacement.

The longitudinal and transverse strains on the top surface of the box beam subjected to seven cycles of heating and cooling were compared based on the FE simulation results and experimental test measurements. Table 4.3 presents a summary of the maximum transverse strains near the joint and at the middle of the box beam. This table shows that the maximum strains predicted with the FE model are comparable with those measured during the experiment.

The difference near the joint ranges from -13.5% to +13.9%, while the difference at the middle of the box beam varies from -30.6% to +5.1%. Similarly, the maximum longitudinal strains obtained from the top surface of the box beam at mid-span are compared with the FE model predictions (Table 4.4). The values show a reasonable consistency with a difference, ranging from -14.6% to 9.3%.

Upon ensuring that the FE models properly capture the expected temperature distributions, as well as main structural response measures, the investigations were extended to examine the range of strains/stresses that the joint and adjacent box beams experienced in early age. This was performed to supplement the observations made regarding the possibility of cracking during the experimental tests. For example, Figure 4.11 shows the predicted evolution of temperature and maximum principal stress at the interface of the joint and adjacent box beam at the mid-span. The temperature profiles along the depth of the joint can be employed to find the maximum and minimum expected temperatures. According to Figure 4.11 (a), the highest temperature gradient was predicted close to the surfaces, where a direct exposure to the ambient temperature exists. The temperature profiles can then be paired with the maximum principal stress distributions along the depth of the joint. It can be seen in Figure 4.11 (b) that the maximum principal stress is generated near the top of the joint. This highlights the points most vulnerable to cracks.

A detailed assessment of both the test specimen and the FE model after the application of a week-long temperature profile indicated that no cracks were formed during early age. The experiments and simulations were, however, performed with a maximum temperature range of 17 °C (30 °F). While this temperature range (TS) captured normal diurnal temperature fluctuations, it was below the maximum ranges considered for design and analysis purposes.

To expand the scope of investigations to the temperature ranges beyond those tested in the laboratory, two additional temperature gradients were investigated. The temperature ranges of choice were 30 °C (86 °F), i.e., the highest temperature gradient recommended by AASHTO LRFD Bridge Design Specifications (TE-1) and 40 °C (104 °F), i.e., the highest temperature gradient reported from the field bridge weather monitoring data (TE-2) (White 2017)).

To introduce the initial temperature and boundary conditions, it was assumed that the temperature at the top surface of the specimen follows a sinusoidal function, i.e., $T = A\sin(2\pi t/24) + B$, where t is in hour ($0 \leq t \leq 24$) and A and B are the constants that form the temperature profile, as shown in Figure 4.12. The material properties and simulation steps were assigned similar to those used for the validated model. Figure 4.13 shows the predicted distribution of maximum principal stress at the interface of the joint and the adjacent box beam at the mid-span. It can be seen in this figure that as the level of thermal gradient increased from 17 °C to 40 °C, the corresponding maximum stress was consistently increased from 0.67 MPa to 0.9 MPa. The maximum values recorded from the three investigated temperature gradients (i.e., TS, TE-1 and TE-2) were near the top and the mid-depth of the joint, which is known to be the initiation point of concrete cracks in many of practical applications. The developed joint, however, remained crack free even under the most extreme temperature ranges. This highlights the great potential of the joint materials and details to be adopted for box-beam (and other similar) bridges. To further understand the effect of shrinkage-compensating behavior for longitudinal joint, another set of simulations was developed with the same test setup subjected to the TE-2 temperature profile with a longitudinal joint made with conventional concrete, including the shrinkage effect. Figure 4.14 presents the comparison of predicted distribution of maximum principal stress between joint made with shrinkage-compensating concrete and

normal concrete at the interface of the mid-span. The outcome of this investigation indicated that the maximum principal stress in conventional concrete can be more than 15% than that in shrinkage-compensating cement concrete, highlighting an increased vulnerability of the joint to shrinkage-induced cracks if a conventional concrete is used.

As concrete pour activities are commonly scheduled for the time periods that the temperature is sufficiently above the freezing temperature, the applied temperature profiles can reflect realistic exposure conditions. Even in the situations that the bridge is exposed to direct sunlight, although the top surface can accumulate warmth and cool down fast in the evening, the top surface temperature cannot go below the ambient temperature, to which the bottom surface has already been exposed to. This, as a matter of fact, has been the basis for the temperature profiles recommended by the AASHTO LRFD Bridge Design Specifications. Despite all the aspects mentioned in the previous paragraph, which can confirm the overall suitability of the temperature profiles applied to the test setup and FE models, to further understand the effect of the temperature profile, a new set of simulations were performed, in which the temperature at the top surface of the test setup is constantly lower than the temperature at the bottom surface. To make direct comparisons possible, the TE-2 Scenario (shown in Figure 4.12) is mirrored to the negative range. This means that the temperature difference between the top and bottom surface changes from + 40º C to - 40º C). The outcome of simulations indicates that although the profile of the maximum principal stress changes through the depth, as shown in Figure 4.15, the TE-2 Scenario still poses the highest risk of crack formation.

4.7 Conclusions

In this study, a full-scale setup consisting of two box beams connected with concrete made with Type K shrinkage-compensating cement was designed, constructed, and tested to evaluate its structural response under early-age temperature and shrinkage effects. The data collected from the experimental tests included temperature, longitudinal and transverse strain, and deflection in the joint and individual box beams under seven cycles of thermal loads. Furthermore, after the validation of a representative 3D FE model, additional simulations were performed to further understand the behavior of such longitudinal joints under service and extreme temperature gradient scenarios. The following observations and conclusions were made:

1. After seven cycles of thermal loads, no cracks were found at the interfaces of the joint and adjacent box beams. According to the strain data collected from the top surface of the box beams, both transverse and longitudinal strain changes were consistent with the temperature profiles with no unexpected trends.
2. Based on the test results, it was determined that the test setup maintains its full integrity under daily temperature fluctuations, taking into consideration the early-age expansion of Type K shrinkage-compensating cement concrete.
3. According to the data recorded at the joint interface, it was found that the transverse stress remains below the bond strength. This indicated that the joint effectively contributes to the overall structural response of the box-beam setup.
4. From the heat transfer analyses performed by the FE models, it was reported that temperatures obtained from the simulations at different depths are very much consistent with those recorded during the experiments.

5. Using thermal-stress analyses, various structural response measures, such as longitudinal and transverse strains, as well as deflections, were extracted from the FE simulations. Further to the validation of the FE models, it was confirmed that the test setup remains free of early-age cracks under the thermal load profiles, replicating those applied during the experiments.
6. From the principal stress distributions obtained for the joint, it was found that the maximum transverse strain in the joint was similar to that recorded by the embedded sensors. Correspondingly, the maximum transverse stress predicted from the FE analyses was 0.7 MPa (101.5 psi) on the top surface of joint, which remained below the cracking strength of concrete. This further supported that observation regarding the satisfactory performance of the bond between the joint and adjacent box beams.
7. The structural behavior of the joint setup was investigated under two extreme temperature gradients of 30 °C (86 °F) and 40 °C (104 °F) through the FE analyses. In particular, no damage was found throughout the thermal-stress analyses. This highlights the potential of the developed joint materials and details for application in various climate conditions.
8. Based on the behavior observed here in this study, while the shrinkage-compensating concrete joint was found to have a promising early-age performance for adjacent box beam bridge, the final judgement concerning applicability of proposed joint design should also combine the analysis of live loads effect, which will be concluded in author's another paper.

4.8 Acknowledgement

The authors would like to acknowledge the Iowa Department of Transportation for sponsoring this project. The contents of the paper reflect the conclusions and opinions of the authors and do not necessarily express the views of the funding agency.

4.9 References

AASHTO. (2016). “LRFD Bridge Design Specifications, 6th Ed.” Washington, DC.

ACI Committee 318. (2014). “Building Code Requirements for Structural Concrete (ACI 318-14).” Farmington Hills, MI: American Concrete Institute, 2014.

ACI Report 209.2R-08: Guide for Modeling and Calculating Shrinkage and Creep in Hardened Concrete, ACI, 2008.

Huckelbridge, Arthur A. and El-Esnawi, H. H. (1997). “Evaluation of Improved Shear Key Designs for Multi-Beam Box Girder Bridges (Report NO. FHWA/OH-97/009).” Cleveland, Ohio: Case Western Reserve University, 1997.

ASTM C157. (2016). “Standard Test Method for Length Change of Hardened Hydraulic-Cement Mortar and.” Annual Book of ASTM Standards, 08(c), 1–7.

Attanayake, U. and Aktan, H. (2008). “Issues with Reflective Deck Cracks in Side-by-Side Box Beam Bridge.” 2008 Concrete Bridge Conference, 1, 1–18.

Attanayake, U., Ulku, E., and Aktan, H. M. (2010). “Rationally Designed Staged Posttension Abates Reflective Cracking on Side-by-Side Box- Beam Bridge Decks.” Transportation Research Board 89th Annual Meeting, 1–15.

Battaglia, I. (2012). “Experimental Use of Type K Cement Concrete in Wisconsin Highway Bridge Decks (Report NO.: FEP-04-12).” Madison, WI: Wisconsin DOT, 2012.

Bischaff, D., Toepel, A. (2004). “Laboratory Testing of Portland Cement Concrete Patch Material Modified to Reduce or Eliminate Shrinkage.” Madison, WI: Wisconsin DOT, 32-33

CTS Cement Manufacturing Corp. Komponent Datasheet. 2019.

Dayton. (2016). Perform with PrecisionTM. Retrieved from http://www.daytonsuperior.com/

FIB: Structural Concrete (1999). Textbook on Behavior, Design and Performance, Updated Knowledge of the CEB/FIP Model Code 1990, FIB Volume 3, July 1999.

Folliard, K., Smith, C., and Sellers, G. (2003). “Evaluation of Alternative Materials to Control Drying-Shrinkage Cracking in Concrete Bridge Decks.” 7.

Giraldo-londoño, O. (2014). “Finite Element Modeling of the Load Transfer Mechanism in Adjacent Prestressed Concrete Box-Beams.”

Grace, N. F., Jensen, E. A., and Bebawy, M. R. (2012). “Transverse post-tensioning arrangement for side-by-side box-beam bridges.” PCI Journal, 48–63.

Gruner, P. W., and Plain, G. A. (1997). “Type K Shrinkage-Compensating Cement in Bridge Deck Concrete.” Concrete International.

Han, J., Jia, D., and Yan, P. (2016). “Understanding the shrinkage compensating ability of type K expansive agent in concrete.” Construction and Building Materials, Elsevier Ltd, 116, 36–44.

Hassan, K. E., Cabrera, J. G., and Maliehe, R. S. (2000). “Effect of mineral admixtures on the properties of high-performance concrete.” Cement and Concrete Composites, 22(4), 267–271.

Hognestad, E. (1951). A Study of Combined Bending and Axial Load in Reinforced Concrete Members.

Huckelbridge Jr., Arthur A., El-Esnawi, H., and Moses, F. (1995). “Shear Key Performance in Multibeam Box Girder Bridges.” Journal of Performance of Constructed Facilities, 9(4), 271–285.

Kianoush, M. R., Acarcan, M., and Ziari, A. (2008). “Behavior of base restrained reinforced concrete walls under volumetric change.” Engineering Structures, 30(6), 1526–1534.

Lei, X., Yao, Y., Cao, S., and Guo, Z. G. (2015). “Research in Destruction of Concrete Bridge Expanded Joint Influenced by Temperature Difference.” Applied Mechanics and Materials, 744–746, 803–806.

Liu, Zhengyu, "Evaluation of an innovative joint design for the adjacent box beam bridges" (2018). Graduate Theses and Dissertations, 50–65.

Miller, R. A. (1999). “Ful Scale Testing of Shear Keys for Adjacent Box Girder.” PCI Journal.

Nair, H., Ozyildirim, C., and Sprinkel, M. M. (2016). “Evaluation of Bridge Deck with Shrinkage- Compensating Concrete.”

Ogawa, K. (1982). “C4A3S Hydration, Ettringite Formation, and Its Expansion Mechanism: II. Microstructural Observation of Expansion.” Cement and Concrete Research. Vol. 12, 101-109, 1982.

Precast/Prestressed Concrete Institute. (2015). PCI Bridge Design Manual, Chicago.

Péra, J., and Ambroise, J. (2004). “New applications of calcium sulfoaluminate cement.” Cement and Concrete Research, 34(4), 671–676.

Rahman, M., Chen, Y., Lindquist, W., Ibrahim, A., and Hindi, R. (2018). “Mitigation of Shrinkage Cracking in Bridge Decks Using Type-K Cement Mohammad.” (NBI 2006), 133–144.

Richards, T. (2013). “Solving Contact Problems with ABAQUS.” (March).

Hussein, Husam H., Walsh, Kenneth K., Sargand, Shad M., AI Rikabi, Fouad T., Steinberg, Eric P. (2017a). “Modeling the Shear Connection in Adjacent Box-Beam Bridges with Ultrahigh-Performance Concrete Joints. I : Model Calibration and Validation.” Journal of Bridge Engineering, 22(8), 1–14.

Sargand, Shad M., Walsh, Kenneth K., Hussein, Husam H., AI Rikabi, Fouad T., Steinberg, Eric P. (2017b). “Modeling the Shear Connection in Adjacent Box-Beam Bridges with Ultrahigh-Performance Concrete Joints. II : Load Transfer Mechanism.” 22(8), 1–11.

Russell, H. G. (2009). Synthesis 393 Adjacent Precast Concrete Box Beam Bridges: Connection Details.

Sandberg, J. P., and Liberman, S. (2007). “Monitoring and Evaluation of Cement Hydration by Semi-Adiabatic Field Calorimetry.” ACI Publications, 241, 13–24.

Semendary, A. A., Asce, S. M., Walsh, K. K., Ph, D., Asce, A. M., Steinberg, E. P., Ph, D., and Asce, M. (2017). “Early-Age Behavior of an Adjacent Prestressed Concrete Box-Beam Bridge Containing UHPC Shear Keys with Transverse Dowels.” 22(5), 1–14.

Simulia. (2014). ABAQUS 6.14.

Steinberg, E., Miller, R., Nims, D., Sargand, S., (2011). “Structural Evaluation of LIC-310-0396 and FAY-35-17-6. 82 Box Beams with Advanced Strand Deterioration.”

White, L., Ryan, K., and Buckle I. (2017), “Thermal Gradients in Southwestern United States and the Effect on Bridge Bearing Loads.” (May)

Xi, Y., Shing, B., Abu-Hejleh, N., Asiz, A., Suwito, A., Xie, Z., and Ababneh, A. (2003). “Assessment of the Cracking Problem in Newly Constructed Bridge Decks in Colorado.” Colorado Department of Transportation, (March).

Yuan, J. and Graybeal, B. (2014). “Adjacent box beam connections.” PCI National Bridge Conference, Precast/prestressed Concrete Insitute, Chicago, 1–28.

Yuan, J. and Graybeal, B. (2016). “Full-Scale Testing of Shear Key Details for Precast Concrete.” Journal of Bridge Engineering.

Table 4.1. Mixture proportions design for box beam and joint

Component	Box Beams (lbs/cy [kg/m^3])	Longitudinal joint (lbs/cy [kg/m^3])
Portland cement	474 (281)	403 (239)
Type K cement	0 (0)	71 (42)
Fine aggregate	1500 (890)	1500 (890)
Coarse aggregate	1517 (900)	1517 (900)
Water	255 (151)	255 (151)
Fly ash	119 (71)	119 (71)

Table 4.2. Summary of material properties used in the FE model.

Properties	Box Beams	Joint	Reinforcement
28-day Compressive Strength (MPa)	34.5-44.8	34.5	413.7
Density (kg/m^3)	2400	2400	8050
Young's Modulus (MPa)	29000	29000	200000
Poisson's Ratio	0.2	0.2	0.3
Heat Conductivity (W/m·K)	2.1	2.1	50
Coefficient of Thermal Expansion (/°C)	10×10^{-6}	10×10^{-6}	12.2×10^{-6}
Specific Heat (J/kg·K)	900	900	490

Table 4.3. Comparisons of transverse strains on the top surface of the mid-span of the test setup.

Time	Strain near the joint (με)			Strain at the box beam (με)		
	Experiment	FE Model	Difference (%)	Experiment	FE Model	Difference (%)
1st day	104	90	-13.5%	110	106	-3.6%
2nd day	83	72	-13.3%	109	87	-20.2%
3rd day	83	91	+9.6%	109	96	-11.9%
4th day	84	88	+4.8%	108	75	-30.6%
5th day	79	90	13.9%	99	101	+2.0%
6th day	82	92	12.2%	98	103	+5.1%

Table 4.4. Comparisons of longitudinal strains on the top surface of the mid-span of the test setup.

Date (days)	Longitudinal Strain (με)		
	Experiment	FE Model	Difference (%)
1st day	89	82	-7.9%
2nd day	89	87	-2.2%
3rd day	89	76	-14.6%
4th day	86	94	+9.3%
5th day	79	85	+7.6%
6th day	82	87	+6.1%

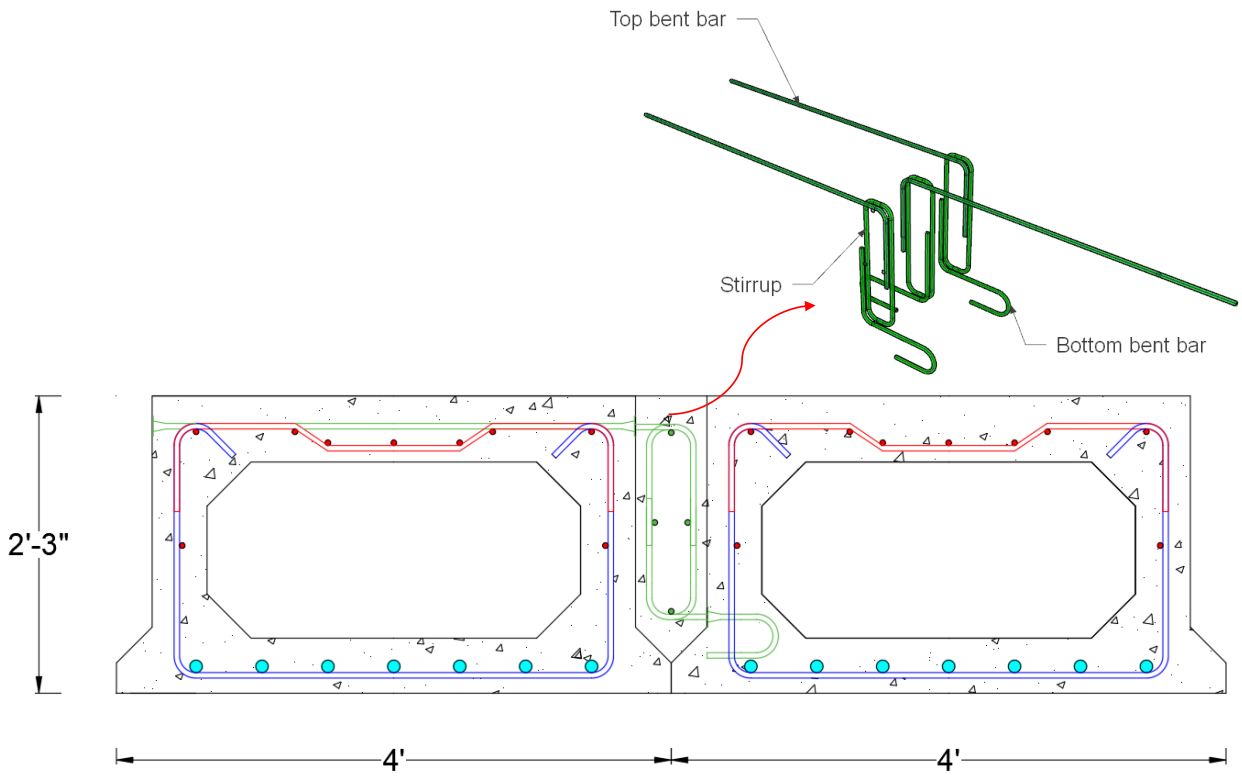

Figure 4.1. Design details of the experimental test setup, including the longitudinal joint and two adjacent box beams (1 in. = 2.54 cm).

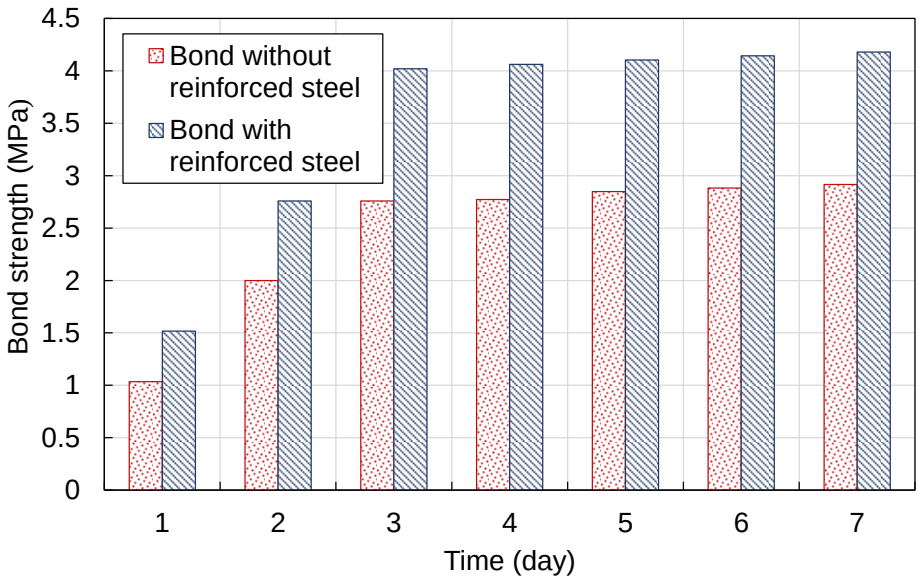

Figure 4.2. Time dependent bond strength between shrinkage compensating cement concrete and normal concrete (Liu, 2018).

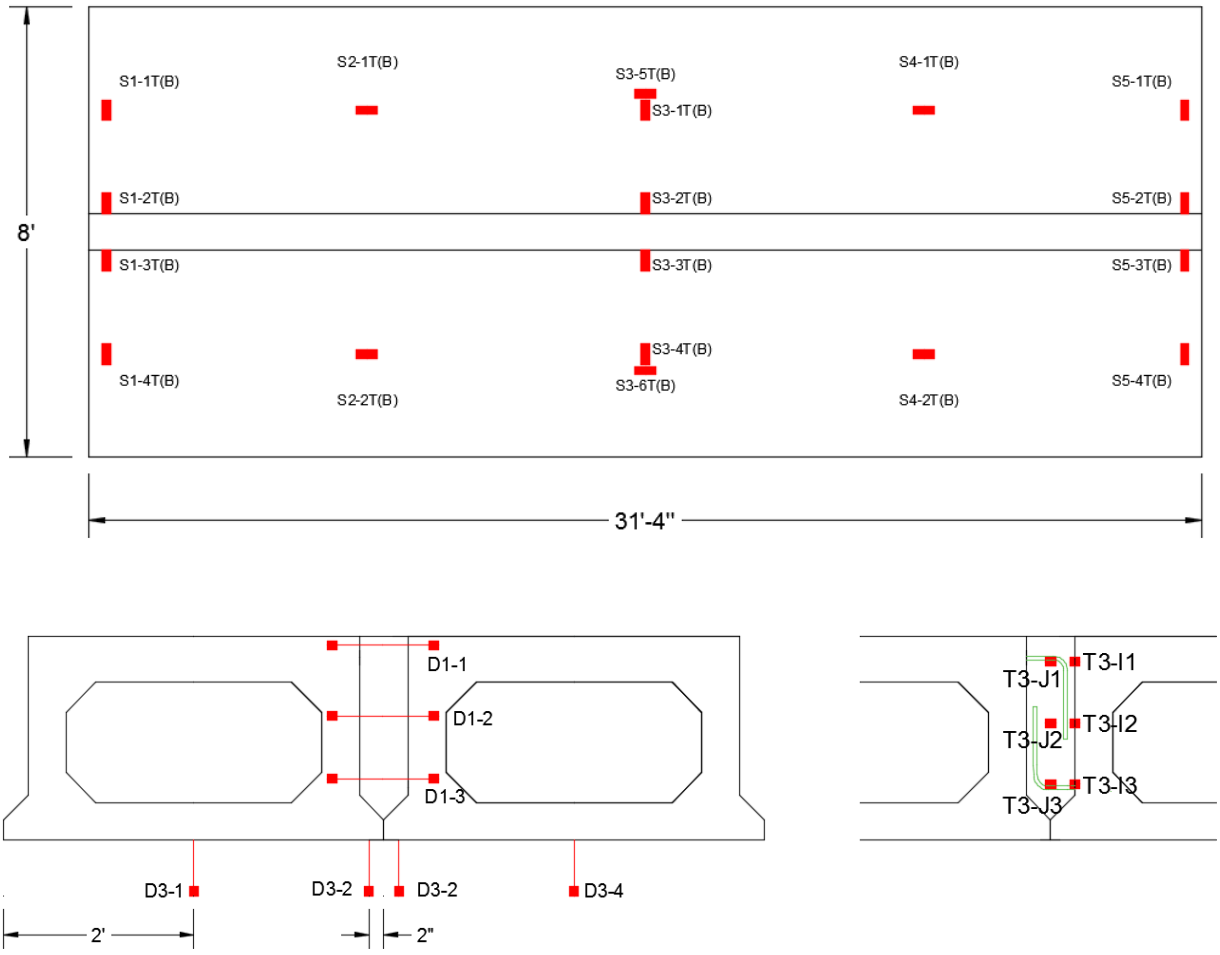

Figure 4.3. Instrumentation layout, which includes vibrating wire strain gauges (labeled with S), deflection transducers (labeled with D), and thermocouples (labeled with I and J).

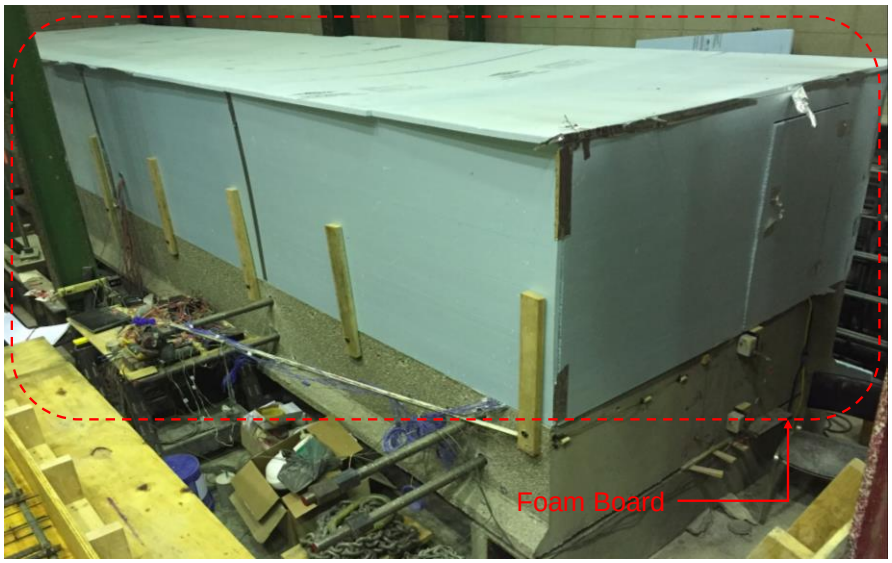

(a)

(b)

Figure 4.4. Details of the test setup to provide a controlled temperature profile during the first seven days after construction: (a) insulated box built on the top surface and (b) inside the insulated box.

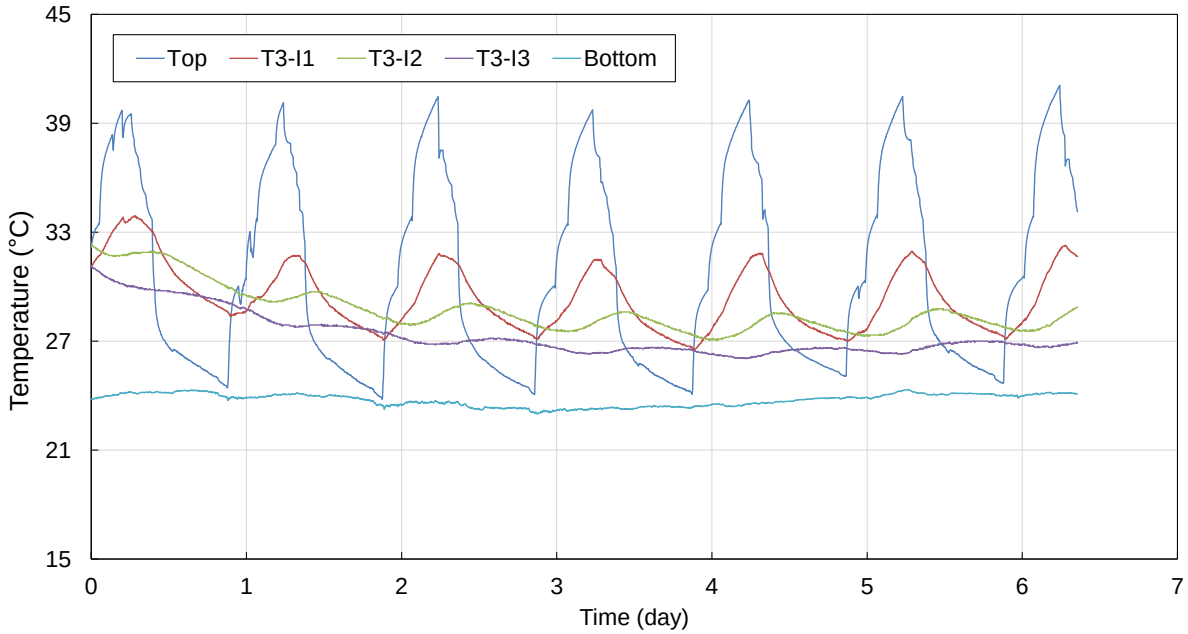

Figure 4.5. Temperature profiles recorded on the top and bottom surface, as well as various depths inside the joint, during the seven-day testing period.

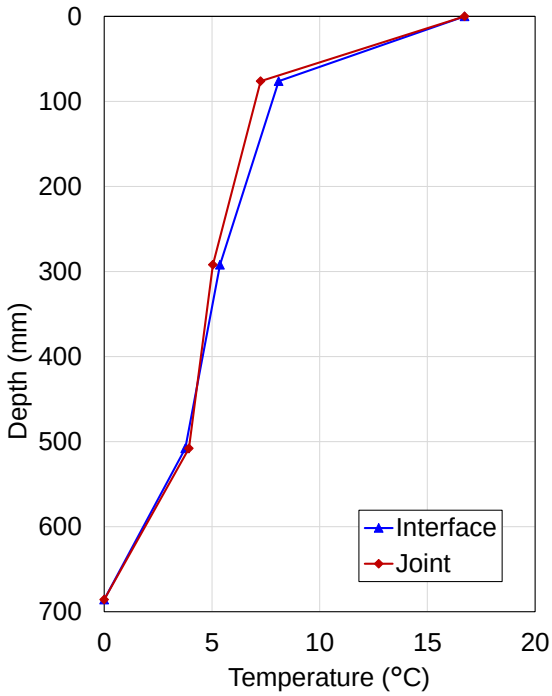

Figure 4.6. Temperature variation in the transverse direction from the center of the joint to the interface.

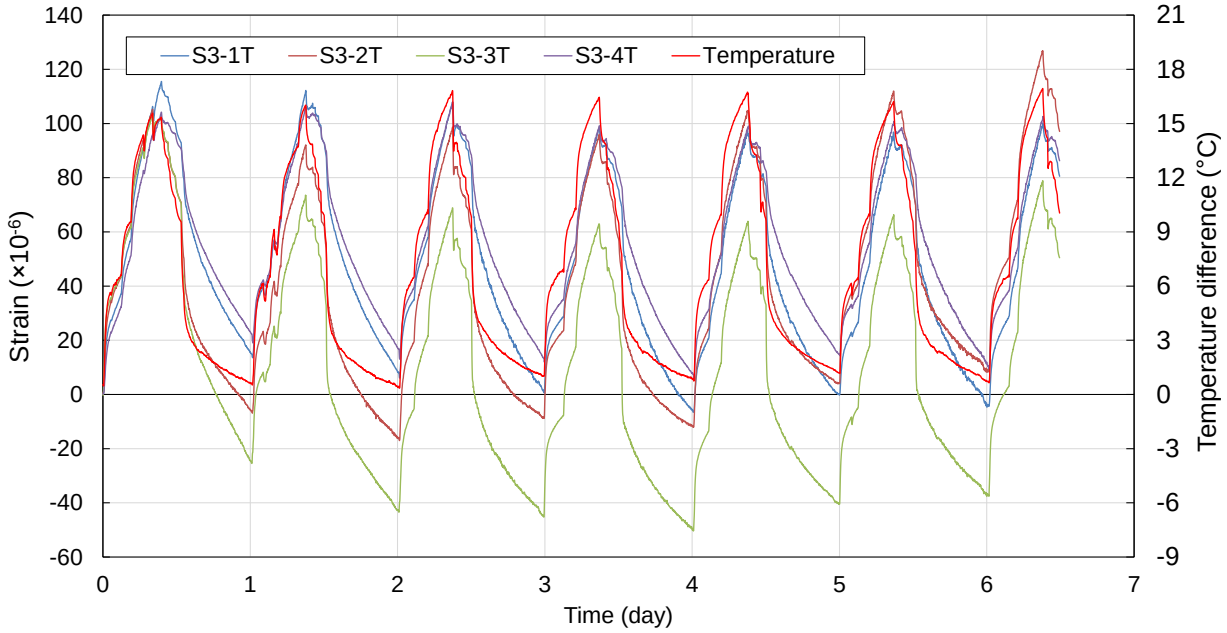

(a)

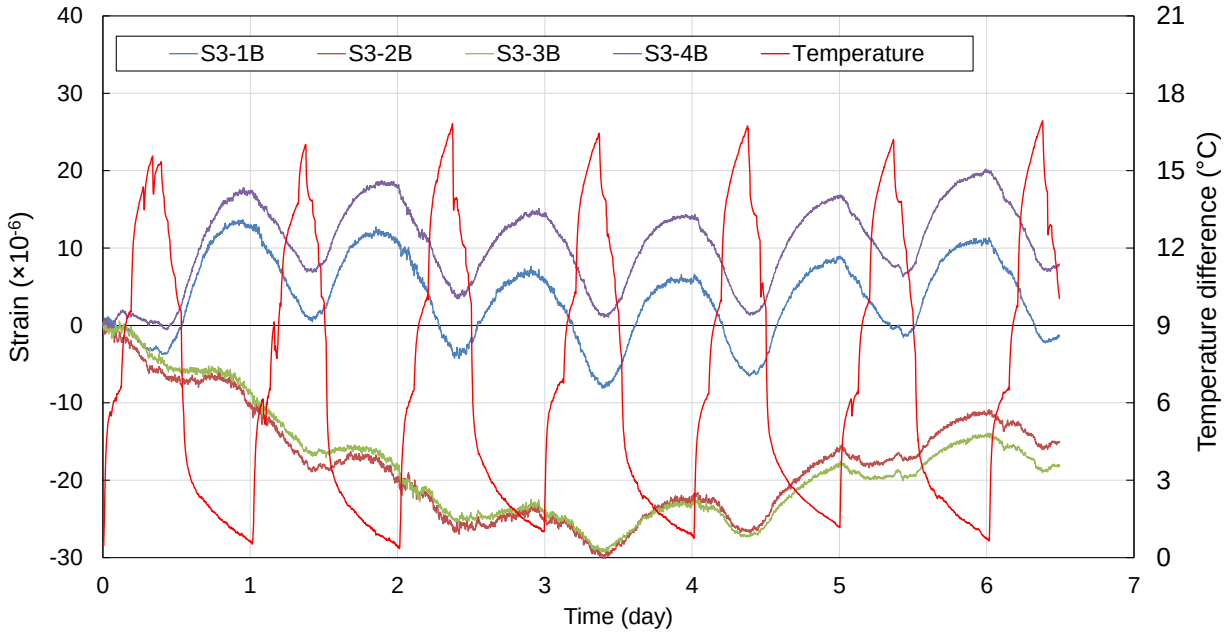

(b)

Figure 4.7. Transverse strain and temperature profiles at the mid-span recorded on (a) top and (b) bottom surface.

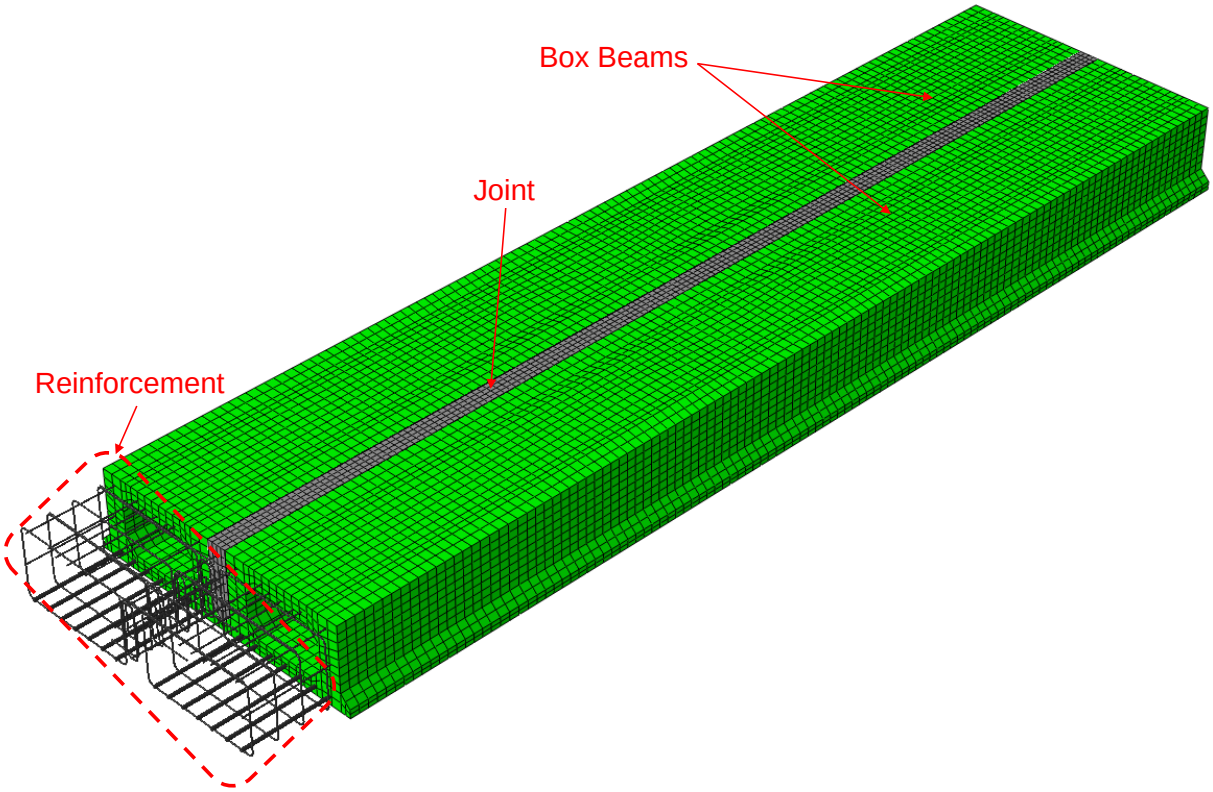

Figure 4.8. Details of the FE model generated for numerical simulations.

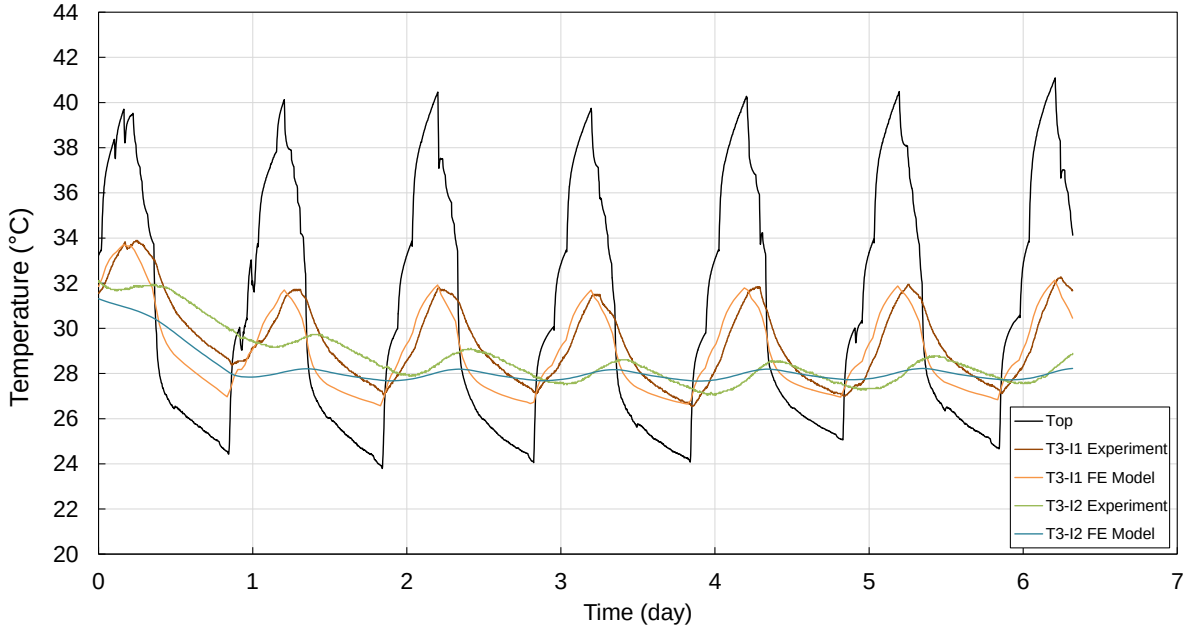

Figure 4.9. Comparison of temperature profiles obtained from the FE model and measured during the full-scale test.

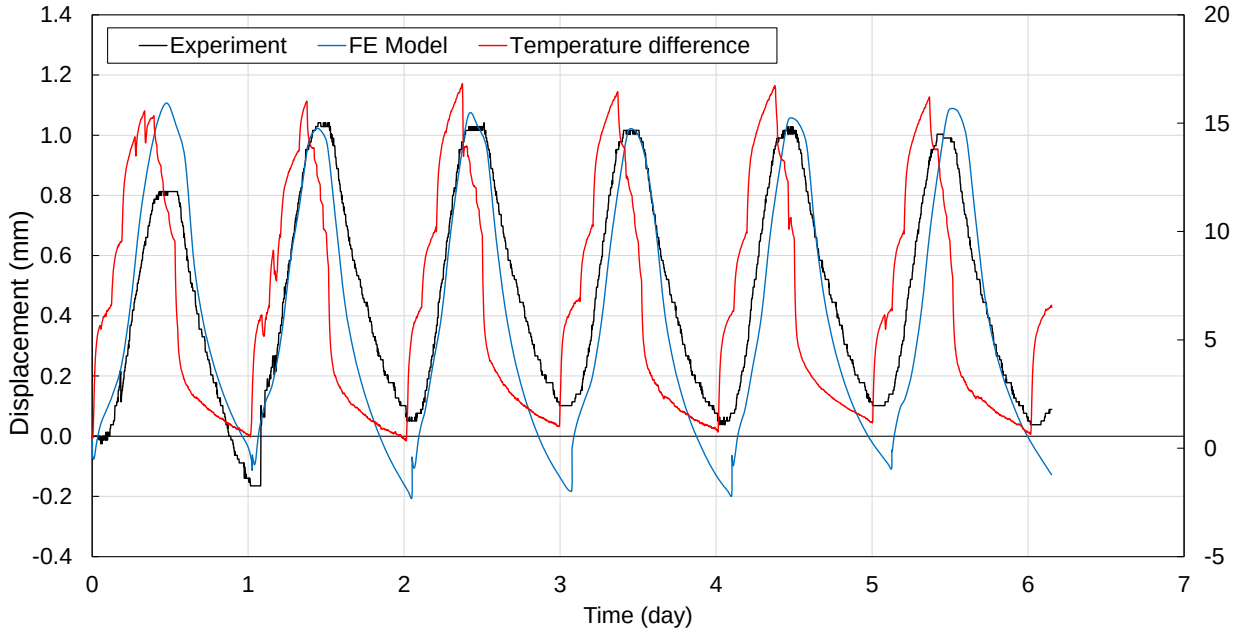

Figure 4.10. Comparison of mid-span deflections obtained from the FE model and measured during the full-scale test.

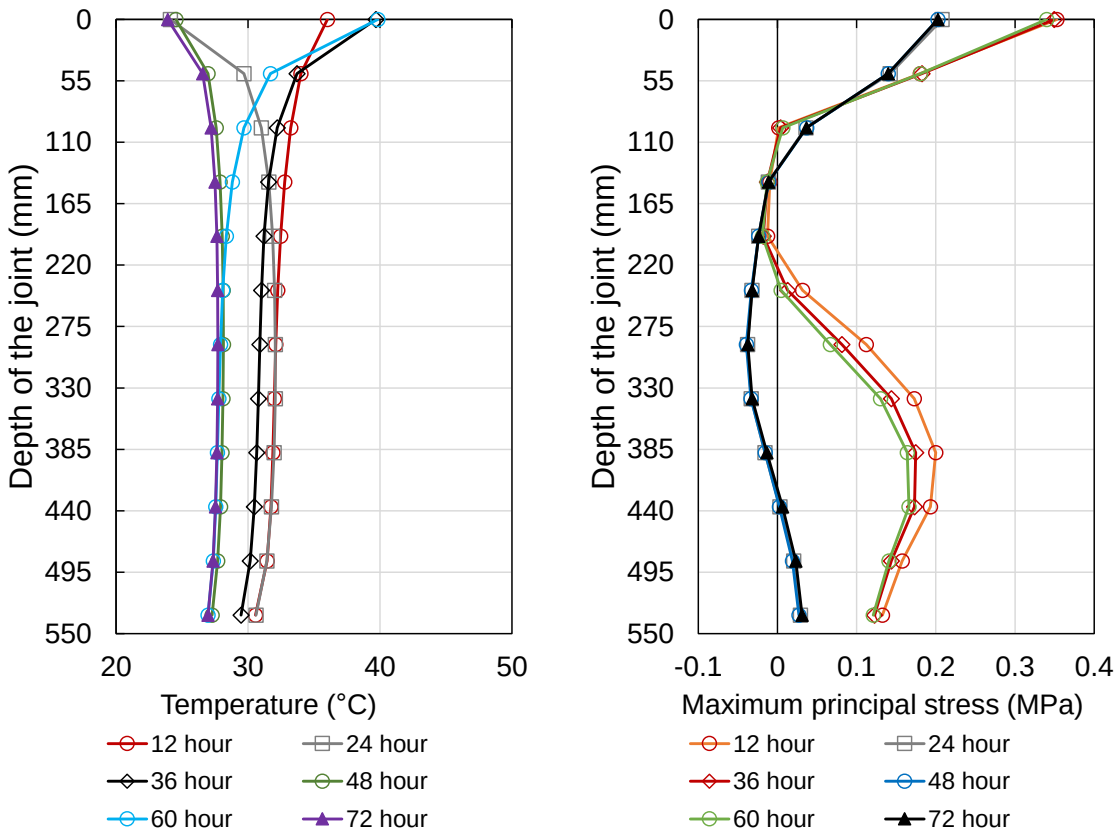

(a) (b)

Figure 4.11. Evolution of (a) temperature and (b) maximum principal stress over time at the interface of the joint with the box beam.

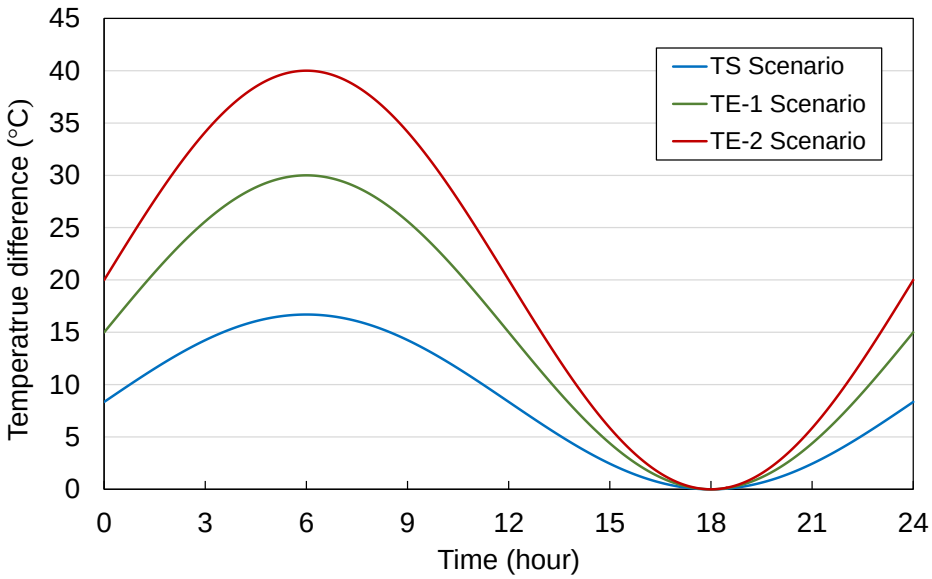

Figure 4.12. Three temperature ranges applied to the FE model to capture service and extreme exposure conditions.

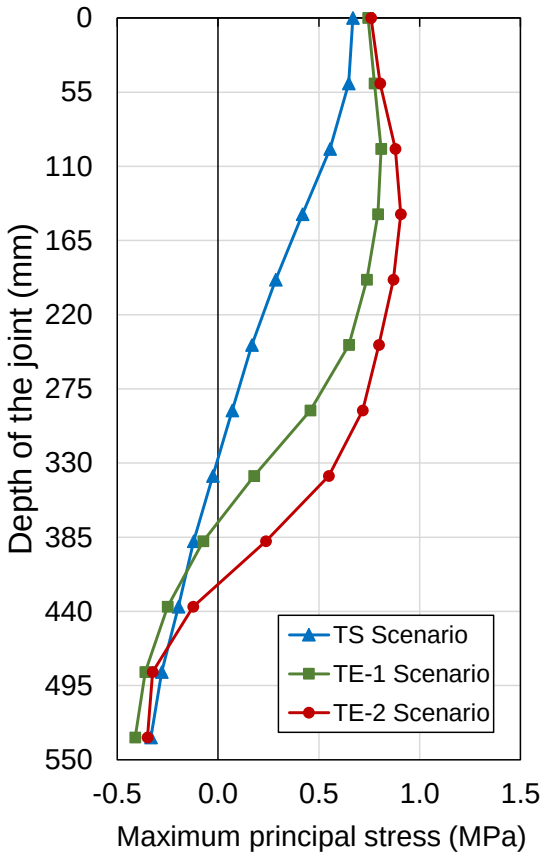

Figure 4.13. Distribution of maximum principal stress along the depth at the interface of the joint with the box beam subjected to three different temperature gradients.

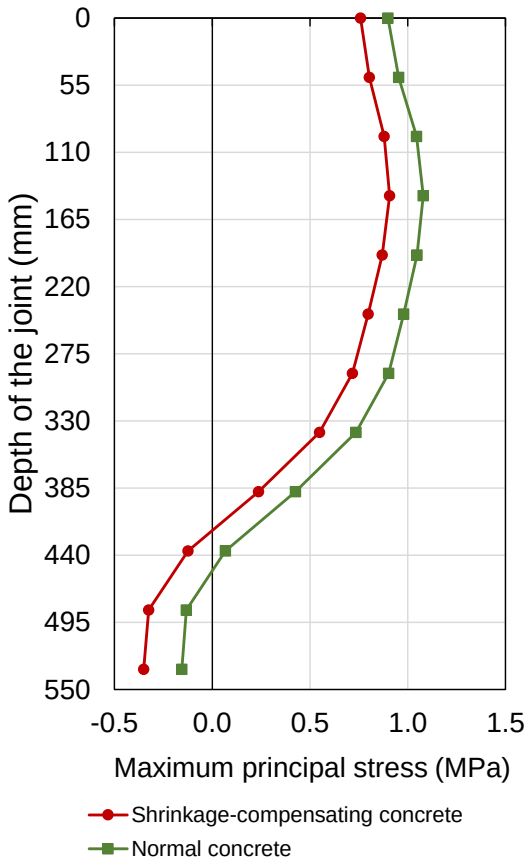

Figure 4.14. Distribution of maximum principal stress at the interface of the joint for the box beam subjected to TE-2 temperature profile.

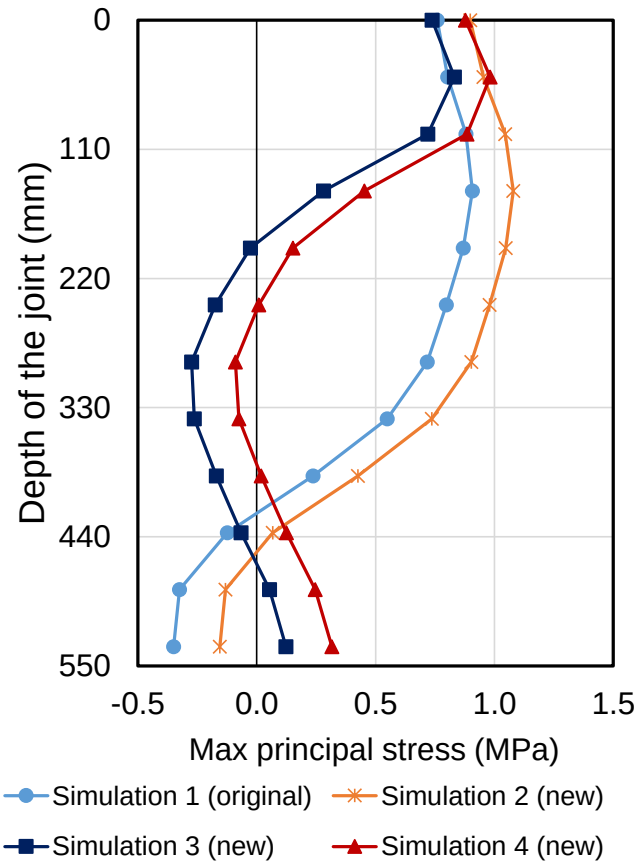

Simulation Case	Joint Material	Temperature Profile
1 (original)	Shrinkage-compensating cement concrete	+ 40º C
2 (new)	Normal concrete	+ 40º C
3 (new)	Shrinkage-compensating cement concrete	- 40º C
4 (new)	Normal concrete	- 40º C

Figure 4.15. Maximum principal stress at the interface for the joint subjected to equal but opposite temperature gradients applied to the top and bottom surfaces.

CHAPTER 5. INVESTIGATION OF LONGITUDINAL BRIDGE JOINTS MADE WITH SHRINKAGE-COMPENSATING CEMENT CONCRETE UNDER MONOTONIC AND CYCLIC LOADS

5.1 Abstract

Longitudinal joints used for connecting adjacent box beams in bridge superstructures are prone to the formation and propagation of cracks, which can cause structural performance issues, further to durability concerns. Among possible solutions, a combination of shrinkage-compensating cement concrete along with joint reinforcement has been investigated in the current study through full-scale experimental tests and supporting numerical simulations. The shrinkage-compensating cement concrete offered the capability of producing controlled compressive stresses during the early stage of hydration, counteracting detrimental tensile stresses that originate from the shrinkage of concrete. Longitudinal and transverse reinforcements were also included in the joint to ensure the proper transfer of forces between adjacent box beams. The structural response of the full setup was evaluated under five million cycles of loading with different loading protocols and boundary conditions. The data collected from the experimental tests consisted of longitudinal and transverse strains, as well as deflections. To expand the scope of this investigation and understand the effect of interfacial bond strength and joint reinforcement, a set of numerical simulations were also performed. Through a new combination of concrete mixture and reinforcement detail, the outcome of this study provided a holistic solution to address the long-standing issue of degradation of longitudinal joints in box-beam bridges.

Keywords: Structural Performance Assessment; Box-Beam Bridges; Longitudinal Joints; Shrinkage-Compensating Cement Concrete; Reinforcement Detail.

5.2 Introduction

Precast concrete box beams are the primary choice for short to medium span bridges in the United States, especially for bridges serving secondary roads. Owing to their relatively shallow superstructure depth, ease of construction, and simple aesthetic attributes, box-beam bridges have been adopted by several Departments of Transportation. This type of bridge is constructed by placing a set of box beams next to each other, casting their longitudinal joints, and applying transverse posttensioning forces (Russell 2009). Despite the overall promise of this structural system, the longitudinal joints are known to be susceptible to cracks, exposing the main box beams to water and deleterious agents. Such an exposure, over time, can lead to the corrosion of embedded rebars and posttensioning ties, which not only reduces the structural capacity, but also leads to excessive differential deflections between the adjacent beams. To address possible performance issues, a number of experimental tests and numerical studies have been conducted on longitudinal joints (Gulyas 1995; Miller 1999; Attanayake and Aktan 2008a; b; Kim and Sang 2010; Russell 2011; Hanna and Morcous 2011; Grace et al. 2012; Giraldo-londoño and Giraldo-londoño 2014; Yuan and Graybeal 2014, 2016; Rikabi et al. 2017). In most cases, cracking of longitudinal joints has been found to be initiated as a result of stresses induced due to the shrinkage of joint materials and seasonal temperature variations, further to live load effects (Miller 1999; Sharpe 2007; Steinberg et al. 2011; Russell 2011; Lei et al. 2015;). In the past two decades, the most commonly used material for the longitudinal joint was non-shrinkage or cast-in-place concrete. Among the studies performed on longitudinal joint materials, Gulyas et al. (1995) conducted a series of experimental tests on the joints made with the cementitious materials that had non-shrinkage properties and magnesium ammonium phosphate mortars. It was reported that the bond strength and composite section properties are the key contributing factors. Issa et al. (2003) performed

vertical shear, direct tension, and flexural tests on a total of 36 specimens using four different grout materials. It was concluded that, even though polymer concrete can be a competitive choice for joints, in terms of strength, bond, and mode of failure, conventional grout can offer the flexibility and convenience of application. Although promising results were obtained in the cited study for longitudinal joints made with grouts, it was stated that a joint material with a thermal expansion coefficient similar to concrete could be an ideal alternative to eliminate the concerns associated with environmental stressors. This can be further supported by the field study conducted by Hlavacs et al. (1997). Based on the data collected from the sensors embedded in the beams and their longitudinal joints, Hlavacs et al. (1997) found significant discontinuities in strains, especially when the bridge under consideration experienced freezing temperatures. In a separate effort, Attanayake and Aktan (2008b) provided observations from monitoring a then newly-constructed box-beam bridge. Longitudinal cracks were found to emerge along the joint interface within only two to three days after grouting the joint.

Further to material properties, joint configuration details directly affect the structural response of box-beam bridges (Giraldo-londoño 2014). Among the relevant studies, Dong et al. (2007) established a set of finite-element (FE) models to investigate the effect of joint rigidity. This was achieved by applying the forces obtained from a full bridge model to the joint setups with full and partial depth. Although the simulations were performed with an assumption of elastic behavior, it was demonstrated how the load transfer mechanism can be influenced with the joint geometry. In particular, it was found that the maximum principal stresses generated in the partial-depth joints were significantly higher than those generated in the full-depth joints. A grillage analysis with similar objectives was conducted by Sang (2010). Considering various configurations, a full-depth joint was recommended, especially to

minimize cracks in longitudinal joints. From a design perspective, live load effect is the primary factor governing the structural configuration of box-beam bridges with longitudinal joints. When a truck passes a box-beam bridge with a set of wheels placed on one of the box beams, a large differential deflection is expected if the longitudinal joint is not properly designed (or if it is damaged). Under such circumstances, moment and shear transfer mechanisms can be significantly disrupted as well. To reduce differential deflections and also counteract the transverse tensile stresses induced in the longitudinal joints, transverse posttensioning is widely used in box-beam bridges. Grace et al. (2012) conducted a study on the performance of box-beam bridges posttensioned in the transverse direction. Despite advantages, non-uniform transverse stresses were found on the sides of the box beams, mainly due to the localized effect of the transverse posttensioning forces. In addition, from six field tests conducted by Huckelbridge et al. (1997) on a box-beam bridge, it was found that, despite the presence of the posttensioned ties, the issue of interface cracks in longitudinal joints was not resolved. This led to the question of whether or not transverse posttensioning has enough contribution to the structural system of box-beam bridges to justify the cost and effort associated with it. This was consistent with the findings reported by Yuan and Graybeal (2016).

In the most recent efforts, the Federal Highway Administration (FHWA) developed a joint design for box-beam bridges using ultra-high performance concrete (UHPC). Yuan and Graybeal (2016) reported the results of full-scale experimental tests on a UHPC longitudinal joint between two box beams. With the main objective of evaluating the structural performance of both partial- and full-depth joints in adjacent box beams, a cyclic load setup was used. The outcome of the tests indicated that cyclic loading did not initiate cracks in the UHPC joint, contrary to the joint with a conventional grout, which suffered from cracks, despite the

presence of transverse posttensioning forces. In a separate study, Semendary et al. (2017) investigated the early-age behavior of UHPC longitudinal joints for an adjacent box beam setup. The data collected during the first week after construction showed that the joint performed well with no interfacial cracks. Despite the promising results obtained with using UHPC in the longitudinal joints of box-beam bridges, there are practical obstacles with regard to the cost and expertise needed for UHPC, which can hinder an immediate implementation of UHPC longitudinal joints. This motivated the current study to explore alternative joint materials and configuration details that not only offer satisfactory structural performance, but also meet budget constraints.

Considering that one of the leading causes of cracking in the longitudinal joints of box-beam bridges is early-age shrinkage and temperature effects, the joint developed in the current study utilizes shrinkage-compensating cement, also known as Type K cement, as a partial replacement of portland cement. Without requiring a significant additional cost, this type of cement offers shrinkage compensation and self-stressing characteristics with no adverse effects on the strength and other mechanical properties of the concrete mixture used in the joint (Ogawa 1982; Péra and Ambroise 2004). In addition, contrary to non-shrinkage grouts, concrete mixtures made with shrinkage-compensating cement provides a thermal expansion coefficient similar to that of the box beam concrete. This minimizes the likelihood of experiencing temperature-induced cracks, especially at early age. While the shrinkage-compensating cement was found to be promising for bridge deck applications (Barnes and Valentine 2002; Graves 2007; Sprinkel 2015), there was no study available in the literature on how this type of cement can be employed in the longitudinal joints of box-beam bridges. To address this research gap, a holistic set of material and structural tests were performed in the

current study on a full-depth longitudinal joint setup made with shrinkage-compensating cement concrete and the reinforcement details that eliminate the need to transverse posttensioning ties. The test plan started with four small-scale specimens designed to investigate different transverse reinforcement size and spacing. The specimens were evaluated for early-age behavior and then tested for ultimate capacity after seven days. Based on the shrinkage, temperature, and strain data reported by Liu and Phares (2019), it was inferred that the longitudinal joint made with shrinkage-compensating cement concrete has the potential to offer superior performance with no cracks. This led to the full-scale testing program outlined in the following sections.

To achieve a holistic evaluation of the developed joint setup, two full-scale box beams were built in the laboratory and connected with a joint made with shrinkage-compensating cement concrete. The first set of tests were focused on the early-age performance of the full-scale setup, examining a range of contributing factors, such as heat of hydration, shrinkage effect, and ambient thermal load. For this purpose, an insulation box was placed on the top surface of the test setup and a temperature profile was applied in seven cycles of heating and cooling, replicating the ambient temperature that a box-beam bridge is exposed to during the first week after construction. As reported in Shi et al. (2019), no cracks or performance issues were observed at the joint or adjacent box beams after seven cycles of thermal load. Upon obtaining satisfactory results from the early-age tests, the second set of tests began to understand the structural response of the developed joint under live loads. This critical aspect, which is the main focus of the current manuscript, was investigated by applying five million cycles of vertical load with different loading protocols and boundary conditions. The data collected from the experimental tests consisted of longitudinal and transverse strains, as well

as deflections. The measurements were primarily targeted to evaluate the joint performance and load transferability. In addition, a set of three-dimensional FE models were created to further understand the structural performance of the longitudinal joints developed in the current study subjected to live load effects. Upon calibrating the FE models, simulations were performed with the objective of evaluating a series of influential parameters related to reinforcement details in the longitudinal joint and how the joint interacts with the main box beams. The findings of this study are expected to provide an alternative selection of materials and details for the longitudinal joints of box-beam bridges with the ultimate goal of facilitating a safe, durable, and economic bridge construction.

5.3 Experimental Program

5.3.1 Specimen Fabrication

To evaluate the structural performance of the longitudinal joint between two adjacent box beams, a set of monotonic and cyclic loading tests were performed on a full-scale setup. The two box beams cast for the experimental test setup had a cross-section of 48 × 27 in. (121.9 × 68.6 cm) (width × depth) and a length of 31.2 ft. (9.5 m), following the Iowa Department of Transportation's 30 ft. Box Beam Standard. In the joint details developed for the current study, the adjacent box beams were connected with top and bottom hooked reinforcing bars extended from each side of the precast box beams into the connection and additionally tied with stirrups to form a closed loop. Four longitudinal reinforcing bars were also placed in the joint (and tied with the stirrups) to increase the flexural stiffness. A three-dimensional view of the reinforcement details included in the joint has been provided in Figure 5.1. As shown in this figure, the top and bottom bent bars are alternatively tied to the stirrups. This was to maintain both moment and shear transfer across the longitudinal joint. In addition, the reinforcement

was intended to control any potential cracks, further to improve the bond strength, as reported in Liu and Phares (2019).

A total of five diaphragms were placed at the midspan, two quarter-spans, and two ends of each box beam (Figure 5.2). Seven #9 (No. 29) Grade 60 steel bars were used as longitudinal reinforcement in each box beam. The closed shear stirrups inside the box beams comprised of #5 (No. 16) steel bars at the bottom and #4 (No. 13) steel bars at the top. The spacing between the stirrups was 8 in. (20 cm) in the two end quarter spans and 10 in. (25 cm) elsewhere. A conventional concrete mixture design with a 28-day strength of 4 ksi (28 MPa) was used for the box beams and longitudinal joint. In the longitudinal joint, 15% of portland cement was replaced with Type K shrinkage-compensating cement, following the instructions received from the cement manufacturer (CTS Cement Manufacturing Corp 2019). The specimen preparation steps are depicted in Figure 5.3. One significant shear force transfer mechanism between the joint and adjacent box beams is through bond strength, which originates from the roughness of the surfaces in contact. To achieve the highest bond strength, the vertical face of each box beam at the joint was sandblasted prior to casting the joint's concrete. Using a chemical retarder oiled on the formwork, it was ensured that an exposed aggregate surface is obtained. After the beam's concrete gained strength and the formwork was removed, the surface mortar was flushed off with a strong stream of water to achieve sandblasted concrete surfaces. Before casting the joint, the beam surfaces were prewetted for 20 minutes. This was to minimize moisture loss, as the room temperature was increased with the objective of simulating a noontime pouring in the field. In addition, a layer of burlap and plastic sheet were placed on the top surface of the joint immediately after casting. This layer was kept moisturized for seven days. Although the developed joint was designed to meet the performance

requirements without needing transverse posttensioning, a set of the transverse posttensioning ties were placed at the diaphragm locations. They, however, were tightened without applying any posttensioning forces.

5.3.2 Test Setup

Immediately after the specimen was cast, seven cycles of thermal load were applied to investigate early-age performance of the joint setup subjected to temperature and shrinkage effects. Upon completing the first set of tests, results of which provided in (Shi et al. 2019), the loading setup is shown in Figure 5.4 was created to evaluate the joint's performance under monotonic and cyclic loads. For this purpose, the loads were applied through a four-point bending setup, which included a spread beam attached to the MTS actuators. A 12 × 12 in. (30 × 30 cm) steel plate was used underneath each actuator to properly distribute the applied load. It should be noted that the two actuators were intentionally placed 6 in. (15 cm) off from the longitudinal centerline of each box beam in order to create torsional effects. Two boundary conditions were established and tested in this study, including a simply supported and a constrained setup. In the simply supported setup, the specimen was supported on neoprene bearing pads, replicating the actual field condition. A total of 3.4 million cycles of load were applied with this boundary condition. The setup was later converted to a constrained boundary condition to simulate a common situation in box-beam bridges, where one of the box beams experiences a significant loading demand because of the placement of the live load and the presence of adjacent beams. For achieving the second boundary condition, which magnifies the shear demand on the joint when subjected to cyclic loads, extra supports were placed underneath one of the box beams at quarter spans. Each extra support crossed the full width of the individual beam, as shown in Figure 5.5.

5.3.3 Loading Protocols and Instrumentation Layout

Cyclic loads were applied with a sinusoidal loading protocol provided in Figure 5.6. Under the simply supported boundary condition, the vertical loads were alternated in such a way that when one beam was under maximum load, the other beam was under minimum load. The minimum load was to ensure that one of the two beams is held down, while the other beam experienced maximum loading demand. Under the constrained boundary condition, however, a constant 5 kips (22 kN) load was applied to one of the two beams. The cyclic loading amplitudes began from 18 kips (80 kN) and then increased to 36 kips (160 kN) and 42 kips (186 kN). It should be noted that the maximum bending moment generated from the 18 kips (80 kN) load was equivalent to the moment caused by an HL-93 truck, according to AASHTO LRFD Bridge Design Specifications (2014). A total of 5 million cycles of load were applied at the three levels of loading amplitude, i.e., 18 kips (80 kN), 36 kips (160 kN), and 42 kips (186 kN). For each of the three amplitudes of load, the test was performed with one million cycles of load with a simply supported boundary condition. In the first 3 million cycles of load, a hand-tightened force was applied to the posttensioning ties. This force was then removed, and another 0.4 million cycles of load were applied at the highest loading amplitude, i.e., 42 kips (186 kN) without changing the boundary condition. The boundary condition was then converted to the constrained one and the remaining 1.6 million cycles of load were applied, consisting of 0.2 million cycles at 18 kips (80 kN), 0.4 million cycles at 36 kips (160 kN), and 1 million cycles at 42 kips (186 kN). During the entire testing program, the cyclic loads were stopped after every 200,000 cycles and a static load test was performed with a loading amplitude similar to that used during the prior cyclic loads. The static tests included three alternative loading configurations consistent with the maximum and minimum loading patterns used for the cyclic loads.

During the entire experimental testing program, the main structural response measures were recorded, further to performing direct visual inspections. Three categories of instrumentation were installed to collect the necessary data during the tests. This included vibrating-wire strain gauges (VWSG), electrical resistance strain gauges (ERSG), and displacement transducers (DCDT). A total of 36 VWSGs were attached on the top and bottom surfaces of the box beams to measure the longitudinal and transverse strains. They were located at the midspan, two quarter-spans, and two ends of the beams. The six ERSGs were placed on the top and bottom steel bars inside the joint to obtain the strain data at the midspan and two quarter-spans. A total of four DCDTs were placed vertically at the midspan underneath the beams to measure the maximum deflection under cyclic and monotonic loads.

5.4 Experimental Results and Findings

The first boundary condition considered for the current study was a simply supported setup, representing the support condition of the box-beam bridges in service. Noting that a satisfactory load transfer between the adjacent box beams significantly depends on the performance of the longitudinal joint, the deflection of both beams was closely monitored throughout the tests performed in this study. Figure 5.7 shows the load-deflection data at the midspan of the two box beams subjected to 3.4 million cycles of vertical load. This figure shows that the vertical deflection remains consistent between the two box beams even under the highest loading demand. Despite the release of the hand-tightened posttensioning ties after 3 million cycles of load, no significant difference is observed in the deflection recorded in the two beams. This highlights that the need to transverse posttensioning can be minimized with a proper joint design. With a maximum deflection of 0.053 in, 0.122 in, and 0.149 in (1.35 mm, 3.10 mm, and 3.78 mm) in Beam L and 0.054 in, 0.126 in, and 0.147 in (1.35 mm, 3.10 mm,

and 3.78 mm) in Beam R under the loading magnitudes of 18 kip (80 kN), 36 kip (160 kN), and 42 kips (186 kN), respectively, it was inferred that an effective load transfer mechanism was achieved through the developed longitudinal joint. This was further supported by calculating the differential deflection between the two beams. While the differential deflection increased by increasing the amplitude of the applied load, the maximum differential deflection, which was recorded at the highest loading demand, was 0.018 in (0.46 mm). This is still below 0.020 in (0.51 mm) recommended as the maximum acceptable differential deflection between adjacent box beams, according to the PCI Bridge Design Manual (2015).

Another critical parameter to evaluate the performance of the longitudinal joint is the load distribution factor. This factor was calculated in the current study based on the deflection data recorded in the two box beams. The calculations captured two extreme loading conditions of (i) Beam L under the maximum load and Beam R under the minimum load (Figure 5.8(a)) and (ii) Beam L under the minimum load and Beam R under the maximum load (Figure 5.8(b)). As reflected in the plots, the transverse load distribution factors for both box beams remained between 0.45 and 0.55. With an average close to 0.50, it can be inferred that half of the loading demand was consistently transferred to the adjacent beam, indicating a satisfactory load transfer mechanism. While no surface cracks were observed during the cyclic loads, the possibility of initiation of longitudinal cracks between the box beams and the longitudinal joint was further examined using the recorded strains. The strain in the transverse direction was measured at the midspan on the top surface, where the highest strain was anticipated. With the layout of the VWSGs shown in Figure 5.9, the change of strain as a function of the loading cycle was determined at various locations. Despite the increase of transverse strain consistent with increasing the loading amplitude, the maximum strain remained under 25 microstrains.

With the transverse strains significantly below the concrete cracking strain, the box beams and longitudinal joint were found to maintain their structural integrity and performance throughout the tests.

Similar to the simply supported boundary condition, the load cycles applied to the beam setup with the constrained boundary condition did not result in any cracks in either the box beams or the longitudinal joint. The maximum deflection measured at Beams L and R were 0.036 and 0.069, respectively. While the absolute vertical deflections were found to reduce to half of those recorded for the simply supported boundary condition, due to the inclusion of extra supports under one of the two box beams, the differential deflection continued to increase with increasing the amplitude and number of loading cycles (Figure 5.10). This confirmed the capability of the second boundary condition to apply the highest loading demand to the longitudinal joint. Despite this high demand, which was significantly beyond the demand that the box beams are expected to experience in bridge applications, the transverse strains measured at the midspan on the top surface remained significantly below the concrete cracking strain (Figure 5.11). This indicated that the tested joint could deliver satisfactory performance without any structural degradation or cracking issues under various load configurations and amplitudes.

5.5 Modeling Assumptions and Details

A set of FE models that represent the geometry and details of the full-scale test setup were developed using the ABAQUS software package (Abaqus 2014) (Figure 5.12). This was primarily to extend the scope of investigations and evaluate a series of influential parameters related to the reinforcement details in the joint and the interfacial bond properties. The concrete material used for the two box beams and the joint was modeled using C3D8R solid elements.

The steel bars in the box beams were modeled using T3D2 truss elements, while the steel bars embedded in the joint were modeled using C3D8R solid elements. This was to fully capture the contribution of the joint reinforcement, including accounting for possible dowel actions. To evaluate the possibility of damage formation and propagation in concrete, the concrete damage plasticity (CDP) model was employed for the box beams and the longitudinal joint. This material model assumes isotropic damage elasticity in combination with isotropic tensile and compressive plasticity to reflect the inelastic behavior of concrete (Abaqus 2014). Considering that a cyclic loading protocol was used in the experiments, the damage parameters were included in the CDP model to simulate the elastic stiffness degradation due to possible damage to concrete during cyclic load reversals. To model the interfacial contact, the surface-based traction-separation algorithm was used between the box beams and the longitudinal joint. In the current study, the initiation and evolution of damage at the joint interface take place when the following quadratic stress-based damage criterion index is reached:

$$\left(\frac{|t_n|}{t_n^0}\right)^2 + \left(\frac{|t_s|}{t_s^0}\right)^2 + \left(\frac{|t_t|}{t_t^0}\right)^2 = 1 \qquad (1)$$

where t_n^0, t_s^0, and t_t^0 are the normal and the two shear failure stresses, respectively.

To obtain original information about the bond strength between the conventional concrete used in the box beams and the shrinkage-compensating cement concrete used in the longitudinal joint, a set of time-dependent splitting tensile strength tests were performed as part of the current study, following ASTM C496 (2017). The tests included two different surface treatments: (i) the surface was roughened, and (ii) the surface was not roughened, but reinforced with a #4 (No. 13) rebar. The test results indicated that a splitting tensile strength of 580 psi (4.0 MPa) could be achieved after seven days for surface treatment (ii). In a separate

study performed for the Wisconsin Department of Transportation (Bischoff and Toepel 2004), the shear bond strength between the conventional and shrinkage-compensating cement concrete was found to be in the range of 1000 psi (7.0 MPa). Therefore, following the bond test results, t_n^0, t_s^0, and t_t^0 were assumed 580 psi (4.0 MPa), 1,000 psi (7.0 MPa), and 1,000 psi (7.0 MPa), respectively. In addition to the surface-based traction-separation contact, a normal general contact (also referred to as hard contact) was defined for the interface of the box beams and the longitudinal joint.

The convergence characteristics and the computational time of the developed FE models were examined by considering different mesh sizes, from which a mesh size of 2 in. (5 cm) and 1 in. (2.5 cm) were decided for the concrete material and steel reinforcement, respectively. For the validation of the FE models, different loading protocols were considered, similar to the full-scale experimental tests. The first loading protocol consisted of 18 kips (80 kN) and 5 kips (22 kN) vertical forces on Beam L and R, respectively. The loading locations were then switched in the second loading protocol. Another set of simulations were then performed by increasing the amplitude of the applied load to 36 kips (160 kN) and 42 kips (186 kN). Figure 5.13 shows the maximum deflections at the midspan of the test setup under various load configurations. A holistic comparison of the FE simulation results with those obtained from the conducted tests confirms the ability of the developed models to provide reliable predictions consistent with the experiments.

5.6 Simulation Results and Discussions

The minimum shear resistance at the interface between concrete materials can be estimated given in Section 5.8.4 of AASHTO LRFD Bridge Design Specifications (AASHTO 2014):

$$V_i = cA_{cv} + \mu(P_n + f_y A_v) \quad (2)$$

where the V_i is the nominal interfacial bond strength; c and μ represent the factors of cohesion and friction coefficient depending on the surface roughness; f_t is the tensile strength of concrete; P_n is the permanent net compressive force normal to the shear plane; f_y is the yield strength of the reinforcement; A_v is the area of reinforcement crossing the interface.

Prior to performing the FE simulations, the bond strength of the joint tested in the current study was calculated to be 300 psi (2.1 MPa), following Equation 2. Based on the study conducted by Bakht et al. (1983), the maximum shear stress in an adjacent box beam setup can reach up to 160 psi (1.1 MPa), while a minimum bond strength of 150 psi (1.0 MPa) was recommended to avoid interface cracking between the longitudinal joint and adjacent box beams. This indicates that the developed longitudinal joint provides adequate bond strength to ensure the proper transfer of loads. To further support this critical aspect, a comprehensive FE investigation was performed on the design parameters that directly influence the structural response of adjacent box beam setups. For this purpose, three different interfacial bond scenarios, i.e., fully-bonded, partially-bonded, and unbonded, were considered. This was to capture a full spectrum of joint conditions (from intact to completely damaged).

The introduced interfacial bond scenarios were included in the FE models by adjusting the contact properties, such that the fully-bonded joint maintained the original shear and normal bond strength; partially-bonded joint had half of the original shear and normal bond strength; and the unbonded joint lost the entire shear and normal bond strength, performing with friction only. Each of the FE models was then subjected to an increasing displacement-

controlled vertical load, following the setup used in the laboratory experiments. Various structural response measures were extracted, particularly to examine the bond strength at the interface of the longitudinal joint and the transfer of loads between the two adjacent box beams. The average strain in the joint transverse reinforcement bars located between the load point and the midspan under the three contact properties is shown in Figure 5.14. The strain data indicates how the loss of bond can increase the demand that the transverse reinforcement embedded in the joint experiences. To evaluate the overall performance of the developed joint under the three interfacial bond scenarios, the differential deflection between the two adjacent box beams was extracted from the FE simulations. As shown in Figure 5.14(b), all the three setups provide a similar and satisfactory response with a maximum differential deflection no more than 0.4 in (10.2 mm) under a maximum load approaching 250 kip (1,110 kN).

From the existing literature (Li et al. 2010 a,b; Sargand et al. 2017), it is known that the use of transverse reinforcement can significantly enhance the overall integrity and performance of joints. The importance of including such reinforcement is further pronounced in box-beam bridges, as it can help eliminate the need to transverse posttensioning ties. In the absence of similar studies on the joint reinforcement details for box-beam bridges, the current study explores three reinforcement details, including RS-B (8 in. (20 cm) spacing in the two end quarter spans and 10 in. (25 cm) spacing elsewhere), RS-1 (12 in. (30 cm) spacing in the two end quarter spans and 14 in. (35 cm) spacing elsewhere), and RS-2 (16 in. (40 cm) spacing in the two end quarter spans and 20 in. (50 cm) spacing elsewhere), as depicted in Figure 5.15. Considering that the unbonded interfacial bond scenario yields the highest demand on the joint reinforcement, the demand on transverse reinforcement is shown for this scenario in Figure 5.16. This figure provides the strain data recorded in the transverse bar located at the midspan

of the box beam setup. It is noted that the strain increases linearly up to a load magnitude in the range of 100-125 kip (445-555 kN), beyond which the strain begins to increase nonlinearly as the load magnitude further increases. In the linear range, since the joint maintains its integrity, the three details provide very similar contributions. However, in the nonlinear range, in which the joint begins to experience cracks, the demand on transverse bars varies, depending on the joint detail. Assuming that the steel bars of the same size are used, if the spacing is increased, each individual bar experiences an increased demand, which can even reach the yield point, as reflected in the strain profile obtained for the RS-2 reinforcement detail. This further highlights the importance of joint reinforcement details to act as a backup load resisting system (in case of bond damage), further to fulfilling other conventional roles.

5.7 Conclusions

In this study, a new longitudinal joint design for adjacent box-beam bridges was developed, including several material and structural aspects, such as the use of shrinkage-compensating cement concrete, embedment of a distributed reinforcement system, and elimination of transverse posttensioning ties. To evaluate the structural response of this joint setup, two full-scale box beams were cast and connected with a longitudinal joint made with shrinkage-compensating cement concrete. The joint also included hooked reinforcing bars extended from each side of the box beams into the joint and additionally tied with stirrups to form a closed loop. The performance of the full setup was investigated by applying five million cycles of vertical load using a range of loading protocols and boundary conditions. Various response measures, such as strain and deflection, were collected from the experimental tests. A set of complementary FE simulations were then performed with the objective of

understanding the effect of different interfacial bond strengths and joint reinforcement details, beyond those tested in the laboratory. The main observations and conclusions are as follows:

1. Upon the completion of all the monotonic and cyclic loads, the test setup maintained its integrity and performance with no degradation. There was no sign of crack at either the box beams or the longitudinal joint. This was further supported by the strain and deflection data recorded throughout the experiment.
2. Based on the calculations performed to evaluate the effectivity of the longitudinal joint in transferring loads from one box beam to the other, the transverse load distribution factors were found to fall in the range of 0.45 to 0.55. Considering that the calculations reflected the extreme loading scenario of having one beam under the maximum load and the other under the minimum load, it was concluded that the developed joint provides a satisfactory load transfer mechanism.
3. Although the hand-tightened posttensioning ties were released after 3 million cycles of load, the differential deflection between the two adjacent beams did not exceed 0.018 in (0.46 mm) even under the highest loading demand. This was confirmed to remain under the maximum acceptable differential deflection between adjacent box beams, according to the PCI Bridge Design Manual (PCI 2015). With maintaining the deflection of the individual box beams under 0.150 in (3.81 mm), it was found that the need to include transverse posttensioning can be minimized with a proper joint design. This can greatly contribute to facilitating the construction of box-beam bridges.
4. Upon the calibration of the FE models with the test data, FE simulations were performed by exploring three interfacial bond scenarios and three reinforcement details. Capturing the contribution of both bond strength and embedded steel bars, it

was determined that the transverse bars can help the joint setup maintain its overall performance even after the bond between the box beams and the longitudinal joint is degraded, or even lost. Through a separate set of simulations, the change of loading demand on the transverse reinforcement was quantified. This is expected to provide the basis for an optimal design and detailing of joint reinforcement for box-beam bridges.

5.8 Acknowledgement

The authors would like to acknowledge the Iowa Department of Transportation (IADOT) for sponsoring this project. The authors would also like to thank for all the associated tasks to Iowa State University Bridge Engineering Center. The contents of the paper reflect the conclusions and opinions of the authors and do not necessarily express the views of the funding agencies.

5.9 References

AASHTO. (2014). "AASHTO LRFD Bridge Design Specifications." 7th Edition. American Association of State Highway and Transportation Officials, Washington D.C.

Abaqus. (2014). Abaqus User's Manual 6.14.

ASTM C496. (2017). "Standard Test Method for Splitting Tensile Strength of Cylindrical Concrete Specimens." ASTM International, West Conshohocken, PA, 9–13.

Attanayake, U. and Aktan, H. (2008). "Issues with Reflective Deck Cracks in Side-by-Side Box Beam Bridge." 2008 Concrete Bridge Conference, 1–18.

Attanayake, U. and Aktan, H. (2009). "Side-by-Side Box-beam Bridge Superstructure: Rational Transverse Posttension Design.", Proceedings of Transportation Research Board 88th Annual Meeting, Paper No. 09-3420.

Bakht, B., Jaeger, L. G., and Cheung, M. S. (1983). "Transverse Shear in Multibeam Bridges." Journal of Structural Engineering, 109(4), 936–949.

Barnes, J. and Valentine, L. (2002). "Revolution in Shrinkage Compensation-Type G Expansive Component." Concrete International, August 2002, American Concrete Institute, (August 2002), 1–10.

Bischoff, D. L. and Toepel, A. (2004). “Laboratory Testing of Portland Cement Concrete Patch Material Modified to Reduce or Eliminate Shrinkage.” Final Report, Madison, WI.

CTS Cement Manufacturing Corp. (2019). Komponent Datasheet.

Dong, H., Li, Y., and Ahlborn, T. M. (2007). “Performance of Joint Connections between Decked Prestressed Concrete Bridge Girders.” PCI Journal, 48(4), 92–103.

Giraldo-londoño, O. (2014). “Finite Element Modeling of the Load Transfer Mechanism in Adjacent Prestressed Concrete Box-Beams.” M.Sc. Thesis, Ohio University.

Grace, N. F., Jensen, E. A., and Bebawy, M. R. (2012). “Transverse Post-Tensioning Arrangement for Side-by-Side Box-Beam Bridges.” PCI Journal, 57(2), 48–63.

Graves, R. E. (2007). “Significance of Tests and Properties of Concrete and Concrete-Making Materials, STP 169D.” Annual Book of ASTM Standards, West Conshohocken, PA, 337–345.

Gulyas, R. J. (1995). “Evaluation of Keyway Grout Test Methods for Precast Concrete Bridges.” PCI Journal, 40(1), 44–57.

Hanna, K., and Morcous, G., and Tadros, M. (2011). “Adjacent Box Girders without Internal Diaphragms or Post-Tensioned Joints.” PCI Journal, 56(4), 51–64.

Hlavacs, G., Long, T., Miller, R., and Baseheart, T. (1997). “Nondestructive Determination of Response of Shear Keys to Environmental and Structural Cyclic Loading.” Transportation Research Record, 1574(1), 18–24.

Huckelbridge, A. A., El-Esnawi, H., and Moses, F. (1995). “Shear Key Performance in Multibeam Box Girder Bridges.” Journal of Performance of Constructed Facilities, 9(4), 271–285.

Ribeiro Do Valle, C. L., Abdalla, H. A., Islam, S., and Issa, M. A. (2003). “Performance of Transverse Joint Grout Materials in Full-Depth Precast Concrete Bridge Deck Systems.” PCI Journal, 48(4), 92–103.

Murphy, M. L., Kim, J., and Sang, Z. (2010). “Determining More Effective Approaches for Grouting Shear Keys of Adjacent Box Beams.” Final Report, Pennsylvania DOT, Harrisburg, PA.

[20] Lei, X., Yao, Y., Cao, S., and Guo, Z. G. (2015). “Research in Destruction of Concrete Bridge Expanded Joint Influenced by Temperature Difference.” Applied Mechanics and Materials, 803–806.

Li, L., Ma, Z. J., and Oesterle, R. G. (2010a). “Improved Longitudinal Joint Details in Decked Bulb Tees for Accelerated Bridge Construction: Concept Development.” Journal of Bridge Engineering, 15(5), 327–336.

Li, L., Ma, Z. J., and Oesterle, R. G. (2010b). “Improved Longitudinal Joint Details in Decked Bulb Tees for Accelerated Bridge Construction: Fatigue Evaluation.” Journal of Bridge Engineering, 15(5), 511–522.

Liu, Z. and Phares, B. M. (2019). “Small-Scale Investigation on Wide Longitudinal Joints Filled with Shrinkage-Compensated Concrete for Adjacent Box Beam Bridges.” Journal of Bridge Engineering, 24(12), 1–11.

Miller, R. A. (1999). “Full Scale Testing of Shear Keys for Adjacent Box Girder.” PCI Journal, 4(6), 80–90.

Ogawa, K. (1982). “C4A3S Hydration, Ettringite Formation, and Its Expansion Mechanism: II. Microstructural Observation of Expansion.” Cement and Concrete Research, 12(1), 101–109.

PCI. (2015). Bridge Design Manual. Precast/Prestressed Concrete Institute, Chicago, IL.

Péra, J. and Ambroise, J. (2004). “New Applications of Calcium Sulfoaluminate Cement.” Cement and Concrete Research, 34(4), 671–676.

Hussein, H. H., Walsh, K. K., Sargand, S. M., Al Rikabi, F. T., and Steinberg, E. P. (2017). “Modeling the Shear Connection in Adjacent Box-Beam Bridges with Ultrahigh-Performance Concrete Joints. I: Model Calibration and Validation.” Journal of Bridge Engineering, 22(8), 1–14.

Russell, H. G. (2009). “Adjacent Precast Concrete Box Beam Bridges: Connection Details.” NCHRP Synthesis 393, National Cooperative Highway Research Program, Washington, DC.

Russell, H. G. (2011). “Adjacent Precast Concrete Bridges: State of the Practice.” PCI Journal, 56(1), 75–91.

Sang, Z. (2010). “A Numerical Analysis of the Shear Key Cracking Problem in Adjacent Box Beam Bridges.” Ph.D. Dissertation, Pennsylvania State University, State College, PA.

Sargand, S. M., Walsh, K. K., Hussein, H. H., Al Rikabi, F. T., and Steinberg, E. P. (2017). “Modeling the Shear Connection in Adjacent Box-Beam Bridges with Ultrahigh-Performance Concrete Joints. II : Load Transfer Mechanism.” Journal of Bridge Engineering, 22(8), 1–11.

Semendary, A., Walsh, K. K., and Steinberg, E. P. (2017). “Early-Age Behavior of an Adjacent Prestressed Concrete Box-Beam Bridge Containing UHPC Shear Keys with Transverse Dowels.” Journal of Bridge Engineering, 22(5), 1–14.

Sharpe, G. P. (2007). “Reflective Cracking of Shear Keys in Multi-Beam Bridges Reflective Cracking of Shear Keys in Multi-Beam Bridges.” M.Sc. Thesis, Texas A&M University, College Station, TX.

Shi, W., Shafei, B., Liu, Z., and Phares, B. M. (2019). “Early-Age Performance of Longitudinal Bridge Joints Made with Shrinkage-Compensating Cement Concrete.” Engineering Structures, 197, 109391, 1–11.

Sprinkel, M. (2005). “Latex-Modified Concrete Overlay Containing Type K Cement.” FHWA/VTRC 05-R26 Report, Virginia DOT, Richmond, VA.

Steinberg, E. P., Miller, R., Nims, D., and Sargand, S. (2011). “Structural Evaluation of LIC-310-0396 and FAY-35-17-6. 82 Box Beams with Advanced Strand Deterioration.” Final Report, Ohio Department of Transportation, Athens, Ohio.

Yuan, J. and Graybeal, B. (2014). “Adjacent Box Beam Connections.” PCI National Bridge Conference, Precast/Prestressed Concrete Institute, Chicago, 1–28.

Yuan, J. and Graybeal, B. (2016). “Full-Scale Testing of Shear Key Details for Precast Concrete.” Journal of Bridge Engineering, 21(9), 1–14.

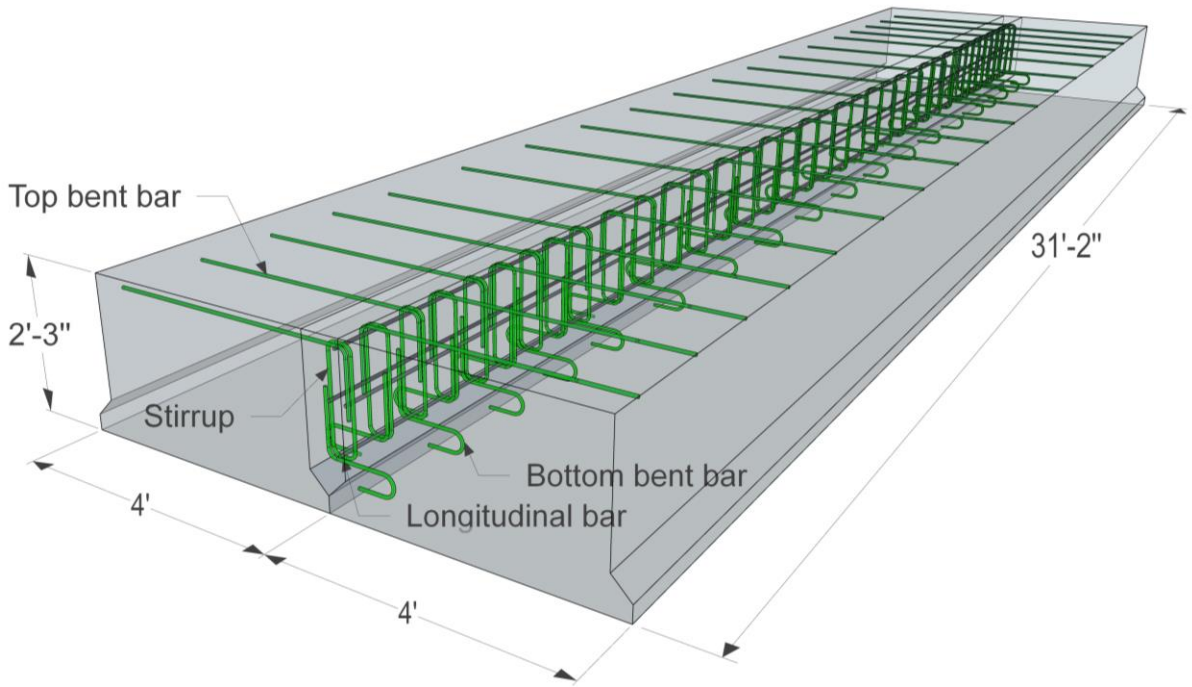

Figure 5.1. 3D view of the proposed reinforcement details for the joint design between adjacent box beams (1 ft = 0.3 m; 1 in = 2.5 cm).

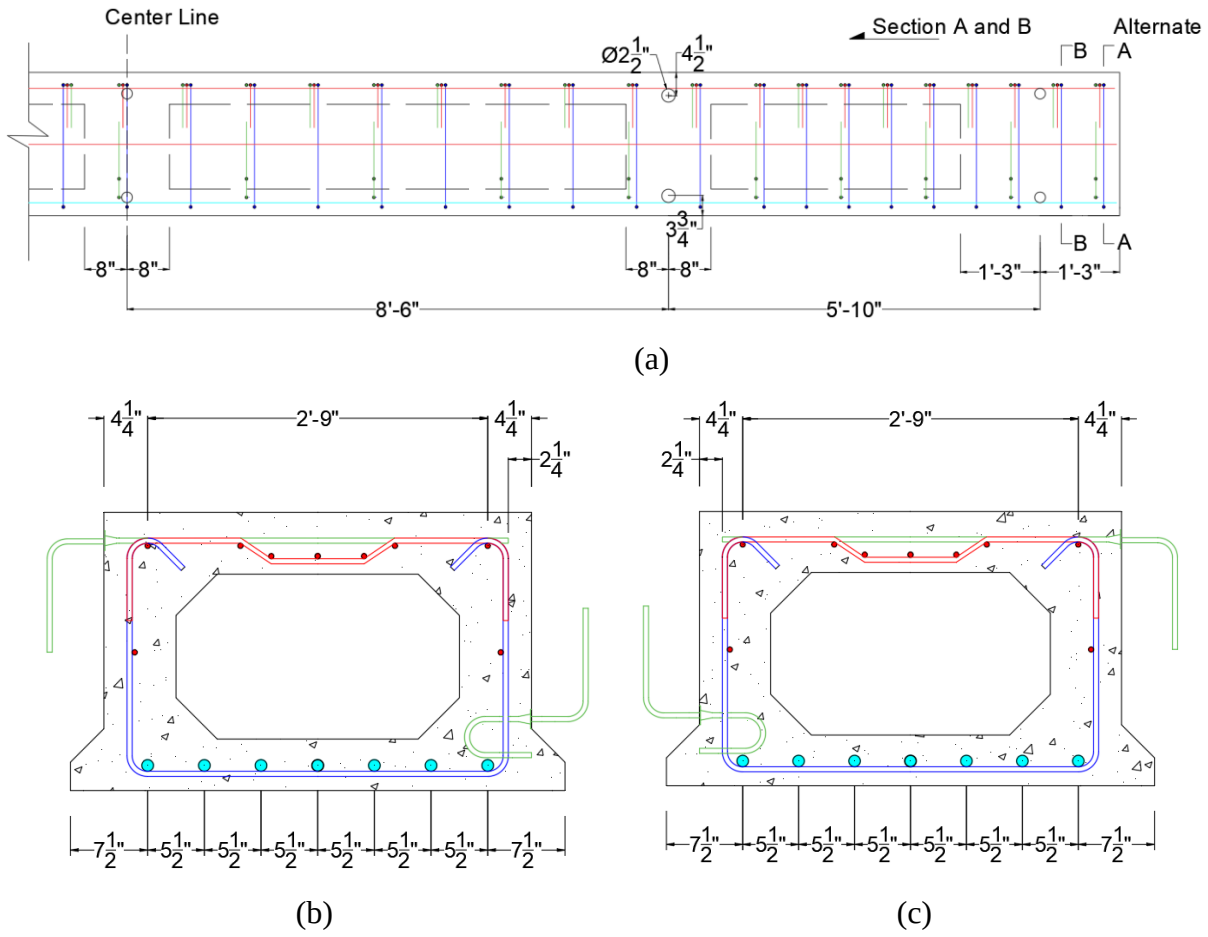

Figure 5.2. Details of joint details (1 in = 2.5 cm; 1 ft = 0.3 m): (a) elevation view; (b) A-A cross section view; and (c) B-B cross section view.

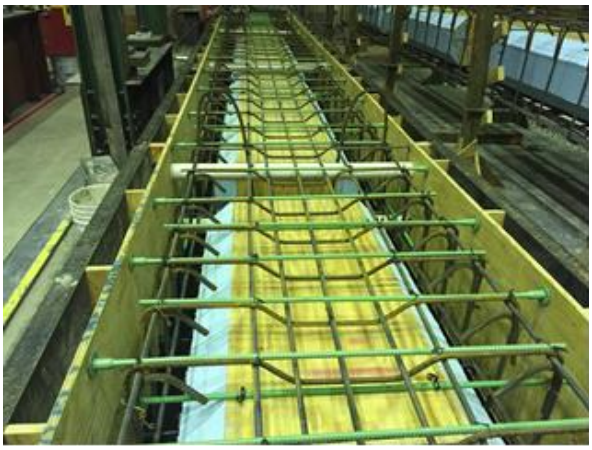

(a)

(b)

(c)

(d)

Figure 5.3. Specimen fabrication: (a) formwork and reinforcement; (b) box beam casting (c) joint reinforcement; and (d) specimen completed.

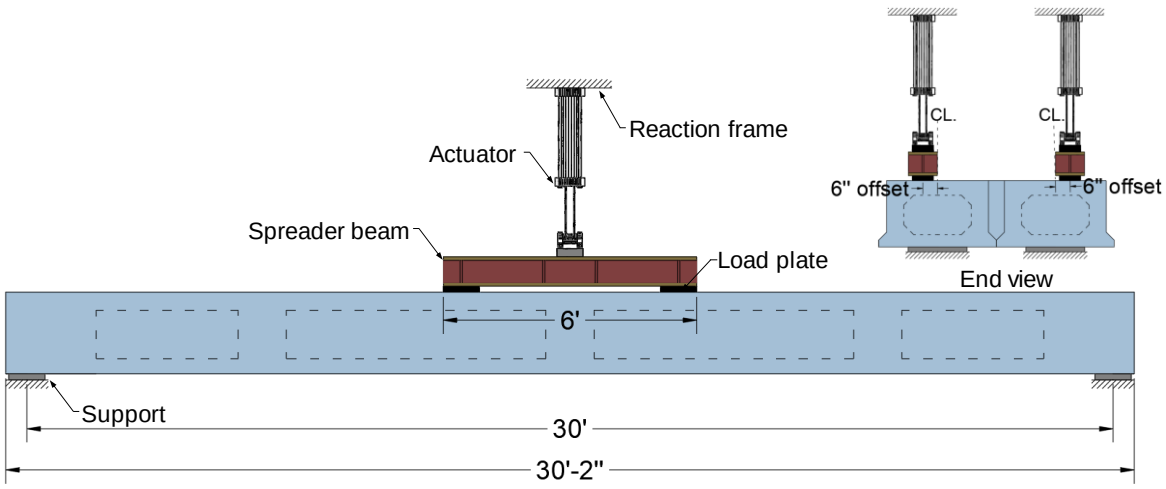

(a)

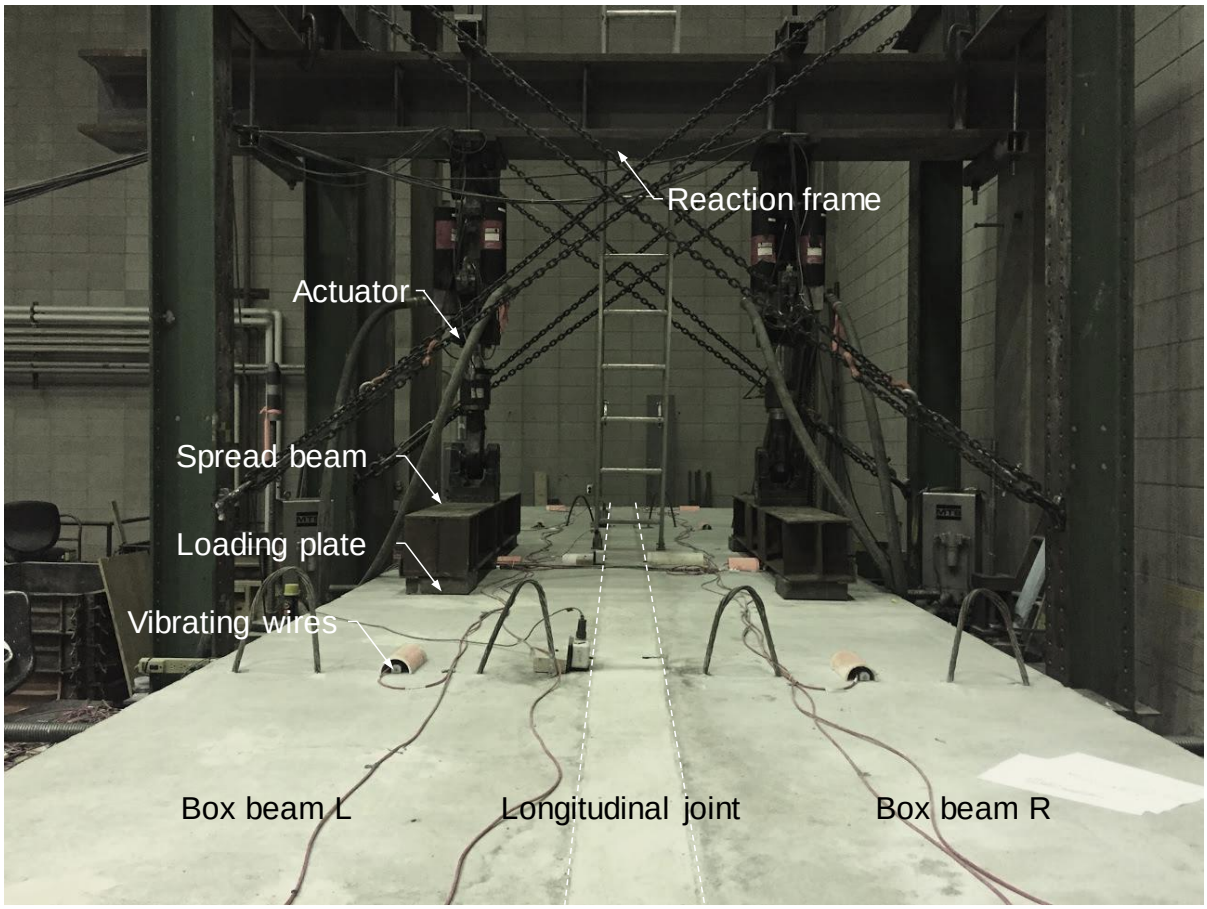

(b)

Figure 5.4. Cyclic structural loading configuration (1 in = 2.5 cm; 1 ft = 0.3 m).

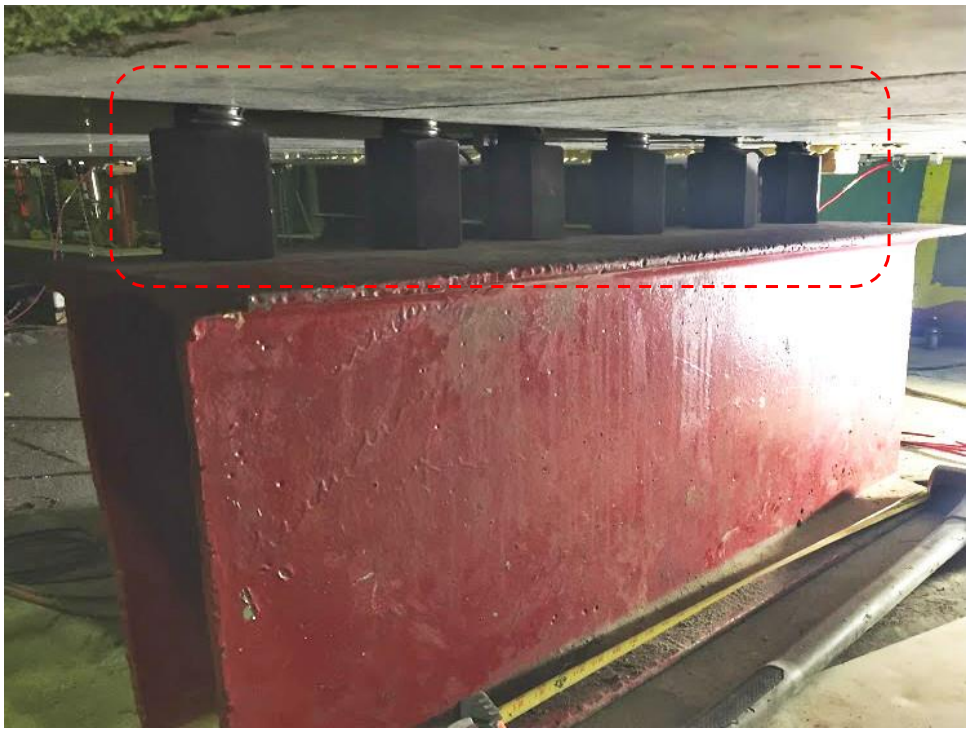

Figure 5.5. Close-up view of restrained boundary condition.

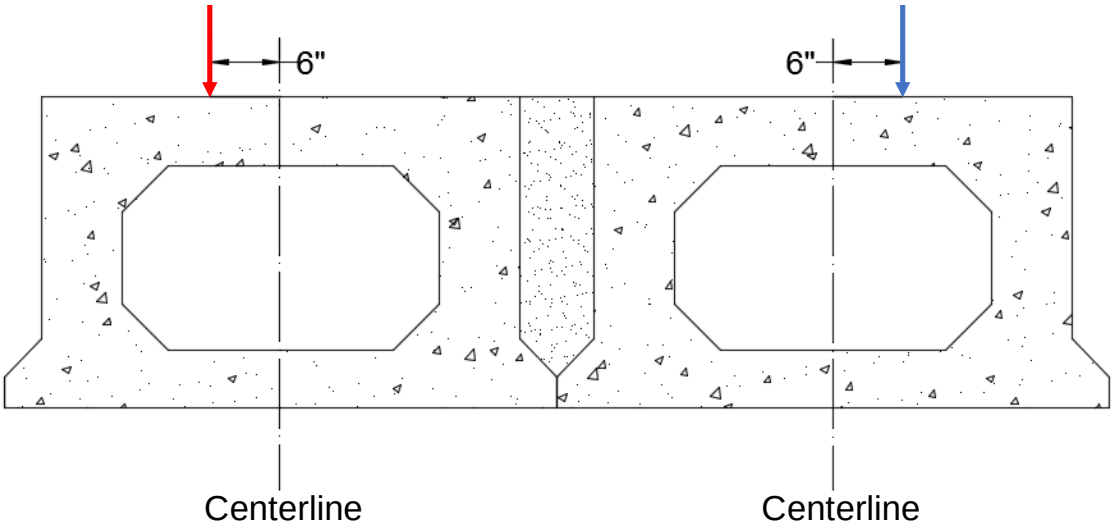
6"
6"
Centerline
Centerline

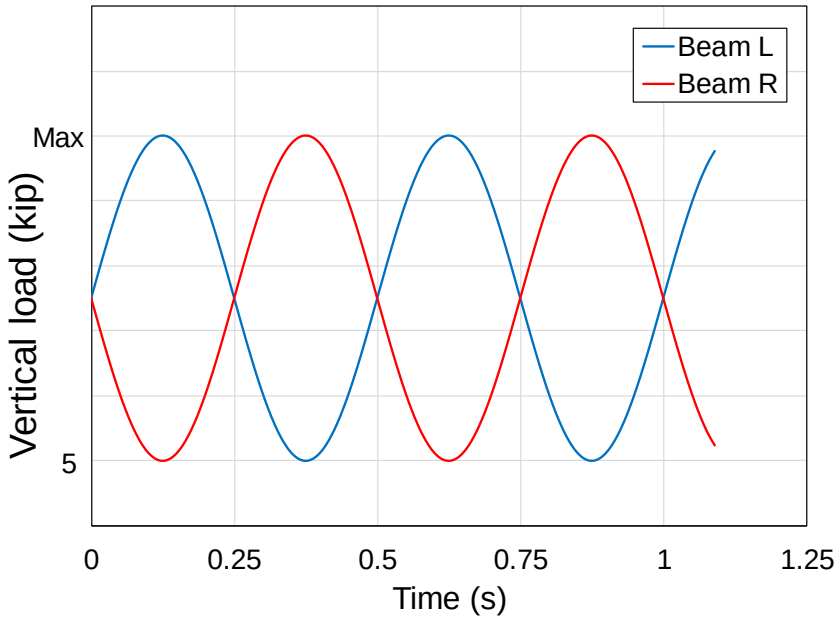
Beam L
Beam R
Max
5
Vertical load (kip)
0
0.25
0.5
0.75
1
1.25
Time (s)

(a)

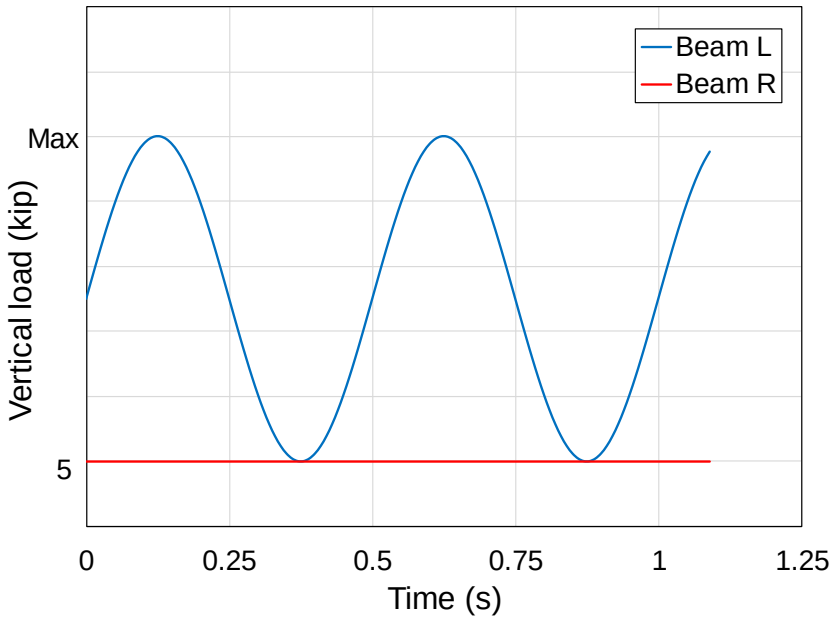

(b)

Figure 5.6. Cyclic loading protocols: (a) simply supported, and (b) one-beam constrained (1 kip = 4.5 kN).

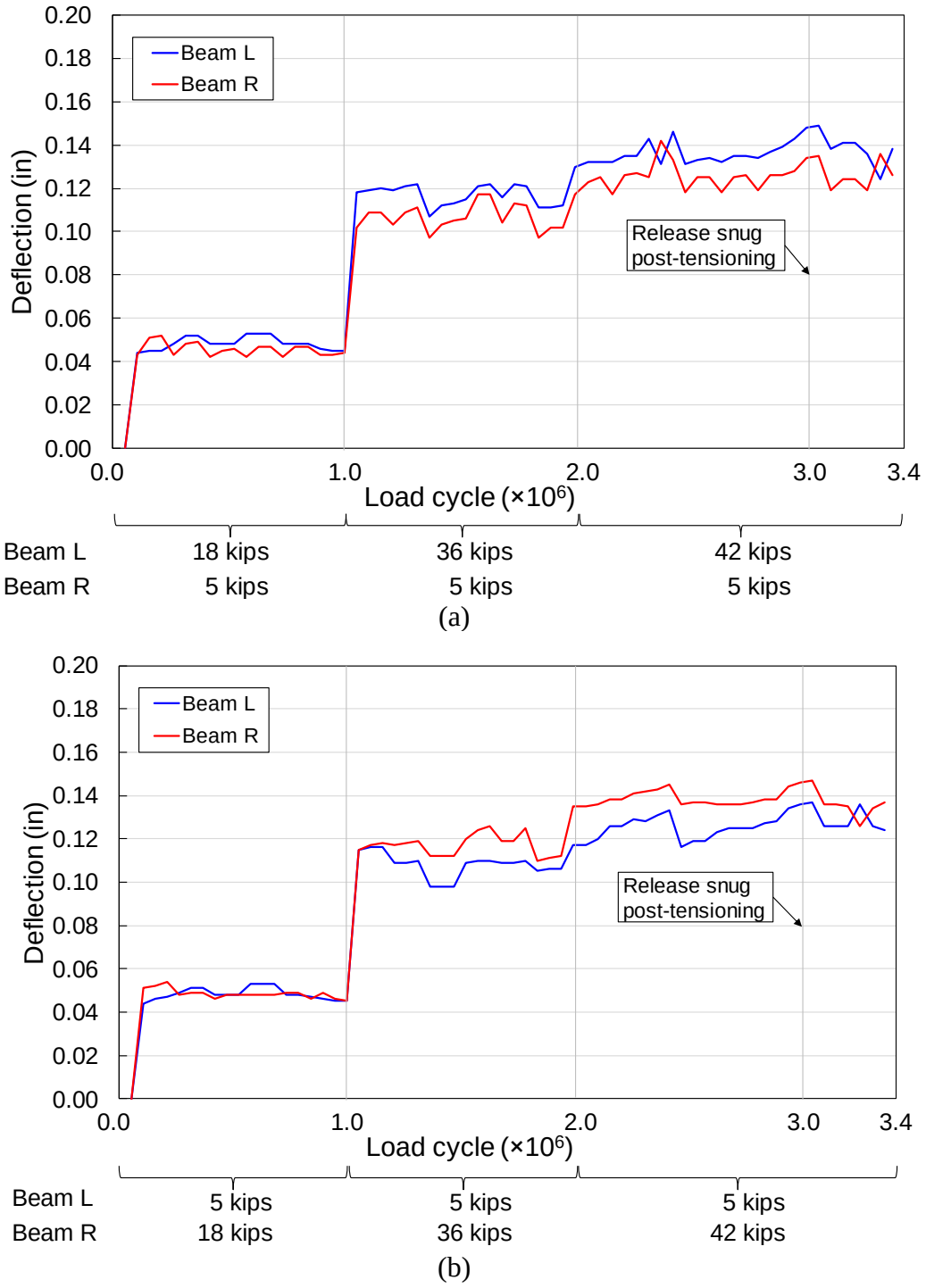

Figure 5.7. Deflection at mid-span of each beam for simply support boundary condition (1 in = 25.4 mm; 1 kip = 4.5 kN).

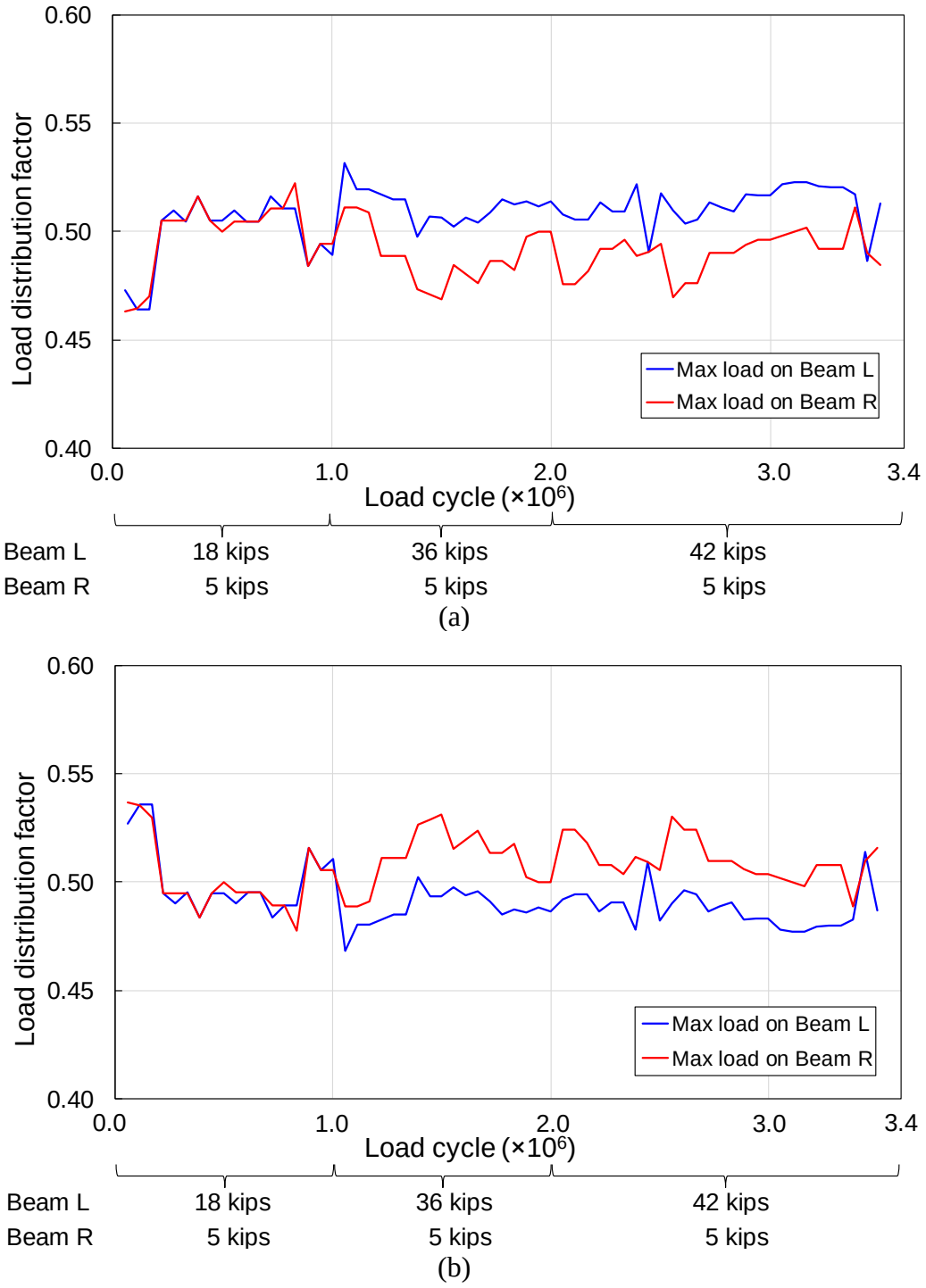

Figure 5.8. Load distribution factor at different loading amplitude for simply supported boundary condition: (a) box beam A; and (b) box beam B (1 in = 2.5 cm; 1 kip = 4.5 kN).

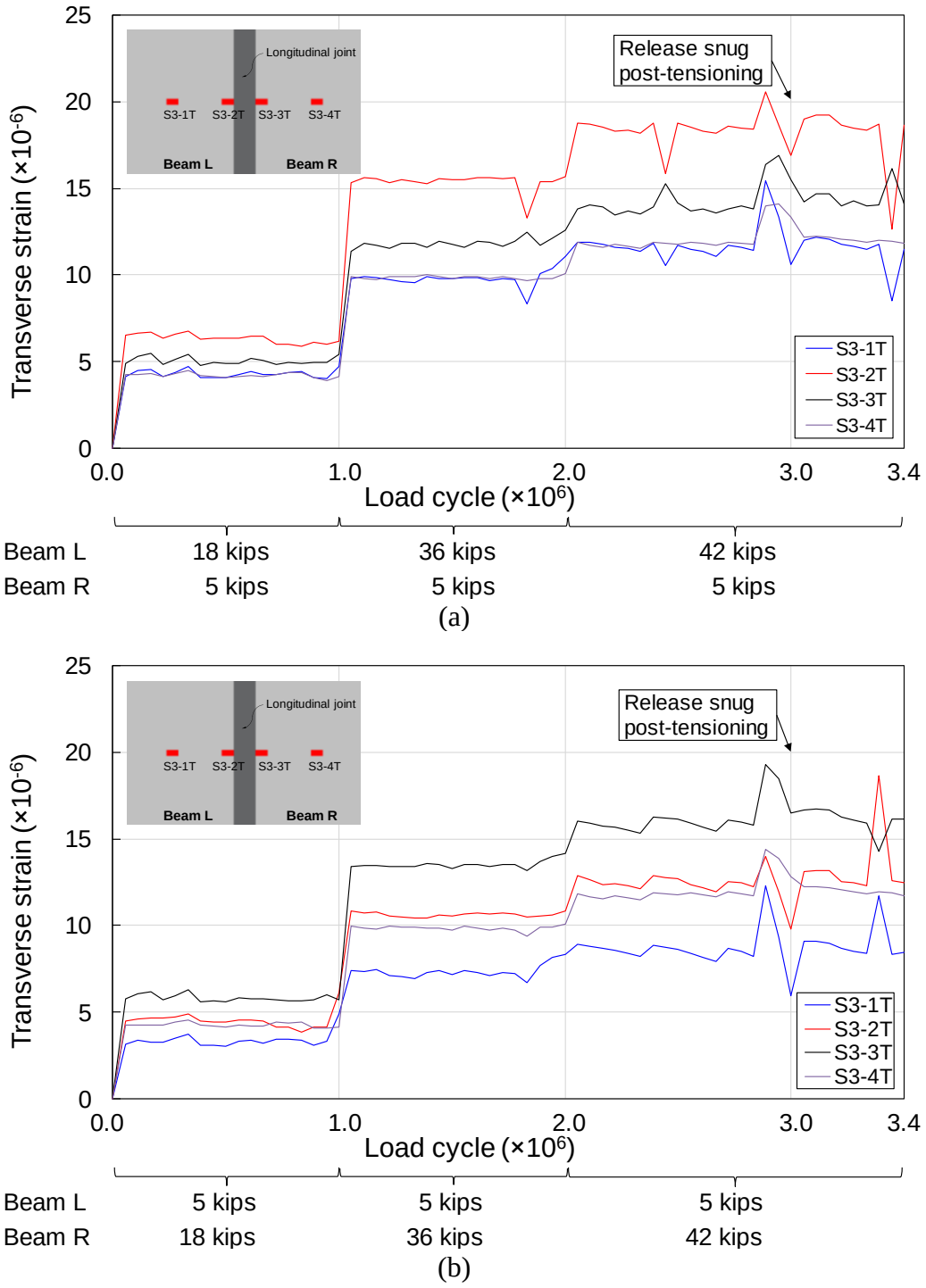

Figure 5.9. Transverse strain of top flange at mid-span of each beam for simply support boundary condition: (a) box beam A; and (b) box beam B (1 kip = 4.5 kN).

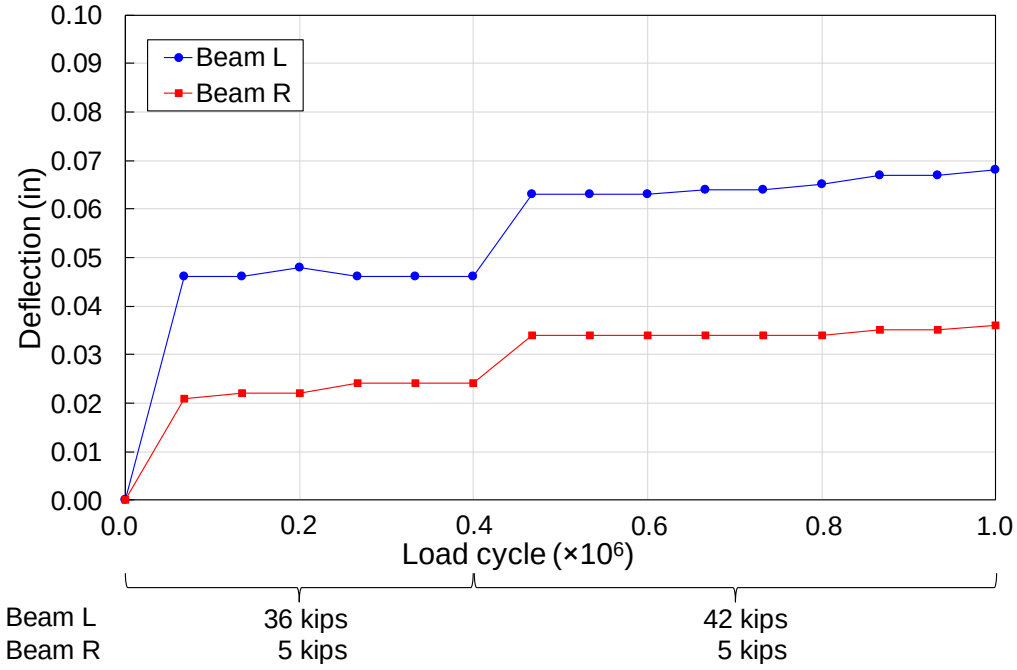

Figure 5.10. Deflection at mid-span of each beam for restrained support boundary condition (1 in = 25.4 mm; 1 kip = 4.5 kN).

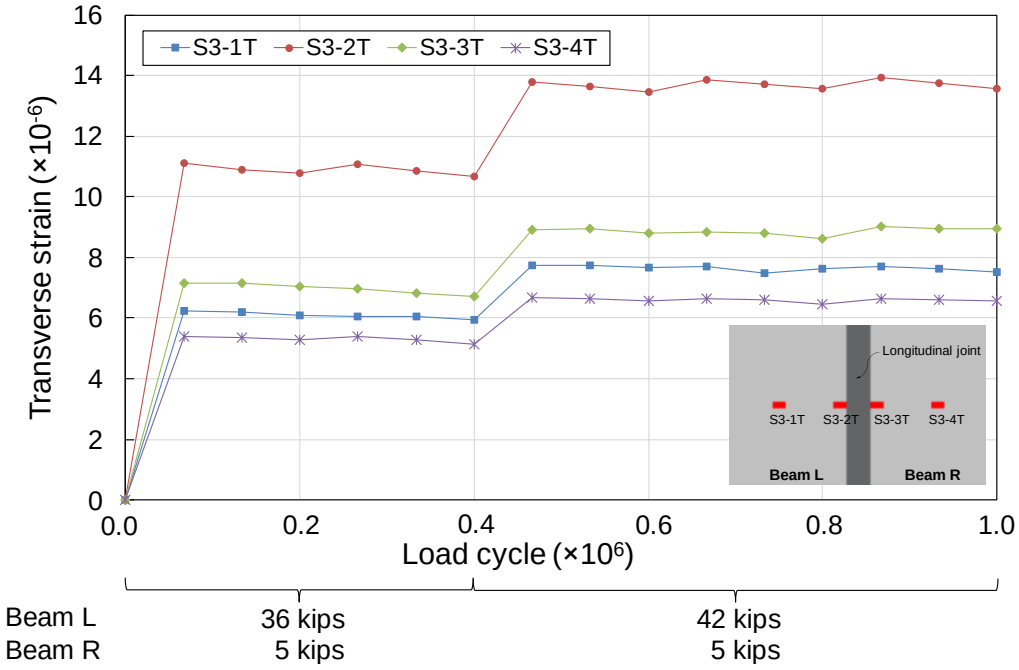

Figure 5.11. Transverse strain of top flange at mid-span of each beam for restrained support boundary condition (1 kip = 4.5 kN).

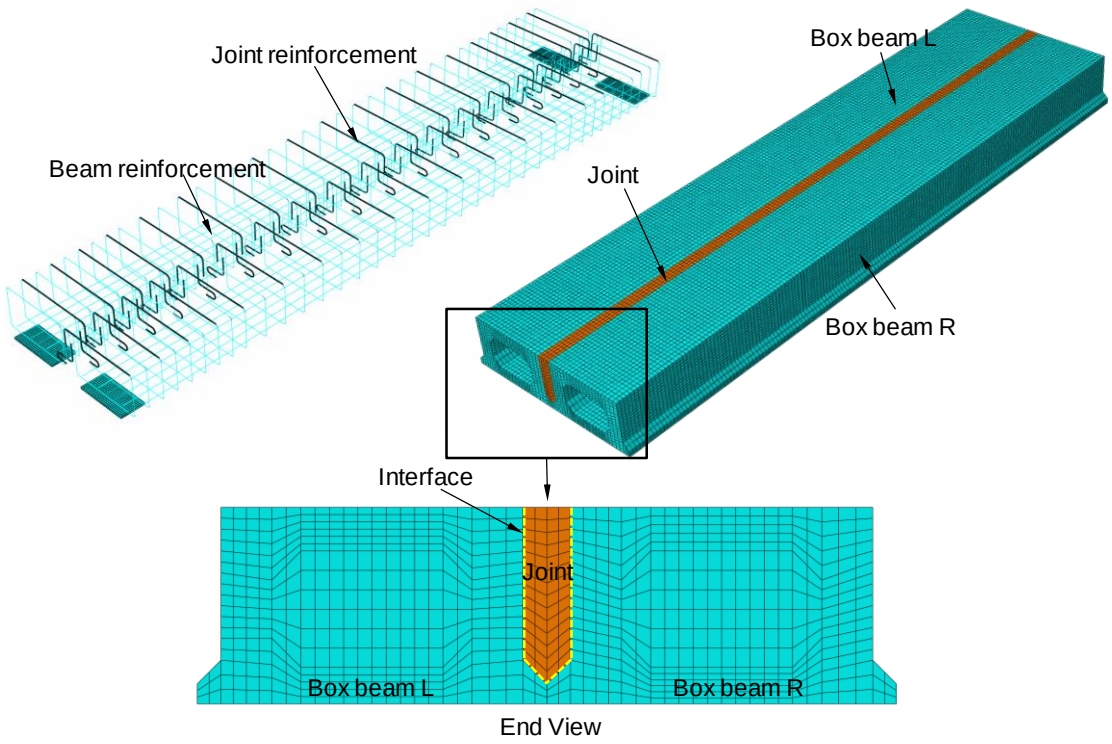

Figure 5.12. FE mesh of the full model of the reinforcement longitudinal joint with two adjacent box beams.

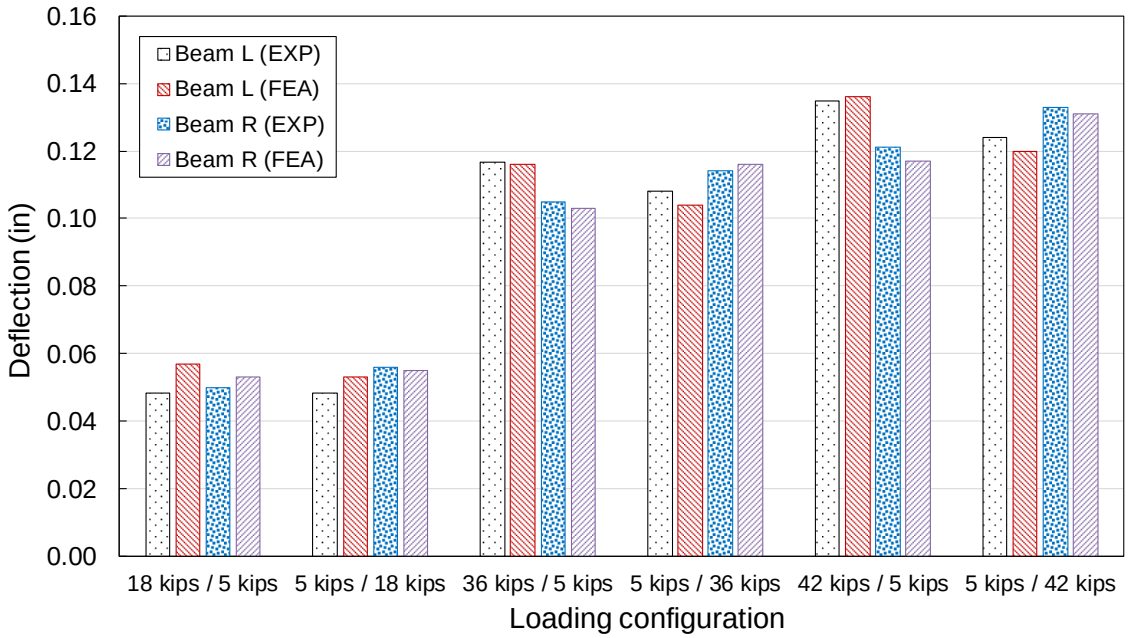

Figure 5.13. Comparison of measured and predicted deflection at mid-span (1 in = 25.4 mm; 1 kip = 4.45 kN).

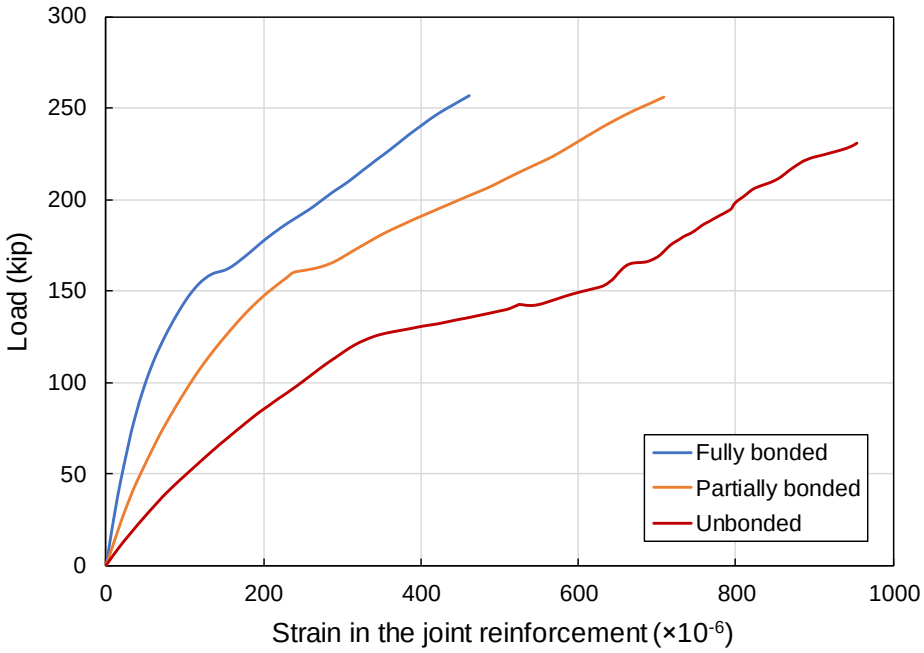

(a)

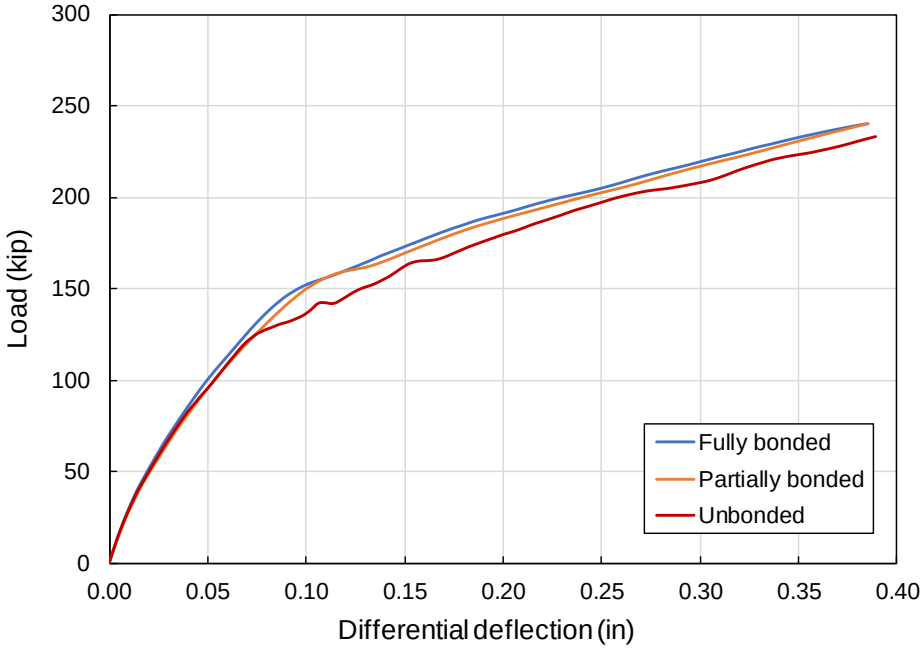

(b)

Figure 5.14. Finite element results under fully bonded, half bonded, and unbonded scenarios: (a) transverse strain of the joint reinforcement; and (b) differential deflection between Beam L and Beam R.

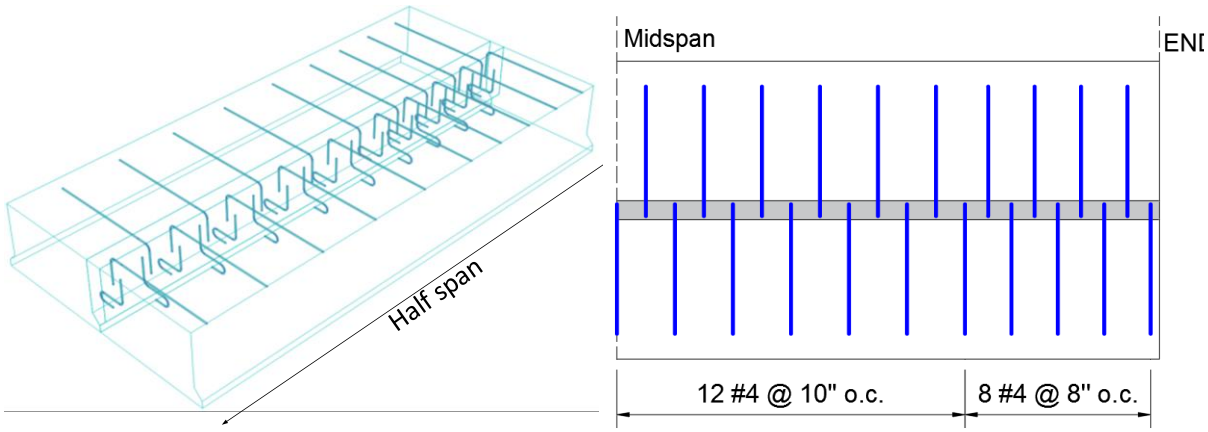

(a)

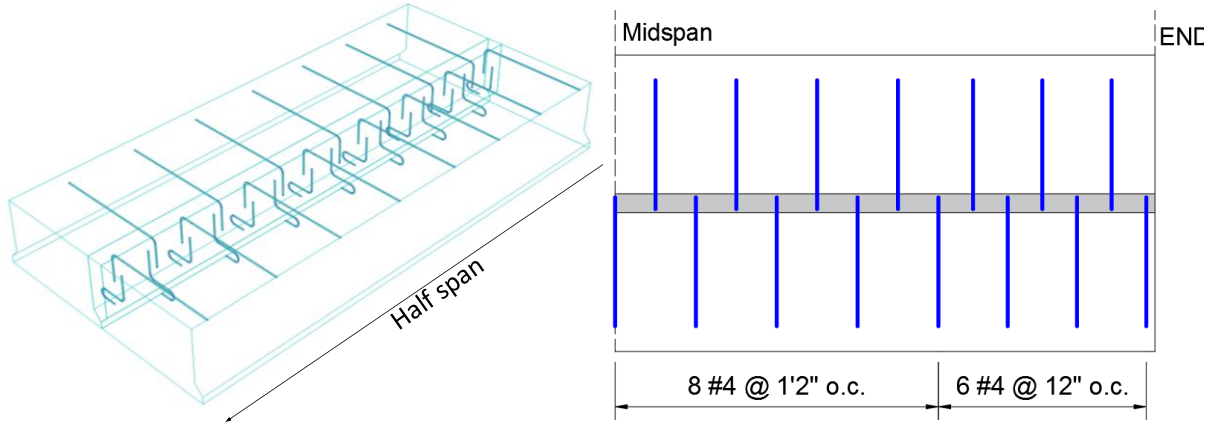

(b)

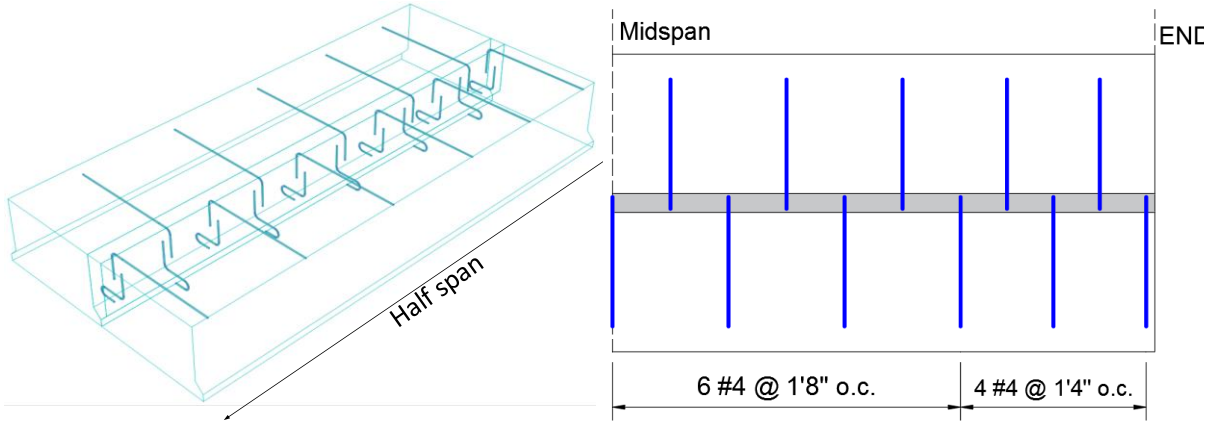

(c)

Figure 5.15. Three joint reinforcement configurations investigated in FE: (a) RS-P, proposed joint reinforcement design; (b) RS-1, 12 in. near the ends and 14 in. at the midspan and (c) RS-2, 16 in. near the ends and 20 in. at the midspan (1 in = 25.4 mm).

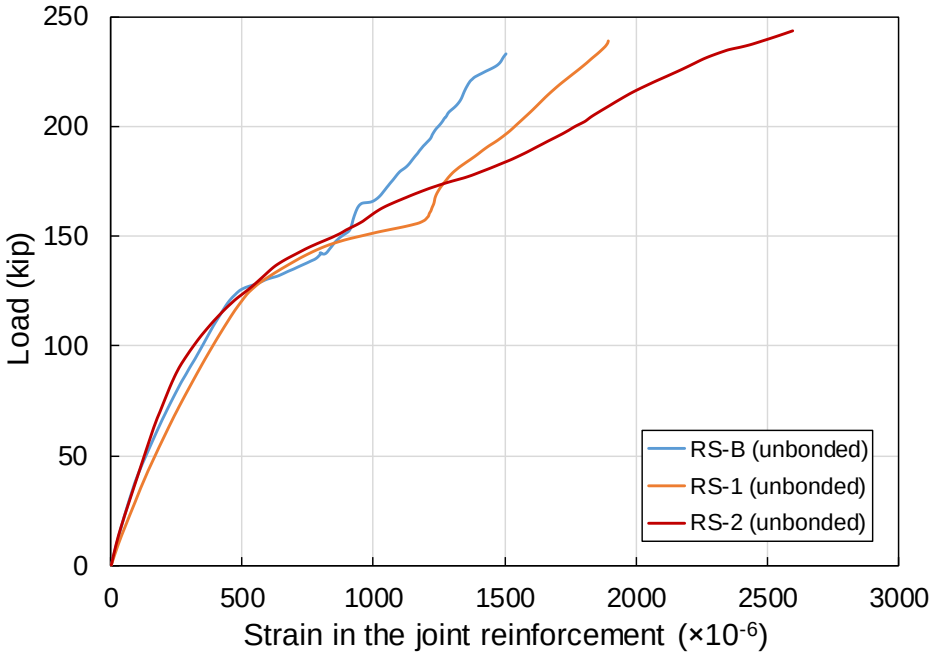

Figure 5.16. Predicted transverse strain of the joint reinforcement versus applied load subjected to full-bonding contact (1 kip = 4.45 kN).

CHAPTER 6. SUMMARY AND CONCLUSIONS

6.1 Summary

To investigate the shrinkage-compensating cement concrete, a holistic experimental program was developed in this research study. This program included small scale SCC-C samples subjected to a series of chloride transport tests and a 31-ft. long specimen made with two box beams and a longitudinal joint. The full-scale structural tests were performed to evaluate early-age thermal effects and cyclic structural loads.

Despite the wealth of information available on the strength, shrinkage, and hydration process of shrinkage-compensating cement concretes, very limited studies were devoted to the investigation of their transport and corrosion properties. With the goal of obtaining an in-depth understanding of penetration of aggressive agents, particularly chloride ions, into shrinkage-compensating cement concretes, a comprehensive laboratory testing program was established to evaluate the concretes made with various dosages of Type K expansive agent (i.e., 0%, 7.5%, 15%, and 22.5% by weight of total cementitious materials) under a number of mechanical, transport, and dimensional stability experiments, including compressive strength, drying shrinkage, rapid chloride penetration, rapid chloride migration, surface electrical resistivity, air permeability, and absorption tests. The listed tests were then complemented with helium and mercury intrusion porosimetry analyses to further support the findings based on the pore structure of hardened mixtures. Corrosion testing of embedded steel reinforcements was also conducted to assess the durability of reinforced concrete structures made with this type of cement.

The study was then extended to investigate how the permeability of concretes made with this type of cement can be improved. For this purpose, similar tests were carried out after

the addition of various supplementary cementitious materials (SCMs), such as fly ash class C, fly ash class F, and silica fume. The outcome of this study led to the identification of optimal dosages of Type K expansive agents, as well as SCMs of choice, that can be utilized for a variety of civil infrastructure applications, especially where there is a high risk of both shrinkage and chloride attack.

In addition, two full-scale box beams were built in the laboratory and connected with concrete made with a 15% replacement of portland cement with Type K shrinkage-compensating cement. In the first test scenario, the primary focus of the investigation was on thermal effects, especially at the early age, due to a combination of diurnal temperature changes and the heat generated during cement hydration reactions. The test scenarios consisted of cycles of heating and cooling for seven days implemented immediately after the joint pour. The data collected from the experimental tests included temperature, longitudinal and transverse strain, and deflection at the joint and individual box beams. To extend the scope of investigations beyond the cases tested in the laboratory, a set of three-dimensional (3D) finite-element (FE) simulations were then performed. The material model used for the longitudinal joint was developed in such a way that the effects of early-age expansion, the heat of hydration, and time-dependent mechanical properties were all taken into consideration. Upon validation of the FE model with the experimental test results, additional simulations were performed to obtain an in-depth understanding of how the joints made with Type K shrinkage-compensating cement concrete respond to extreme thermal loading scenarios, including that provided by AASHTO LRFD Bridge Design Specifications as well as two other additional temperature gradients, i.e., the highest temperature gradient recommended by AASHTO LRFD Bridge Design Specifications (TE-1) and 40 °C (104 °F), i.e., the highest temperature gradient

reported from the field bridge weather monitoring data (TE-2) (White 2017)). The outcome of this study provides an alternative solution to benefit from conventional, low-cost materials to ensure the safety and performance of box-beam bridges.

In the second scenario, the specimen was tested under structural cyclic loading with the aim of investigating structural response. The data collected from the experimental tests consisted of longitudinal and transverse strain, and deflection in the joint and individual box beams due to the cyclic loading effects. A set of three-dimensional finite-element (FE) simulations was also developed with the goal of calibrating the structural performance of the Type K joint by comparing the results obtained from experimental testing, and reasonable agreement between numerical and experimental results was achieved, reflecting the accuracy of the FE modeling used to predict the behavior of such a structural system. Based upon the calibrated FE models, the further study was then extended to evaluate a series of influential parameters related to the arrangement of reinforcement in the joint as well as the interfacial contact properties. The outcome of this study is expected to identify the materials that not only improve the performance and durability of box beam bridge joints, but also facilitate the construction of bridges, especially where only limited resources are available.

6.2 Conclusions

Based on the findings from the experimental results and analysis data, the following conclusions can be made:

- From the laboratory work carried out in this study to evaluate the transport properties and corrosion performance for concrete made with shrinkage-compensating cement:

1. The expansive behavior for the concrete was enhanced with the increase of the dosage of Type K cement (to a certain dosage). It was found that with the contribution of Type K cement, the concrete mixtures experienced a self-volume expansion and achieved the peak value on the 7th day (end of the curing period), while the overall length change was in expansion until 56 days. The results also indicated slight reduction of the observed expansions by the use of SCMs.
2. For the optimal dosage of Type K cement, including 7.5% and 15%, there was an increase in the compressive strength by about 14%, when compared to concrete without Type K cement. Use of high dosage of Type K cement, i.e., 22.5% in this study, resulted in an extensive expansion of paste, which loosened the bond of paste and aggregate, reducing the compressive strength.
3. The resistance of concrete to chloride ion permeability and corrosion resistance reduced by increasing the dosage of replacement of Type K cement. While the addition of class F fly ash led to a partial mitigation of increased chloride permeability caused by the inclusion of Type K cement, the incorporation of silica fume or fly ash C were confirmed as appropriate alternatives for further improvement of the chloride permeability of the concrete mixtures made with Type K cement.
4. A comprehensive review of results collected from the three tests performed to investigate the durability properties and corrosion performance for embedded steel reinforcements of mixtures containing Type K expansive agent confirms the choice of SCMs identified in the current study as a potential solution to

improve the chloride permeability of concretes made with shrinkage-compensating cements. This was supported with the holistic investigation of air permeability, resistance to chloride ions, and corrosion characteristics of embedded steel reinforcements of a wide range of mixtures that were contained 15% Type K expansive agent and 7.5% silica fume or 15.0% fly ash Class C.

5. From the practical point of view, use of Type K cement in concrete can lead to the development of shrinkage free, low permeable concrete if it is combined with proper addition of supplementary cementitious materials. The concrete contained 7.5% silica fume and 15% SCC-C has reached a favorable compressive strength, water absorption, chloride penetration and drying shrinkage.

- From the experimental and numerical investigation of the structural behavior of reinforced longitudinal joints made with this type of cement in bridges for adjacent box beams under thermal loads and millions of cyclic loads:

  1. After seven cycles of thermal loads and five millions of cyclic loads, no cracks were found at the interfaces of the joint and adjacent box beams. According to the strain data collected from the top surface of the box beams, both transverse and longitudinal strain changes were consistent with the temperature profiles with no unexpected trends.
  2. Upon the completion of all the monotonic and cyclic loads, the test setup maintained its integrity and performance with no degradation. There was no sign of crack at either the box beams or the longitudinal joint. This was further supported by the strain and deflection data recorded throughout the experiment.

3. Based on the behavior observed here in this study, while the shrinkage-compensating concrete joint was found to have a promising early-age performance for adjacent box beam bridge, the final judgement concerning applicability of proposed joint design should also combine the analysis of live loads effect, which will be concluded in author's another paper.
4. With respect to the performance of Type-K cement joint under cyclic loading, transverse posttension force shows a limited contribution to crack resistance at the interface. In addition, the difference from the use of transverse posttensioning ties with or without hand force was also not significant. However, the reinforcing bar system utilized in the joint provides transverse connection strength and longitudinal stiffness both during early and later loading. This may greatly facilitate the construction of bridges and reduce construction costs.
5. Based on the numerical models developed in this research study, it was found that during the early age, the maximum principal stress in conventional concrete can be more than 40% higher than that in shrinkage-compensating cement concrete, highlighting an increased vulnerability of the joint to shrinkage-induced cracks if a conventional concrete is used.
6. Upon the calibration of the FE models with the test data, FE simulations were performed by exploring three interfacial bond scenarios and three reinforcement details. Capturing the contribution of both bond strength and embedded steel bars, it was determined that the transverse bars can help the joint setup maintain its overall performance even after the bond between the

box beams and the longitudinal joint is degraded, or even lost. Through a separate set of simulations, the change of loading demand on the transverse reinforcement was quantified. This is expected to provide the basis for an optimal design and detailing of joint reinforcement for box-beam bridges.

6.3 Constructability and Design Recommendations

Based on the experimental findings and analyses of data, the following recommendations have been summarized for designing and constructing longitudinal reinforced shrinkage-compensating cement concrete joint for adjacent box beam bridges:

- Use of chemical formwork retarder was found to be an efficient method to roughen the surface.
- The elimination of the transverse posttensioning ties can significantly improve the construction speed and efficiency. This eventually reduces the traffic delays and road closures, minimizing indirect costs.
- Based on the observation from material investigation, joint cast with SCC-C is required to be well planned and completed within a short time due to its low workability.
- To resistance of chloride induced corrosion for joint made with SCC, the use of some SCMs, i.e., silica fume or fly ash class C, are highly recommended to include in the mix design.
- The promise of the innovative joint design developed as part of this project can be further evaluated through field applications. Extension of laboratory observations to field investigations can be an appropriate next step for properly utilizing the joint

details that can offer a safe, durable, and economic alternative for various bridge applications.